Technical Physics Letters, Vol. 28, No. 5, 2002, pp. 355–356. Translated from Pis'ma v Zhurnal Tekhnicheskoĭ Fiziki, Vol. 28, No. 9, 2002, pp. 1–5.
Original Russian Text Copyright © 2002 by Tikhov, Pavlov, Shilyaev, Shobolov, Os'kin.

Hydrogen Sensitivity of a Silicon Schottky Diode Increased by Modification of the Semiconductor Surface Microrelief

S. V. Tikhov, D. A. Pavlov, P. A. Shilyaev, E. L. Shobolov, and A. A. Os'kin
Nizhni Novgorod State University, Nizhni Novgorod, Russia
e-mail: fdp@phys.unn.ru; shobolov@phys.unn.runnet.ru

Received December 17, 2001

Abstract—A nearly atomically smooth semiconductor surface in a Schottky diode based on the palladium–oxide–silicon structure is modified by treating with a selective etchant. It is shown that the appearance of a developed microrelief (with an average roughness of 22–32 nm and a fractal dimension of 2.33–2.40) leads to a decrease in the barrier height of the Pd–Si junction, an increase in the density of states at the oxide–silicon boundary, and a considerable (an order of magnitude) growth in the sensitivity with respect to hydrogen detected by a change in the diode reverse current. *© 2002 MAIK "Nauka/Interperiodica".*

Schottky diodes with a catalytically active palladium electrode can be used as energy-saving miniature remote hydrogen sensors [1]. Gas-sensitive Schottky diodes are usually manufactured by standard technology using semiconductors possessing an almost atomically smooth surface. Below we will demonstrate that modification of such a surface leading to the formation of a developed surface roughness provides for a significant increase in the sensitivity with respect to hydrogen.

The Schottky diodes were based on (100)-oriented single crystal *n*-Si wafers with a resistivity of 4.5 Ω cm. The experiments were performed with silicon plates possessing either a mirror-flat surface, obtained by treatment in a standard polishing etchant HNO_3–HF–HAc (8 : 1 : 1) until removal of the mechanically damaged surface layer, or a rough surface obtained upon additional 3-min treatment in the selective Sirtle etchant CrO_3–HF (1 : 1). For the preparation of hydrogen-sensitive Schottky diodes, the silicon surface was annealed so as to obtain a thermal oxide layer with a thickness of about 4 nm, after which a ~20-nm-thick palladium electrode was formed by deposition in vacuum.

The surface of oxidized silicon samples coated with palladium was studied by atomic force microscopy (AFM) in a Topometrix Accurex TMX-2100 instrument operated in a contactless mode. The surface topology was quantitatively characterized by calculating an average roughness height and the fractal dimension. According to [2], the fractal dimension more adequately characterizes the surface structure and allows various types of the crystal surface to be distinguished using a single value ranging between 2.0 (the ideal smooth surface) to 3.0 (a strongly developed porous surface). The fractal dimension was determined by a conventional method of counting cells [3].

Figure 1 shows typical AFM images of the silicon surfaces observed upon treatment with (a) polishing and (b) selective etchants. The former sample is characterized by an average roughness height of $\tilde{h} \approx 0.4$ nm and a fractal dimension of $\Phi \approx 2.12$, which is close to an atomically smooth surface, whereas the latter sample has $\tilde{h} \approx 22$ nm and $\Phi \approx 2.33$, which is evidence of

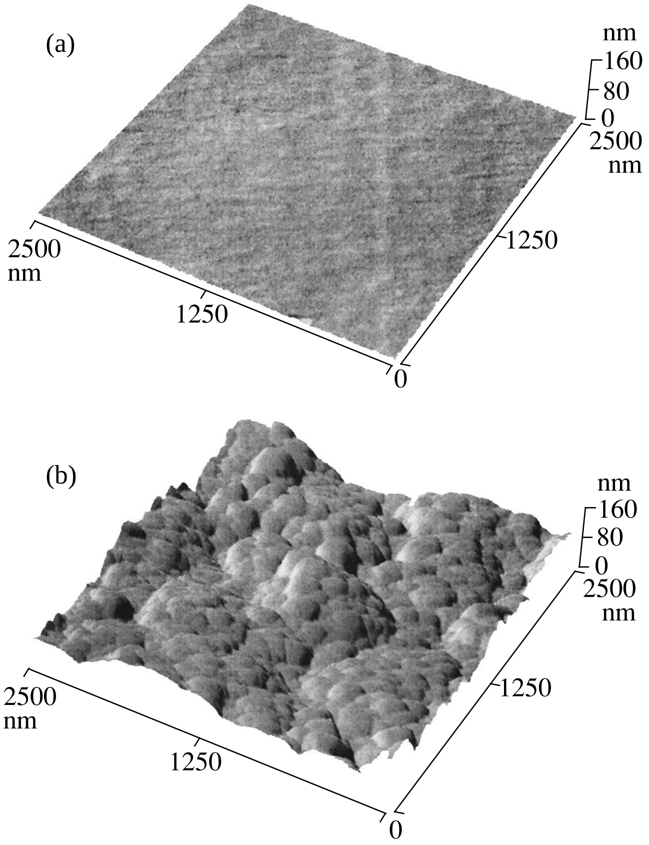

Fig. 1. AFM images of the surface of silicon crystals upon treatment with (a) polishing and (b) selective etchants.

1063-7850/02/2805-0355$22.00 © 2002 MAIK "Nauka/Interperiodica"

Some electric parameters of hydrogen-sensitive Schottky diodes

Sample no.	Surface condition*	φ_B, V	m	ΔV_I, V	ΔV_{ph}, V	ΔJ, A/cm^2	$\Delta J/J$
1	Polished (0.4; 2.12)	0.76	1.02	0.03	0.03	1.8×10^{-3}	6
2	Polished (1.5; 2.20)	0.78	1.02	0.11	0.06	2.7×10^{-3}	7
3	Strongly rough (22; 2.33)	0.70	1.50	0.16	0.18	2.3×10^{-2}	130
4	Strongly rough (32; 2.40)	0.75	1.30	0.16	0.14	3.1×10^{-2}	116

Note: * Values in parentheses indicate the average surface roughness and fractal dimension, respectively.

a significant surface roughness. Note that the surface of a Pd film virtually repeated, with slight smoothing, a microrelief of the underlying silicon surface.

Some electric properties of the Schottky diodes based on polished and strongly rough silicon surfaces, determined from measurements of the current–voltage (I–V) characteristics in the dark and under illumination, are summarized in the table. Here, φ_B is the barrier height of the Pd/Si junction (determined by extrapolating the exponential portion of the I–V characteristic to $V = 0$) and m is the nonideality factor [4]. The other parameters in the table characterize the diode response to hydrogen at a concentration of 0.6 vol % and a temperature of 90°C: ΔV_I is the shift of a direct branch of the I–V curve measured at a current density of $J \approx 10^{-3}$ A/cm^2 [5]; ΔV_{ph} is the change in the open-circuit voltage (photo emf); ΔJ is the change in the reverse current for $V = -0.3$ V on the Pd contact; and $\Delta J/J$ is the change in the current relative to the initial value (before hydrogen admission). As can be seen from the data presented in the table, the Schottky diodes with strongly rough semiconductor surface exhibit a slightly lower (the difference not exceeding 0.08 V) values of φ_B, significantly increased m, and very strongly (by an order of magnitude) increased hydrogen sensitivity (determined by ΔJ).

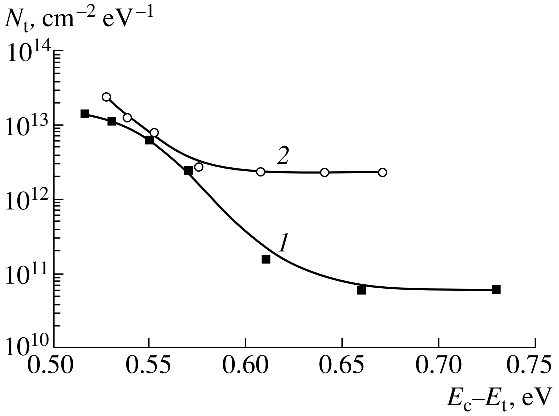

Fig. 2. Plots of the density of surface states N_t localized at the oxide–silicon interface versus energy E_c–E_t determined for the structures with (*1*) polished and (*2*) strongly rough silicon surfaces (E_c is the conduction band edge of silicon; E_t is the surface energy level).

Figure 2 shows plots of the density of surface states N_t localized at the oxide–silicon interface versus energy, determined for the polished and strongly rough samples using the method described in [6]. As can be seen, the N_t value is significantly (by more than one order of magnitude in the upper half of the bandgap of silicon) greater for the rough surface. It might seem that the hydrogen sensitivity of the diode could decrease [6] as a result of increased screening of the surface states; instead, the sensitivity increases, probably due to an increase in activity of the PD–oxide interface with respect to hydrogen adsorption [7]. The latter can be related to the strong roughness and high fractal dimension of the modified semiconductor surface.

In concluding, we note that the relative sensitivity to hydrogen $k = \Delta J/J$ presented in the table is not the maximum possible for Schottky diodes with a rough semiconductor surface. Indeed, assuming that k is determined only by a change in the barrier height caused by the hydrogen adsorption, the value of k (e.g., for $\Delta V_{ph} \approx 0.18$ V, see table) must be ~400 instead of the observed ~130. This result can be explained by the fact that changes in the diode current are limited by the tunneling of charge carriers through the oxide film [8]. A decrease in the oxide thickness must lead to an increase in the tunneling current and, hence, to a further growth in sensitivity of the Schottky diodes with respect to hydrogen.

REFERENCES

1. A. V. Evdokimov, M. N. Mushurudli, A. E. Rzhanov, *et al.*, Zarubezhn. Élektron. Tekh., No. 2 (321), 3 (1988).
2. S. Chesters *et al.*, in *Proceedings of Institute of Environmental Sciences* (1990), Vol. 316.
3. J. Feder, *Fractals* (Plenum, New York, 1988; Mir, Moscow, 1991).
4. E. H. Rhoderick, *Metal–Semiconductor Contacts* (Clarendon, Oxford, 1978; Radio i Svyaz’, Moscow, 1982).
5. V. I. Gaman, P. I. Drobot, M. O. Duchenko, *et al.*, Poverkhnost, No. 11, 64 (1996).
6. V. I. Gaman, M. O. Duchenko, and V. M. Kapygina, Izv. Vyssh. Uchebn. Zaved., Fiz., No. 1, 69 (1998).
7. A. V. Rzhanov and V. I. Filippov, Mikroélektronika **19** (1), 106 (1990).
8. V. Kumar and W. E. Dahike, Solid-State Electron. **20** (2), 113 (1977).

Translated by P. Pozdeev

Technical Physics Letters, Vol. 28, No. 5, 2002, pp. 357–360. Translated from Pis'ma v Zhurnal Tekhnicheskoĭ Fiziki, Vol. 28, No. 9, 2002, pp. 6–13.
Original Russian Text Copyright © 2002 by Naydenov, Ryzhikov.

Determining Chemical Compositions by the Method of Multi-Energy Radiography

S. V. Naydenov and V. D. Ryzhikov
Institute of Single Crystals, National Academy of Sciences of Ukraine, Kharkov, Ukraine
e-mail: naydenov@isc.kharkov.com

Received November 11, 2001

Abstract—A theoretical model of multi-energy radiography is proposed and two approaches—“synthesis” and “analysis”—to studying the structure of objects by this method are considered. It is theoretically proved that the atomic numbers of elements and the other parameters of chemical composition of a sample can be restored from the multichannel absorption data. The multi-energy radiography approach and possible generalizations open wide prospects for both basic experimental investigations and nondestructive testing applications. *© 2002 MAIK “Nauka/Interperiodica”.*

At present, X-rays and γ-radiation are effectively employed for nondestructive testing of materials. This direction achieved additional impact due to the development of digital data processing (computer-aided) techniques [1]. Of special interest among such modern developments is digital radiography—a method intended for distinguishing spatial structures of materials in the same object, possessing identical or different chemical compositions. This provides for the possibility of monitoring the topography of various articles (in particular, electronic devices) [2], detecting flaws in mechanical joints, and analyzing chemical compositions. In medicine, digital radiography techniques allow differential monitoring and diagnostics of soft and bone tissues [3]. Among other applications, of special importance is the ability of detecting dangerous and prohibited substances (explosives, drugs, etc.).

An especially high efficacy was demonstrated by the two- and three-energy radiography techniques [4], employing detectors capable of measuring the interaction of γ-quanta with substances in different energy intervals [1]. This approach provides additional information about the structure of an object studied. In the traditional approach, this information is incompletely employed (in particular, hindering the quantitative analysis of elements with close atomic numbers).

Below we will theoretically prove that the results of multi-energy radiography (MER) can be used for quantitative analysis of the composition of random objects. Previously, such problems were solved by large and expensive neutron facilities [5]. Depending on the MER configuration employed, it is possible to restore various parameters of the atomic and spatial structure.

Let us consider an object of rectangular geometry, oriented with its plane perpendicular to the radiation beam direction. In the case of an object possessing arbitrary shape, one should consider elementary parallelepipeds “cut” by the beam scanning over the sample. The total thickness Δ is assumed to be known (fixed). This value can be determined, for example, by tomography. The main task of the subsequent monitoring is to determine a chemical composition of materials present in the object studied. Each material can represent either a simple or complex substance. The atomic structure is identified in terms of the effective atomic number Z_{eff} [6], density ρ, and relative atomic concentrations a_k of elements ($k = 1, \ldots, P$; $\Sigma_k a_k = 1$). In the general case, it is also necessary to provide for the spatial separation of components, that is, to establish the thickness of layers Δ_j ($j = 1, \ldots, Q$; $\Sigma_j \Delta_j = \Delta$) representing different components (various materials or parts of the object). Below, we restrict the consideration to a monolayer case, although the multi-energy approach allows multilayer objects to be studied as well. The last simplification adopted here is the assumption of a fixed set of energies E_i ($i = 1, \ldots, N$) of the γ-radiation detected. A nonmonochromaticity (energy scatter) in each particular interval influences the efficacy of signal detection, but not the basic possibilities of the MER method. In practice, nonmonochromatic sources are employed in which the particular energy intervals are cut by a system of radiation energy filters.

The physical basis of radiography is the absorption of ionizing radiation in a substance. For γ-quanta, the absorption leads to the phenomena of photoeffect, Compton scattering, and pair production. The corresponding partial cross sections are determined both theoretically [7] and experimentally [8]. The radiation is absorbed both in the object studied and in the radiation detector. The signal measured can be described as

$$V_i = V(E_i) = \eta(E_i) V_0 \exp\left[-\sum_{j=1}^{Q} \mu_{ij} \Delta_j\right]; \tag{1}$$

$$\mu_{ij} \equiv \mu(E_i; Z_{\text{eff},\,j}),$$

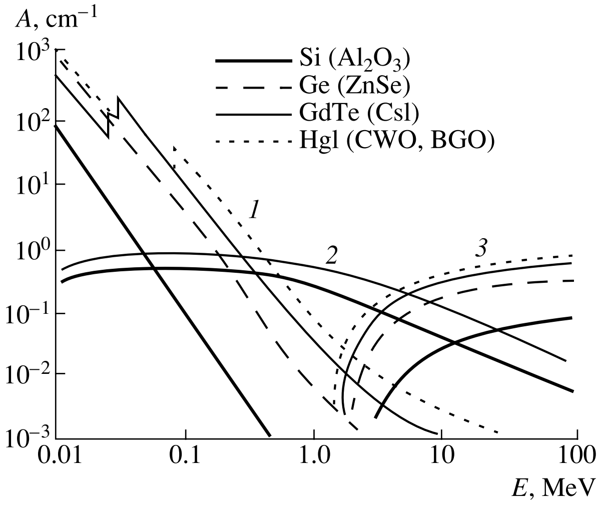

Fig. 1. Linear attenuation coefficients for various γ-radiation absorption channels in typical scintillators employed in radiographic detectors: (*1*) photoeffect; (*2*) Compton scattering; (*3*) pair production. Note the universal character of the energy dependences and the difference in the contributions of various channels to the absorption at medium and high energies.

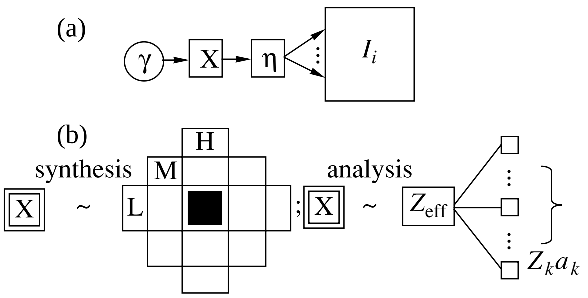

Fig. 2. Schematic diagrams of (a) the multi-energy radiography principle and (b) different approaches to restoration of the object (X) structure: "synthesis" of the object image employs three patterns of typical components possessing low (L), medium (M), and high (H) atomic numbers Z; "analysis" consists in determining the distribution of Z_{eff} over partial contributions $Z_k a_k$.

where η is the detector conversion efficiency, V_0 is the source power (or the background signal level), μ_{ij} are the partial attenuation coefficients of the object, and Q is the number of components (or layers) in the object. Digitization of the signal allows the results of measurements to be obtained in any convenient scale. Let us introduce the logarithmic intensity $I = \ln(\eta V_0/V)$, in which the radiography equations acquire a linear form. If the number of energies N (MER order) is matched to the number of components Q ($N = Q$), we obtain (repeated indexes imply summation):

$$I_i = \mu_{ij}\Delta_j;$$
$$\mu_{ij} = \rho_j[\tau(E_i)Z^4_{\text{eff},\,j} + \sigma(E_i)Z_{\text{eff},\,j} + \chi(E_i)Z^2_{\text{eff},\,j}]; \quad (2)$$
$$i, j = 1, \ldots, N,$$

$$\mu_{ij} \equiv \rho_j\left[\tau(E_i)\sum_{k=1}^{P} a_{jk}Z_k^4 + \sigma(E_i)\sum_{k=1}^{P} a_{jk}Z_k + \chi(E_i)\sum_{k=1}^{P} a_{jk}Z_k^2\right], \quad (3)$$

where τ, σ, and χ are the universal (independent of the substance) energy dependences of the absorption for the photoeffect, Compton scattering, and pair production, respectively; and P is the number of chemical components (e.g., elements in a complex compound). In the energy range 0.01 MeV $\lesssim E \lesssim$ 0.5 MeV employed in most applications, the τ and σ contributions are dominant. In the radiography of large objects employing high-energy beams from accelerators, the σ and χ terms become the most important. Figure 1 shows typical variation of the attenuation coefficients for various absorption channels.

In the traditional approach, the image of an object studied is synthesized from "phantoms" corresponding to the materials with certain standard properties, as is schematically illustrated in Fig. 2. In other words, the absorption coefficients μ_{ij} for the radiation energies measured by each detector of the multi-energy system are assumed to be known. A basis set is determined for the most typical substances in each class of compounds. For example, in medical two-energy (2E) radiography, these are calcium phosphate (representing solid bone tissues) with $Z_{\text{eff}}[Ca_3(PO_4)_2] = 17.38$ and water (soft tissues) with $Z_{\text{eff}}[H_2O] = 7.95$. In technical applications, a typical set includes carbon (representing low-Z organic components) with $Z_L = 6$ and iron (high-Z inorganic substances) with $Z_H = 26$. In the more exact 3E radiography, the components are subdivided into three ranges, including substances with low ($1 < Z_L < 10$), medium ($10 < Z_M < 18$), and high ($18 < Z_H < 40$) atomic numbers. Improperly selected basis set (Z_L, Z_M, Z_H) leads to increased errors in the reconstruction of components. For example, the pattern of a component with a low Z_{eff} can be replaced by a "synthesized" image of an object possessing a higher Z_{eff} at a lower thickness. Errors of this kind increase for different materials with close Z_{eff}.

Let us replace the initial data I_i by the auxiliary parameters $I'_i = D_{ii'}I_{i'}$ obeying the relationships

$$I'_i = D_{ii'}\mu_{i'j}\Delta_j = (D_1\Delta_1; \ldots; D_N\Delta_N). \quad (4)$$

This implies a spatial separation of the patterns corresponding to different basis $Z_{\text{eff},\,j}$ and ρ_j values. Each I'_j value reflects the content of the jth component in the object studied. The parameters D_j are uniquely determined. Relationships (4) give $N(N-1)$ of the total of N^2 undetermined coefficients of the $D_{ii'}$ matrix. The remaining relations correspond to the scale invariance of the linear relationships $I \propto I'$. Any N coefficients (or their combinations) in $D_{ii'}$ can be selected arbitrarily (this ambiguous choice also influences the efficacy of recognition of the object images obtained in various components). Thus, the I_i' values depend only on the I_i data.

In particular, we obtain for the 2E-radiography (selecting $D_{12} = D_{22}$):

$$I_{\mathrm{H}} = I_1' = \frac{\mu_{2\mathrm{H}}}{\mu_{1\mathrm{H}}} I_1 - I_2; \quad I_{\mathrm{L}} = I_2' = I_2 - \frac{\mu_{2\mathrm{L}}}{\mu_{1\mathrm{L}}} I_1; \quad (5)$$

$$\mu_{i\mathrm{H,\,L}} = \mu(E_i;\, Z_{\mathrm{H,\,L}}); \quad i = 1, 2.$$

The analogous expressions for (I_{L}' ; I_{M}' ; I_{H}') in 3E radiography are more cumbersome. In the general case, we obtain closed systems of relations $I_j' = f_j(I_i;\, \mu_{ij})$ and $\Delta_j = \mu_{ji}^{-1} I_i$, where μ^{-1} is the inverse matrix. In order to determine the Δ_j values, it is necessary that $\det\mu_{ij} \neq 0$, which implies that $E_i \neq E_{i'}$ for $i \neq i'$. Note that the recognition of patterns corresponding to Z_{H} and Z_{L} is impossible within the framework of monoenergetic radiography. Indeed, for $E_1 = E_2$, we obtain $I_{\mathrm{H}} = -I_{\mathrm{L}} = I_1 - I_2 \equiv 0$ because $I_1 = I_2$. Using the digitized data on $I_j' \sim \Delta_j$ and special software, a computer restores the object image with thickness-resolved components.

The approach described above stipulated no quantitative determination of the parameters Z_{eff}, ρ, and a_k. The "synthesis" of the object structure was essentially qualitative, since the object was characterized only with respect to the presence of components with high (Z_{H}), medium (Z_{M}), or low (Z_{L}) atomic numbers. Should an object be composed of elements with close atomic numbers ($Z_{\mathrm{eff,\,1}} \simeq Z_{\mathrm{eff,\,2}}$), the corresponding patterns will be indistinguishable; resolving the patterns would require a higher order of MER, which implies considerable technical complications. Let us use the radiography data for an "analysis" of the object structure. For this purpose, we assume the object thickness to be fixed and introduce the layer density $\varrho_i = \rho_i\Delta$. Now select the radiation energy ranges so that, for one (or more) of these, at least two absorption channels are significant. This would require a certain adjustment of the radiation detectors as well, but it is always possible to select the required parameters (and scintillators). This "multichannelness" is a necessary condition for determination of the chemical compositions. However, this property alone is insufficient. An important feature is that the character of absorption and the influence of Z_{eff} on the absorption in the employed absorption channels are different. It is this difference that allows both qualitative and quantitative information about the corresponding object structure to be extracted from the results of measurements.

We can distinguish between the cases of a "rough" 2E-monitoring, whereby only Z_{eff} and ϱ are determined, and "fine" analysis involving restoration of the a_k concentrations for a set of P components. In order to solve the problem, the number of energies N (MER order) has to be matched to the number of components P. Below, we proceed from the equations

$$I_i = \tau(E_i)z_\tau + \sigma(E_i)z_\sigma; \quad i = 1, 2;$$
$$z_\tau = \varrho Z^4, \quad z_\sigma = \varrho Z; \quad Z \equiv Z_{\mathrm{eff}}; \quad (6)$$

$$I_i = \lambda_{ik} a_k; \quad \lambda_{ik} = \varrho[\tau(E_i)Z_k^4 + \sigma(E_i)Z_k];$$
$$i, k = 1, \ldots, N, \quad (7)$$

where only two channels (the photoeffect and the Compton scattering) are taken into account. By the same token, we can readily obtain equations for the three-channel radiography including the pair production channel. It can be noted (without proof) that the three-channel 3E-radiography allows the spatial and atomic structure of an object to be completely restored, by independently determining the atomic number Z_{eff}, density ρ, and thickness Δ.

Equations (6) and (7) can be readily solved. In order to close the system, it is necessary to exclude all quantities independent of the results of radiographic measurements. This can be done upon preliminary tests with the samples of known composition and geometry (Z_j^*, ρ_j^*, Δ_j^*). As a result, the coefficients τ and σ, as well as the energy dependences of λ, are expressed through the calibration coefficients $C_{ij} = I(E_i;\, Z_j^*,\, \rho_j^*,\, \Delta_j^*)$. For the NE-radiography, it is necessary to perform N^2 calibration measurements.

According to the above, a four-dimensional calibration basis is sufficient for the 2E-radiography. Omitting intermediate transformations, we present expressions for the "rough" monitoring at medium energies:

$$Z_{\mathrm{eff}} = Z_{\mathrm{eff}}(I_1, I_2)$$
$$= \sqrt[3]{\frac{Z_1^{*4}\varrho_1^*(C_{12}I_2 - C_{22}I_1) - Z_2^{*4}\varrho_2^*(C_{11}I_2 - C_{12}I_1)}{Z_1^*\varrho_1^*(C_{12}I_2 - C_{22}I_1) - Z_2^*\varrho_2^*(C_{11}I_2 - C_{12}I_1)}}; \quad (8)$$

$$\varrho = \varrho(I_1, I_2)$$
$$= \frac{Z_1^*\varrho_1^*(C_{12}I_2 - C_{22}I_1) - Z_2^*\varrho_2^*(C_{11}I_2 - C_{12}I_1)}{(C_{11}C_{22} - C_{12}C_{21})}\left(\frac{1}{Z_{\mathrm{eff}}}\right). \quad (9)$$

Simple but cumbersome expressions for the "fine" quantitative analysis are not presented here. Solutions (8) and (9) exist under the conditions

$$C_{11}C_{22} - C_{12}C_{21} \neq 0; \quad Z_1^* \neq Z_2^*, \quad (10)$$

which require using sufficiently different energy ranges of detected radiation and selecting control samples of sufficiently different compositions.

The $2E$-radiographic chemical analysis of an object should be performed in two steps. First, a "rough" structure of the object is determined using Eqs. (8) and (9). Then, the a_k concentrations of elements mostly contributing to the effective atomic number are refined for the elements possessing close values of $Z_k \simeq Z_{\text{eff}}$. If necessary, some other basis values of $Z_k \leq Z_{\text{eff}}$ are used in order to determine the content of minor elements. Once the effective atomic composition is established, additional NE-radiography can provide for the data about thickness of all individual N components in the object. Using modern computer facilities, all these procedures can be performed simultaneously.

Thus, using multichannel multi-energy radiography, it is possible to determine the structural parameters of multicomponent objects and distinguish chemical compounds with close atomic compositions. The number of structural parameters which can be restored from the results of measurements increases with the number (not less than two) of absorption channels and detection energies. This opens wide prospects for using this method for both basic experimental investigations and nondestructive testing applications.

REFERENCES

1. *Abstracts of the 15th World Conference on Non-Destructive Testing (Session of Methods and Instrumentation), Rome, 2000.*
2. E. V. Astrova, A. D. Remenyuk, A. G. Tkachenko, and I. L. Shul'pina, Pis'ma Zh. Tekh. Fiz. **26** (24), 31 (2000) [Tech. Phys. Lett. **26**, 1087 (2000)].
3. R. M. Harrison, Nucl. Instrum. Methods Phys. Res. A **310**, 24 (1991).
4. *Heimann Systems: Prospects* (Germany, 2001), available on Internet web-site http://www.heimannsystems.com.
5. L. Grodzins, Nucl. Instrum. Methods Phys. Res. B **36**/**37**, 829 (1991).
6. V. V. Ivanov, *Course of Dosimetry* (Atomizdat, Moscow, 1978).
7. V. B. Berestetskii, E. M. Lifshitz, and L. P. Pitaevskii, in *Course of Theoretical Physics*, Vol. 4: *Quantum Electrodynamics* (Nauka, Moscow, 1989; Pergamon, Oxford, 1982).
8. O. F. Nemets and Yu. V. Gofman, *Handbook of Nuclear Physics* (Naukova Dumka, Kiev, 1975).

Translated by P. Pozdeev

Technical Physics Letters, Vol. 28, No. 5, 2002, pp. 361–364. Translated from Pis'ma v Zhurnal Tekhnicheskoĭ Fiziki, Vol. 28, No. 9, 2002, pp. 14–21.
Original Russian Text Copyright © 2002 by Sorokin.

Electron Beam Formation in an Open Discharge: Part 2. Does the Photoelectron Mechanism Work?

A. R. Sorokin
Institute of Semiconductor Physics, Siberian Division, Russian Academy of Sciences, 630090 Novosibirsk, Russia
e-mail: IFP@isp.nsc.ru

Received December 3, 2001

Abstract—The qualitative pattern of electron beam formation in discharges of various types, including hollow-anode, anomalous, and open, is considered from the most general standpoints. The considerations confirm the conclusion made by the author previously: atom-induced electron emission ensures a high efficiency of the electron beam formation, provided that sufficiently fast atoms are formed in the recharge process, which is consistent with commonly accepted notions about the glow discharge. Examples of the general character are presented which indicate that the open discharge is incompatible with the photoelectron mechanism, although publications in favor of the latter model still appear. The latest of such publications is critically analyzed. *© 2002 MAIK "Nauka/Interperiodica".*

1. Below we will again discuss the question as to whether the open discharge in systems with a grid anode is induced by photoelectrons (that is, self-sustained by photoemission from the electron beam drift space behind the grid [1–3]) or it is a kind of glow discharge with anode plasma [4, 5]. This paper is a reply to the recent publication [6] in which the authors insist on the photoelectron mechanism of open discharge induction.

A glow discharge with anode plasma has been widely used in electron-beam tubes since the second half of 19th century; since the 1960s, this type of discharge has been employed in technological electron guns with a hollow anode (in the simplest case, with a flat pinhole anode). It was reliably established long ago [7] that the discharge in this system is sustained by a flow of ions supplied from the anode plasma region. Penetration of a strong electric field into this region (where $E/p > 150$ V/(cm Torr) for the discharge in helium) is hindered because electrons "avoid" collisions and the ionization is very weak. Photoemission from the cathode is assumed to be small and usually ignored.

The main purpose of this paper is to consider qualitatively (without aspiring to absolute exactness) from the most general standpoints the features of electron beam formation in discharges of various types for checking whether these features can place open discharge outside the well-known forms of glow discharge. We will also analyze the experimental results recently reported in [6].

2. The consideration is based on a nontraditional classification of the forms of glow discharge suggested in [8], which most simply and clearly reflects the physical essence of the discharge phenomenon (Fig. 1). In the diagram of Fig. 1, region *1* corresponds to the simplest discharge (whereby the field in the gap is weakly distorted by charged particles), region *2* represents a dense discharge (significant distortion of the field), and region *3* corresponds to the normal glow discharge. For the simplest discharge, a section in the (U, pd) plane gives the Paschen curve, while a section in the (U, j) plane represents a current–voltage (I–U) characteristic.

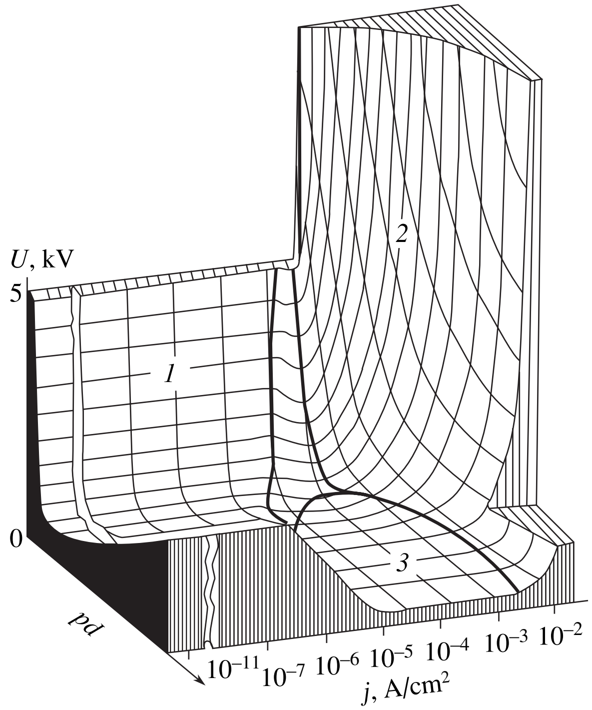

Fig. 1. A diagram in the (U, j, pd) coordinates illustrating the types of glow discharge (see the text for explanation) [8].

1063-7850/02/2805-0361$22.00 © 2002 MAIK "Nauka/Interperiodica"

As can be seen, the character of the current buildup for the dense discharge is the same on the left- and right-hand branches of the Paschen curve. If we take the ratio of the current to the working discharge area (rather than to the total cathode surface) on the *j* axis in the normal glow discharge region (which is the only reasonable course of action), then the trough in region *3* of Fig. 1 will disappear and the similarity of both branches of the *I*–*U* curve will be even more pronounced.

In the course of the electric breakdown of the gap on the right-hand branch of the *I*–*U* curve (where the electron avalanches can freely develop), the current in one of the avalanches becomes (as a result of fluctuations) sufficient for significantly distorting the field. As a result, the field strength at the cathode exhibits a local increase, a cathode potential fall is developed, and the negative feedback mechanism becomes more effective, whereby electrons are emitted at a higher rate from the cathode bombarded by heavy particles. As a result, the voltage *U* drops and the current is limited by a ballast resistance. This regime also determines the cathode area involved in the discharge (in the other part of the cathode surface, the discharge is quenched as a result of decreasing *U*). Upon a slight increase in *U*, the appearing excess ions spread aside from the discharge column and the cathode area involved in the discharge increases. As a result, *U* drops to the initial level and so on, until the discharge spreads over the whole cathode surface. The further increase in *U* gives rise to a dense discharge.

In addition, note that the current buildup on the left-hand branch of the *I*–*V* curve is accompanied by spreading of the negative glow into the gap and by the cathode potential fall development. As the voltage *U* increases, the field tends to concentrate in the cathode fall region so that hindrances to the electron avalanche development are gradually removed. For the discharge in helium, the hindrances are completely removed when $j/p^2 = 2.5 \times 10^{-12}U^3$ [9] (j/p^2 [A/(cm Torr)^2]; U [V]) and the cathode potential fall region is completely formed. As the current grows, the length of this region tends to a minimum value of $l_\mathrm{m} = 0.37(pl)_\mathrm{n}p^{-1}$, where $(pl)_\mathrm{n}$ refers to the normal discharge. In a pulsed regime, the discharge in the initial stage (left-hand branch) is always hindered.

On the right-hand branch, the negative glow and the completely formed cathode potential fall are still present in the form of a normal discharge. However, this discharge is essentially a dense discharge.

3. Let us proceed to electron beams and begin with the situation in a hollow-anode discharge. Deep in the left-hand branch of the *I*–*U* curve, a trans-anode plasma is formed in a weak field sagging in the anode hole. Traveling by the curved field lines, heavy ions, together with fast atoms, appear in the course of the recharge process produce emission only in the central cathode region. As a result, a narrow electron beam is formed representing essentially a simplest discharge enhanced by the flow of ions supplied from the trans-anode plasma region.

On the right-hand branch of the *I*–*U* curve (as well as on the left-hand branch, provided that the cathode potential fall region *l* accounts for only a part of the discharge gap width *d*), a near-anode plasma is formed and the electron beam spreads over the entire hole aperture. This is essentially a dense discharge. If the hindrances are incompletely removed, the discharge is enhanced due to ionization in the residual field sagging in the anode hole.

The efficiency ξ of the electron beam formation, defined as the ratio of the beam current to the total current (or, more exactly, as the ratio of the corresponding powers), is determined by a generalized emission coefficient $\gamma = \gamma_i + \gamma_a$, so that $\xi = \gamma(\gamma + 1)^{-1}$ [7]. Typical working gas pressures in the electron guns with hollow anodes are on the order of 10^{-2}–10^{-1} Torr, while typical voltages amount to 10^1–10^2 kV.

When the discharge hindrances are completely removed, the parameters can change rather slightly if the anode is continuous and arbitrarily arranged (e.g., aside from the cathode) so as not to cross the beam, as was noted in [10]. In order to ensure a high efficiency of ξ, it is only necessary to provide that the velocity of ions in the cathode fall region would be sufficiently high for the effective emission γ. This corresponds to the well-known anomalous discharge, representing a special case of the dense discharge with a completely formed cathode fall region.

If many hollow-anode discharges are switched in parallel (e.g., using a grid anode), we obtain open discharge [1]. In this case, the conditions of effective electron beam formation over a large area can be satisfied at pressures of up to 10^2 Torr, provided that A, $d < 1$ mm (A is the characteristic hole size in the grid anode). The working voltages typically do not exceed 15–20 kV. The coefficient η of beam penetration into the drift space falls within the interval from ξ to $\xi\mu$, where μ is the geometric transparency of the grid; $\eta \approx \xi$ if the current to the grid is small (as in the case of the simplest discharge [11, Fig. 2] or in the initial stage of a dense discharge [3, Fig. 1] with pulsed excitation). It should be noted that differences in using the hollow-anode and open discharge regimes are determined only by the features of particular applications.

4. In [1], we suggested a nontraditional mechanism of open discharge operation—the photoelectron mechanism, which was most clearly formulated in [2]. According to this mechanism, the open discharge is essentially non-self-sustained: it is initiated and sustained by UV emission from a trans-anode region. From this standpoint, the ionization process is a negative factor reducing the efficiency. The photoemission-initiated discharge concept was criticized, first in [4] and then in subsequent publications, as summarized in [5]. These papers demonstrated that the open discharge, as well as the hollow-anode discharge, retain all

properties of the well-known forms of glow discharge, while the photoelectron mechanism shows a number of deep and unsolvable discrepancies with experiment.

The discrepancies are numerous and, especially important, are all of a general and basic character. The most obvious are as follows. For a photoelectron-induced discharge, the photoemission coefficient γ_v must exceed unity—otherwise the discharge will not be initiated (γ_v implies the number of electrons emitted from the cathode due to the photoeffect, per electron reaching the drift space). In this case, the current would increase up to a value limited by the “3/2” power law. However, such currents are never reached.

One can examine an arbitrary (this is emphasized) typical oscillogram, such as that reported in [3, Fig. 1], to observe the following: the beam current begins to drop under the conditions most favorable for the excitation of photoemission—that is, on the fall of U [4], where the velocity of electrons is not as large. It is generally unclear why the photoelectron-induced discharge requires overstated U values in order to provide for growth of the beam current and the efficiency, as observed in all the known experiments, including those with laser media. In these experiments (see, e.g., [12]), transparency of the active media was too high for the electron beams, which hindered full realization of the potentially high efficiency of open-discharge lasers. From the standpoint of the photoelectron-induced discharge, it would be sufficient to reduce the voltage, thus increasing the beam current and the efficiency. In the experiment, however, a decrease in U leads to a drop in both the anode current and to an even more pronounced drop in the beam current and laser efficiency.

Upon considering, for example, the curves reported in [2, Fig. 3], a question arises as to why it is necessary, under photoelectron-induced discharge conditions, to reduce the pressure (and, hence, decrease the beam–gas interaction) and increase the voltage (decreasing the interaction still more) in order to maintain the beam current.

Why do the beam current and the discharge current [13, Fig. 3] remain unchanged (or even increase, as in [5, Fig. 6]) when the area of photoemission is increased by moving the collector near the anode grid? The number of such questions of rather basic character can be increased. Consider one more example.

It was pointed out [5, Fig. 4] that the plot of current versus discharge gap width d (Fig. 2) typical of the open discharge is also characteristic (cf. Fig. 1) of the glow discharge. This behavior is absolutely inconsistent with the mechanism of photoelectron-induced discharge, since we are speaking of a change in the current by two orders of magnitude. Then, what is the photoelectron-induced discharge for? It can by no means depend so strongly on the gap width d. It should be emphasized that the efficiency ξ was retained close to unity even for d exceeding l_n for the normal discharge, when the presence of holes in the anode does not influence the discharge parameters (and, hence, using the term “open discharge” is senseless).

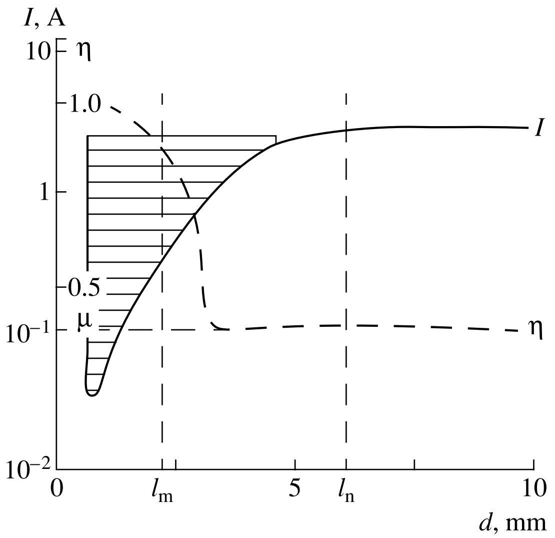

Fig. 2. Plots of the total current I and the electron beam propagation η versus interelectrode distance d [5] for a discharge operated at a voltage amplitude of U_0 = 10.8 kV and helium pressure p_{He} = 2.2 Torr.

The above analysis of the electron beam formation under various conditions of glow discharge is based on the most general principles and, hence, can be generalized to include the entire range of conditions realized in practice for the open discharge. It is important to emphasize once more that the glow discharge with a positive I–V characteristic, which is most frequently employed as the open discharge, belongs, under arbitrary pd conditions, to the same type (dense discharge) and, hence, is controlled by the same mechanism of electron beam generation. This by no means implies that the electron beam can be obtained under arbitrary conditions (e.g., under arbitrary pressure p). Limitations arise as a result of the development of instabilities in the near-cathode region (due to a high intensity of the electric field at the cathode surface).

5. In conclusion, let us analyze the results of experiments [6] in which an additional grid spaced by 2 mm from the grid anode (both grids with A = 0.2 mm) and connected to the anode was mounted outside the acceleration gap (d = 1 mm, U = 2.4 kV, p_{He} = 16 Torr). An auxiliary discharge (U = 0–35 V) between the grid and collector (spaced by 20 mm, with plus on the collector) led to an increase (up to twofold) in the current through the acceleration gap, which was interpreted as being due to additional photoemission from the auxiliary discharge.

In these experiments, the current in the acceleration gap was one order of magnitude lower than the value required by the j/p^2 parameter for the complete formation of the cathode potential fall region. Therefore, the discharge is operated at the expense of the field sagging, whereby the regime is significantly influenced by conditions at the anode grid, in particular, by the presence of closely spaced additional electrodes, sources of charged particles, etc. Consider an example: if a grounded electrode approaches (or touches) a discharge tube on the drift space side near the grid in a regime close to the simplest discharge, the resulting change in the sagging field distribution leads either to a decrease in the current [11, Fig. 1] or even to the discharge quenching (can this effect also be explained by the photoelectron-induced discharge?).

In fact, the current buildup observed in [6] was caused by the field of the auxiliary discharge (E/p = 0–1.1 V/(cm Torr)), which induced an additional ion flow toward the grids. This flow is trapped by the field sagging in the acceleration gap (at the auxiliary grid position, calculation [14] yields E/p = 0.95 V/(cm Torr)). Note that the parameter E/p is close to the value $E/p \approx$ 1 V/(cm Torr) typical of the positive column of a normal glow discharge.

To summarize, there are more than necessary arguments, all of general and basic character, evidencing inconsistency of the photoelectron mechanism of initiation of open discharge. Therefore, there is no need to draw attention to some partial effects for which it is frequently difficult to give an unambiguous interpretation. Such effects are numerous but, upon thorough consideration, only provide additional evidence for predominance of the atom-induced electron emission. This concept agrees with the commonly accepted notions about glow discharge and is confirmed by recent calculation of the open discharge [15].

Acknowledgments. The author is grateful to A.A. Chernenko for calculation of the field sagging in the grid anode.

REFERENCES

1. P. A. Bokhan and A. R. Sorokin, Zh. Tekh. Fiz. **55** (1), 88 (1985) [Sov. Phys. Tech. Phys. **30**, 50 (1985)].
2. G. V. Kolbychev, P. D. Kolbycheva, and I. V. Ptashnik, Zh. Tekh. Fiz. **66** (2), 59 (1996) [Tech. Phys. **41**, 144 (1996)].
3. G. V. Kolbychev, Opt. Atmos. Okeana **6** (6), 635 (1993).
4. A. R. Sorokin, Pis'ma Zh. Tekh. Fiz. **21** (20), 37 (1995) [Tech. Phys. Lett. **21**, 832 (1995)].
5. A. R. Sorokin, Zh. Tekh. Fiz. **68** (3), 33 (1998) [Tech. Phys. **43**, 296 (1998)].
6. A. P. Bokhan and P. A. Bokhan, Pis'ma Zh. Tekh. Fiz. **27** (6), 7 (2001) [Tech. Phys. Lett. **27**, 220 (2001)].
7. M. A. Zav'yalov, Yu. E. Kreĭndel', A. A. Novikov, and L. P. Shanturin, *Plasma Processes in Electron Guns* (Énergoatomizdat, Moscow, 1989).
8. B. N. Klyarfel'd, L. G. Gusaeva, and A. S. Pokrovskaya-Soboleva, Zh. Tekh. Fiz. **36** (4), 704 (1966) [Sov. Phys. Tech. Phys. **11**, 520 (1966)].
9. K. A. Klimenko and Yu. D. Korolev, Zh. Tekh. Fiz. **60** (9), 138 (1990) [Sov. Phys. Tech. Phys. **35**, 1084 (1990)].
10. Z. Yu, J. J. Rocca, and G. J. Collins, J. Appl. Phys. **54** (1), 131 (1983).
11. A. R. Sorokin, Pis'ma Zh. Tekh. Fiz. **22** (13), 17 (1996) [Tech. Phys. Lett. **22**, 526 (1996)].
12. P. A. Bokhan and A. R. Sorokin, Pis'ma Zh. Tekh. Fiz. **10** (10), 620 (1984) [Sov. Tech. Phys. Lett. **10**, 262 (1984)].
13. P. A. Bokhan and G. V. Kolbychev, Zh. Tekh. Fiz. **51** (9), 1823 (1981) [Sov. Phys. Tech. Phys. **26**, 1057 (1981)].
14. V. A. Govorkov, *Electric and Magnetic Fields* (Énergiya, Moscow, 1968).
15. A. R. Sorokin, Pis'ma Zh. Tekh. Fiz. **26** (24), 89 (2000) [Tech. Phys. Lett. **26**, 1114 (2000)].

Translated by P. Pozdeev

Technical Physics Letters, Vol. 28, No. 5, 2002, pp. 365–368. Translated from Pis'ma v Zhurnal Tekhnicheskoĭ Fiziki, Vol. 28, No. 9, 2002, pp. 22–30.
Original Russian Text Copyright © 2002 by Kamzin, Vcherashniĭ.

Simultaneous Gamma, X-ray, and Electron Mössbauer Spectroscopy Measurements at Low Temperatures

A. S. Kamzin and D. B. Vcherashniĭ
Ioffe Physicotechnical Institute, Russian Academy of Sciences, St. Petersburg, 194021 Russia
e-mail: KAMZIN@Cityline.spb.ru

Received November 22, 2001

Abstract—A low-temperature setup is described that allows the Mössbauer spectra to be measured with simultaneously detecting gamma quanta, characteristic X-ray radiation, conversion electrons, and Auger electrons in a range of temperatures from 10 K to room temperature. The system comprises a low-temperature detector of electrons, mounted inside a cryostat, and the counters of gamma and X-ray quanta mounted outside the cryostat. Thus, the system implements the method of simultaneous gamma, X-ray, and electron Mössbauer spectroscopy (SGXEMS) proposed in [5] and allows the measurements to be performed in a broad temperature range (from room temperature down to 10 K) with simultaneous investigation of the volume, subsurface, and surface layers of macroscopic crystal samples. © *2002 MAIK “Nauka/Interperiodica”.*

Introduction. The investigation of basic phenomena in the surface layers of macroscopic samples and the detection of changes in the properties of crystals on the passage from bulk to surface require methods capable of simultaneously probing the bulk and surface layers of samples and directly comparing the experimental data. The results of our preliminary investigations [1–3] showed that these possibilities are offered by the method of simultaneous gamma, X-ray, and electron Mössbauer spectroscopy (SGXEMS) originally proposed and developed in [4–7]. This method is also called simultaneous triple radiation Mössbauer spectroscopy (STRMS) [8].

The essence of the SGXEMS method consists in simultaneously measuring the Mössbauer spectra by detecting radiation possessing different ranges in substances: gamma quanta, characteristic X-ray radiation, conversion electrons, and Auger electrons. Previously [5], we proposed the design of a three-chamber detector unit allowing three counters to separately detect γ quanta, X-ray radiation, and electrons. The first detector chamber measures gamma quanta in the transmission geometry, while the second and third chambers detect X-ray radiation and electrons (conversion and Auger), respectively, in the backscattering geometry. The Mössbauer spectra measured with this three-chamber detector unit can provide information about the state of material in the bulk, in a surface layer with a thickness of several microns, and in the outermost surface layer with a thickness not exceeding 300 nm (for magnetic dielectrics and metals studied with the aid of a ^{57}Fe isotope). Using the experimental techniques described in [5–7], it is possible to expand the temperature range of SGXEMS from room temperature up to 850 K.

We have developed the SGXEMS system based on proportional flow detectors which are widely used for detecting low-energy radiations. This is explained by the simplicity of manufacturing detectors for various experimental setups, good energy resolution, and high efficacy of detection in comparison with detectors of other types. The requirements of some experimental techniques (such as Mössbauer spectroscopy of conversion electrons) where the radiation has to be detected in a broad temperature range led to the development of both high-temperature [5, 9] and low-temperature [10, 11] detectors of low-energy (below 15 keV) electrons. However, the conditions of operation of the proportional detectors at temperatures different from room temperature have still been incompletely studied. A more effective use of such detectors is possible provided that their possibilities would be studied in more detail. Thus, development of the physics of surfaces posed the task of elaborating facilities extending the domain of SGXEMS measurements far below room temperature.

Below we describe a proportional flow counter for detecting electrons in broad temperature range from room temperature down to 10 K. The low-temperature detector of electrons, in combination with detectors of gamma quanta and characteristic X-ray radiation, allows the SGXEMS system [5–7] to be applied to investigations of the bulk and surface properties of crystals in this broad temperature range.

System design. Thus, the proposed SGXEMS system measures gamma quanta, characteristic X-ray radi-

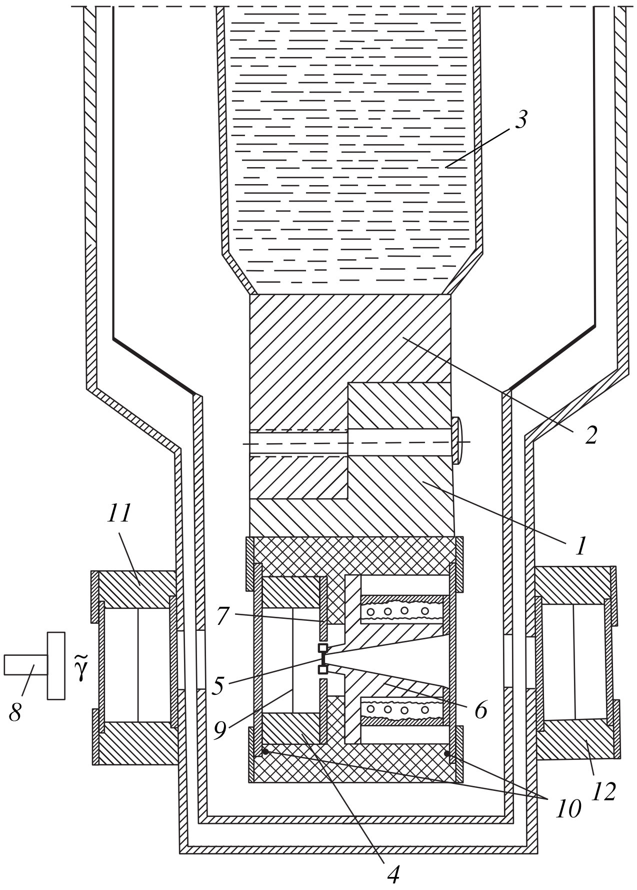

Fig. 1. Schematic diagram of a low-temperature detector unit for SGXEMS measurements: (*1*) copper holder; (*2*) heat-exchanger rod; (*3*) cooling agent (liquid helium or nitrogen); (*4*) electron detector case; (*5*) sample crystal; (*6*) heater; (*7*) beryllium foil windows; (*8*) Mössbauer source; (*9*) anode; (*10*) grooves for indium wire gaskets; (*11*) X-ray detector case; (*12*) gamma counter case.

ation, conversion electrons, and Auger electrons using proportional gas flow detectors. The reasons for selecting these detectors were mentioned above. The system is mounted in a cryostat schematically depicted in Fig. 1. The main difficulty encountered in selecting a flow detector for the measurement of conversion and Auger electrons is as follows. The sample has to be mounted immediately in the detector of electrons because no materials “transparent” for electrons are available for cryostat windows. Therefore, the flow detector must occur and operate at temperatures in the entire range in which the Mössbauer spectra of a given crystal have to be measured. In our system, the electron detector was mounted on a copper holder *1* fastened to a protrusion of rod *2* brazed to vessel *3* containing a cooling agent (liquid helium or nitrogen, depending on the temperature range studied). When the experiments are conducted at temperatures far from the boiling point of the cooling agent, additional thermoinsulating spacers are placed between holder *1* and rod *2* in order to decrease the heat transfer from detector to vessel *3*. In addition, the spacer provides for the elimination of vibrations caused by intensive boiling of the cooling agent. Transferred from vessel *3* via holder *1* to the electron counter, these vibrations hinder the Mössbauer measurements.

The case of electron detector *4* is made of duralumin. A sample crystal *5* placed on heater *6* is mounted in a beryllium window *7*, bounding the working volume of detector *4* on one side. On the opposite side, the detector is closed by a beryllium foil window through which gamma radiation is transmitted from the Mössbauer source *8* to the sample studied. Heater *6* represents a copper flange on which a 0.3 mm nichrome wire is wound above an insulating film. The temperature is monitored by a copper–constantan thermocouple fastened to the crystal studied. Another thermocouple, mounted directly on the heater, serves as a sensor in the electronic system of temperature stabilization by controlling current passing through the nichrome heater coil. Anode *9* in the detector represents a gold-coated tungsten filament with a thickness of 30 μm. A working gas mixture is supplied to the working zone of the detector and is discharged from it via tubes brazed to the holder. The working gas is insulated from a vacuum jacket of the cryostat by indium wire gaskets put into special grooves *10*.

Detector *11*, measuring the characteristic X-ray radiation from the crystal in the backscattering geometry, is mounted on the outer front window of the cryostat (Fig. 1). The counter is provided with a duralumin case and has a working volume of $8 \times 30 \times 40$ mm. The gamma quanta are measured in the transmission geometry with the aid of detector *12* mounted on the opposite beryllium window of the cryostat (Fig. 1). In both gamma and X-ray counters, beryllium windows and duralumin cases serve as the cathodes, while the anodes are made of a 30-μm-thick gold-coated tungsten filament. As can be seen from Fig. 1, the detectors of gamma quanta (*11*) and X-ray radiation (*12*) occur outside the cryostat and operate at room temperature. The conditions of room-temperature operation of such detectors are well known (see, e.g., [10]). As was demonstrated previously [5–7], a good energy resolution and high efficacy of the gamma and X-ray counter operation are ensured by using an Ar + 5% CH_4 working gas mixture. Based on these results, we also employed the Ar + 5% CH_4 working mixture in the gamma and X-ray detectors (*11* and *12*, Fig. 1) in the system described here.

The main difficulty encountered in the use of proportional flow detectors of electrons operating at temperatures different from room temperature is selecting a working gas ensuring a maximum efficacy of the radiation detection under the given conditions. We have tried various gases and gas mixtures for the low-temperature detector of electrons. The results of these preliminary experiments showed that a He + 5% CH_4 mixture provides for a virtually constant efficacy in the

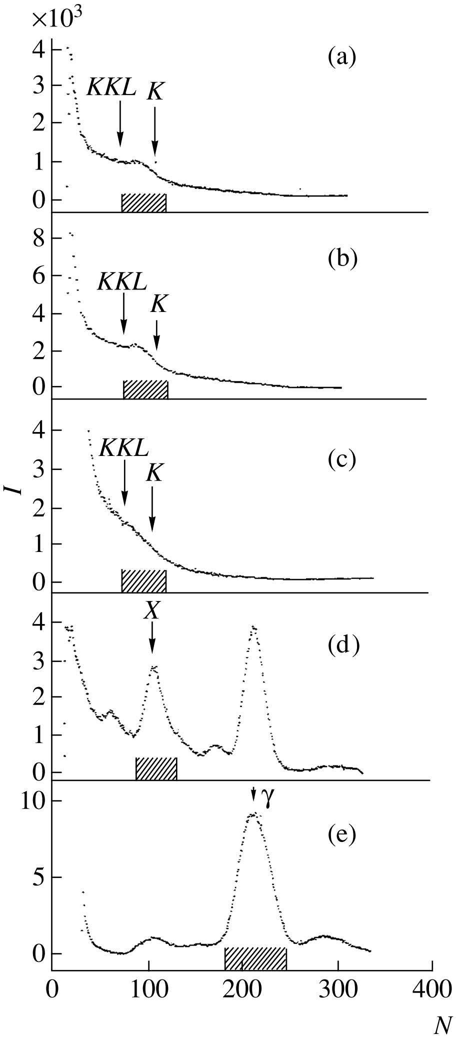

Fig. 2. (a–c) The electron energy spectra of a ^{57}Fe foil measured using the SGXEMS system at 10 (a), 30 (b), and 80 K (c), showing the peaks of (*KLL*) 5.6-keV Auger electrons and (*K*) 7.2-keV conversion electrons. The measurements were performed using Ar + 5% CH_4 (80 K), pure H_2 (30 K), and pure He (10 K) as the working gases. (d, e) The energy spectra of (d) characteristic X-ray radiation and (e) gamma quanta showing the peaks of (*X*) 6.3-keV X-ray radiation and (γ) 14.4-keV Mössbauer gamma quanta. The measurements were performed using the corresponding detectors filled with an Ar + 5% CH_4 working gas mixture.

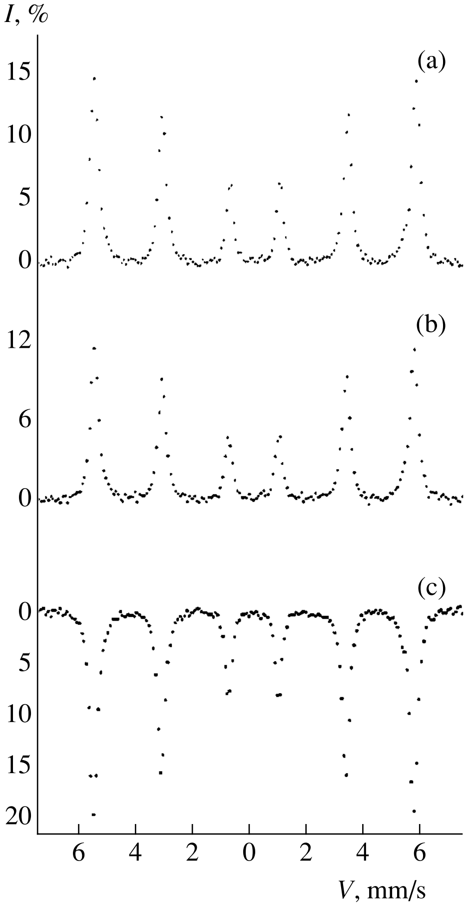

Fig. 3. The Mössbauer spectra simultaneously measured using the SGXEMS system with the detectors tuned to the energy regions cross-hatched in Fig. 2, corresponding to (a) 7.2-keV conversion electrons and 5.6-keV Auger electrons, (b) 6.3-keV characteristic X-ray radiation, and (c) 14.4-keV Mössbauer gamma quanta.

range from room temperature to 77 K, but drops sharply when the temperature decreases below 77 K. The experiments with Ne, He, and H_2 showed that the best results in the temperature interval from 77 to 25 K are obtained when the detector is filled with pure hydrogen. This result agrees with the data reported in [11], where effective operation of an electron detector filled with pure H_2 was observed in the range from room temperature down to 15 K. However, the use of hydrogen is significantly limited by a considerable danger of explosion; moreover, as noted in [11], hydrogen frequently reacts with the samples studied. For these reasons, we employed pure hydrogen only for measurements in the temperature interval from 77 to 25 K. In the interval from 25 to 10 K, a sufficiently high efficacy of electron detection was provided by pure helium.

SGXEMS measurements. Using the above-descried low-temperature detector of electrons and a Mössbauer source of gamma quanta (^{57}Co in Rh matrix with an activity of 1.86 GBq), we have measured the electron energy spectra of an iron foil containing 25% ^{57}Fe isotope. Figures 2a–2c show the examples of such spectra measured at 10, 30, and 80 K. The experimental spectra exhibit clear peaks belonging to the Auger electrons with an energy of 5.6 keV and the conversion electrons with an energy of 7.2 keV (*KLL* and *K*, respectively). The fact that the system includes three detectors capable of simultaneously measuring different types of radiation (electrons, gamma quanta, and characteristic X-rays) allows the electron energy spectra to be complemented by the spectra of signals detected by gamma and X-ray counters (Fig. 2d and 2e, respectively). The line observed in Fig. 2d (peak *X*) represents the characteristic X-ray radiation with an energy of 6.3 keV, while the signal in Fig. 2e (peak γ) corresponds to the Mössbauer gamma quanta with an energy of 14.4 keV.

Figure 3 presents the experimental Mössbauer spectra of an iron foil with a natural content of ^{57}Fe isotope measured at 10 K using the SGXEMS system with simultaneously operating detectors of gamma quanta, characteristic X-rays, conversion electrons, and Auger electrons. The energy discriminators of the detectors of electrons, X-ray radiation, and gamma quanta, were adjusted so as to measure the signals at energies in the intervals indicated by cross hatching in Figs. 2c–2e, respectively. A computer processing and analysis of the spectra presented in Fig. 3 in comparison with the analogous spectra measured below room temperature showed that an important parameter, the spectral linewidth, coincides with the values obtained at room temperature.

Thus, we have developed a low-temperature electron detector which allows the SGXEMS method to be used for the investigation of bulk and surface properties of macroscopic crystals in a broad temperature range from room temperature down to 10 K.

Acknowledgments. This study was supported by the Russian Foundation for Basic Research, project no. 01-02-17889.

REFERENCES

1. A. S. Kamzin and L. A. Grigor'ev, Zh. Éksp. Teor. Fiz. **104** (10), 3489 (1993) [JETP **77**, 658 (1993)].
2. A. S. Kamzin and L. A. Grigor'ev, J. Appl. Phys. **75** (10), 7099 (1994).
3. A. S. Kamzin, L. P. Ol'khovik, and V. L. Rozenbaum, Zh. Éksp. Teor. Fiz. **111** (4), 1426 (1997) [JETP **84**, 788 (1997)].
4. A. S. Kamzin, V. P. Rusakov, and L. A. Grigor'ev, in *Proceedings of the International Conference on Physics of Transition Metals, USSR, 1988*, Part 2, p. 271.
5. A. S. Kamzin and L. A. Grigor'ev, Pis'ma Zh. Tekh. Fiz. **16** (16), 38 (1990) [Sov. Tech. Phys. Lett. **16**, 616 (1990)].
6. A. S. Kamzin and L. A. Grigor'ev, Pis'ma Zh. Tekh. Fiz. **19** (8), 50 (1993) [Tech. Phys. Lett. **19**, 245 (1993)].
7. A. S. Kamzin and L. A. Grigor'ev, Pis'ma Zh. Tekh. Fiz. **19** (21), 32 (1993) [Tech. Phys. Lett. **19**, 680 (1993)].
8. U. Gonser, P. Schaaf, and F. Aubertin, Hyperfine Interact. **66**, 95 (1990); P. Schaaf and U. Gonser, Hyperfine Interact. **57**, 2101 (1990).
9. Y. Isozumt, M. Kurakado, and R. Katano, Rev. Sci. Instrum. **52** (3), 413 (1981).
10. G. N. Belozerskiĭ, *Mössbauer Spectroscopy as a Method of Surface Analysis* (Énergoatomizdat, Moscow, 1990).
11. K. Fukumura, A. Nakanishi, and T. Kobayashi, Nucl. Instrum. Methods Phys. Res. B **86**, 387 (1994).

Translated by P. Pozdeev

Technical Physics Letters, Vol. 28, No. 5, 2002, pp. 369–370. Translated from Pis'ma v Zhurnal Tekhnicheskoĭ Fiziki, Vol. 28, No. 9, 2002, pp. 31–35.
Original Russian Text Copyright © 2002 by Danilov, Nechiporuk.

Experimental Investigation of the Quantum Amplification Effect for Magnetostatic Waves in Ferrite–Paramagnet Structures

V. V. Danilov and A. Yu. Nechiporuk
Kiev National University, Kiev, Ukraine
e-mail: chipa@mail.univ.kiev.ua

Received December 14, 2001

Abstract—The effect of quantum amplification of the forward bulk magnetostatic waves (MSWs) in a composite structure of yttrium iron garnet $Y_3Fe_5O_{12}$ (YIG) and Al_2O_3:Cr^{3+} (ruby) was studied. The maximum amplification coefficient at 4.2 and 1.6 K was 12 and 25 dB, respectively. No MSW amplification was observed in an epitaxial structure comprising an YIG film grown on a gadolinium gallium garnet $Gd_3Ga_5O_{12}$ (GGG) substrate, which is explained by a strong paramagnetic absorption of MSWs in the GGG substrate crystal. *© 2002 MAIK "Nauka/Interperiodica".*

Previously [1], we developed a theory describing the quantum amplification of magnetostatic waves (MSWs). The theory referred to structures composed of the yttrium iron garnet $Y_3Fe_5O_{12}$ (YIG) and a paramagnetic maser crystal, in which the microwave MSW field interacts with an inverted spin system of the paramagnet. The coefficient of the quantum amplification of MSWs was calculated by a formula analogous to that employed for traditional traveling-wave ruby masers [2]:

$$G[\mathrm{dB/cm}] = 4.34(\omega d_m - 2\omega_r)/V_g,$$

where V_g and ω_r are the group velocity and relaxation frequency of the wave, ω is the frequency of the operating transition in the paramagnet (ruby), and d_m is the magnetic decrement of ruby characterizing the efficiency of interaction of the MSW and the inverted spin system of ruby. Obviously, amplification is only possible provided that the MSW frequency coincides with the electron paramagnetic resonance (EPR) frequency for the operating transition in ruby. Below we consider the experimental results on the quantum amplification of the forward bulk magnetostatic waves (FBMSWs) interacting with the inverted spin system of ruby at liquid helium temperature.

The selection of FBMSWs for the experimental investigation of quantum amplification in a YIG–ruby structure was based on the following considerations. For a forward bulk MSW, the microwave field also contains a polarization component providing for an optimum interaction with the inverted spin system of the maser crystal (ruby). This circumstance increases the magnetic decrement of ruby (d_m). At the same time, the operating transition frequency in ruby occurs near the upper boundary frequency of FBMSW, where the group velocity of the wave is minimum and (according to the above formula) the efficiency of interaction is maximum. We have selected the operating transition $1 \longrightarrow 2$ and the pumping transition $4 \longrightarrow 1$ (for an

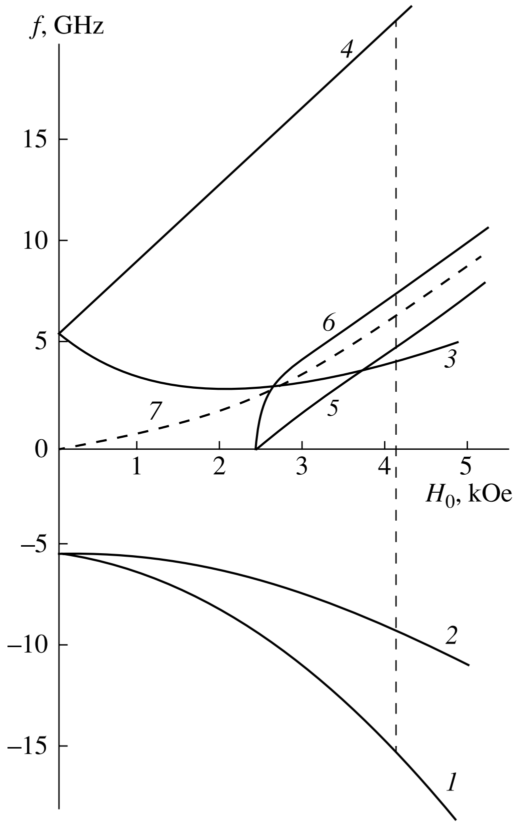

Fig. 1. Frequency–field domains of the existence of FBMSW in YIG and EPR in ruby at liquid helium temperature: (*1–4*) energy levels of Cr^{3+} ion in Al_2O_3; (*5*, *6*) lower and upper boundary frequencies of MSWs; (*7*) frequency of the $1 \longrightarrow 2$ transition in ruby; vertical dashed line indicates the working regime.

1063-7850/02/2805-0369$22.00 © 2002 MAIK "Nauka/Interperiodica"

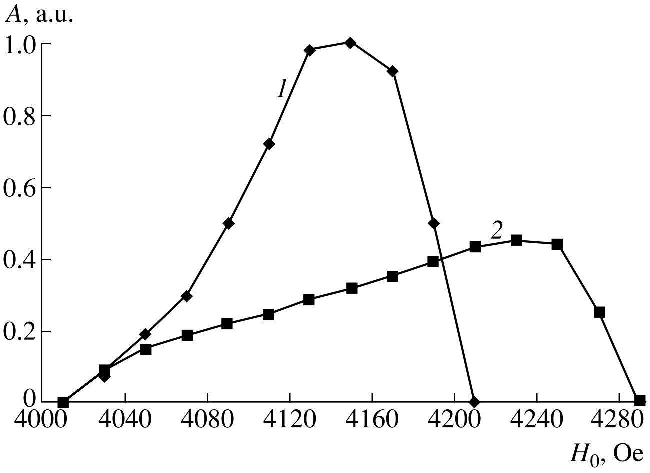

Fig. 2. A comparison of the signal amplitude–field strength characteristics of the FBMSW transmitted through a epitaxial YIG film–ruby structure measured at (*1*) 77 and (*2*) 4.2 K for f_s = 6100 MHz.

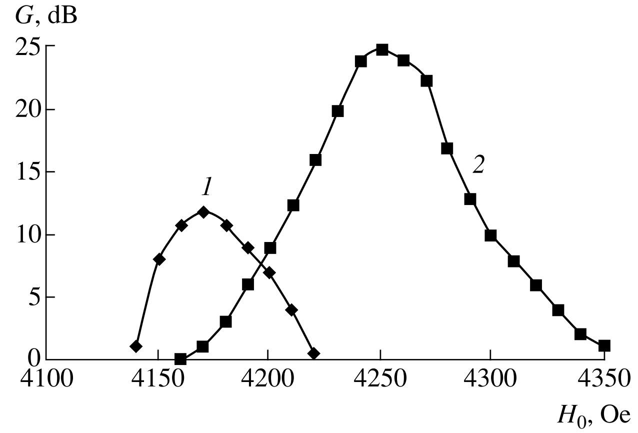

Fig. 3. Experimental plots of the quantum amplification of FBMSWs in a structure composed of 200-μm-thick single crystal plates of YIG and ruby at (*1*) 4.2 and (*2*) 1.6 K for f_s = 6100 MHz.

angle of 90° between the external magnetic field $\mathbf{H}_0$ and the symmetry axis **C**, see Fig. 1).

In the experiments, we have studied parameters of the microwave power transmission through the system of excitation and detection of the MSW energy at an operating (signal) transition frequency of f_s = 6100 MHz. The ruby crystal was pumped from a magnetron generator operating at f_p = 35520 MHz, providing for a power level of up to 3 W.

Figure 2 shows a comparison of the signal amplitude–field strength characteristics of the FBMSW transmitted through a ruby–epitaxial YIG film structure measured at 4.2 and 77 K. As was demonstrated previously [3] (see also [4]), a gadolinium gallium garnet (GGG) substrate magnetized by an external magnetic field creates (at low temperatures) an inhomogeneous demagnetizing field which, besides influencing the MSW dispersion ((manifested by a shift and broadening of the curve), leads to an additional broadening and displacement of the EPR line in ruby. At the same time, a strong paramagnetic absorption in the GGG substrate [3] accounts for a sharp growth in the MSW losses with decreasing temperature (this is illustrated by the comparison of curves *1* and *2* in Fig. 2), thus hindering the development of inversion in the spin system of ruby. For this reason, the operation of a pumping generator did not significantly change the observed behavior.

In connection with this, we conducted an analogous experiment in a structure composed of 200-μm-thick single crystal plates of YIG and ruby with lateral dimensions 16 × 20 mm. The results of this test are presented in Fig. 3. After switching on the pumping generator in this system, we observed the quantum amplification of the FBMSWs at 4.2 and 1.6 K. The amplification coefficient was determined relative to the MSW signal level without pumping. Note that the maximum calculated amplification coefficient under these conditions amounts to 15 and 31 dB, respectively, at an amplification bandwidth of 60–70 MHz. This last value coincides with the EPR line width in ruby, but is greater than the line width of conventional traveling-wave maser [5]. A somewhat greater amplification bandwidth observed in our case is explained by a certain inhomogeneity of the static magnetic field related to demagnetizing fields of relatively thick YIG plates.

Thus, we have experimentally demonstrated the basic possibility of the phenomenon of quantum amplification of microwaves in a YIG–maser crystal system. An integral traveling-wave maser employing this effect can be developed based on an YIG–diamagnetic garnet structure [1]. In this structure, the YIG film plays the role of a retarding structure, while the diamagnetic garnet substrate serves as the active medium (for the purpose of which the latter crystal has to be doped with active paramagnetic centers capable of providing for the maser effect).

REFERENCES

1. M. G. Balinskiĭ, V. V. Danilov, and A. Yu. Nechiporuk, Zh. Tekh. Fiz. **63** (9), 122 (1993) [Tech. Phys. **38**, 798 (1993)].
2. A. E. Siegmann, *Microwave Solid-State Masers* (McGraw-Hill, New York, 1964; Mir, Moscow, 1966).
3. V. V. Danilov, D. L. Lyfar’, Yu. V. Lyubon’ko, *et al.*, Izv. Vyssh. Uchebn. Zaved., Fiz. **32** (4), 48 (1989).
4. M. Marysko, J. Magn. Magn. Mater. **101** (1), 159 (1991).
5. N. T. Cherpak, Izv. Vyssh. Uchebn. Zaved., Radiofiz. **27** (7), 815 (1984).

Translated by P. Pozdeev

Technical Physics Letters, Vol. 28, No. 5, 2002, pp. 371–373. Translated from Pis'ma v Zhurnal Tekhnicheskoĭ Fiziki, Vol. 28, No. 9, 2002, pp. 36–41.
Original Russian Text Copyright © 2002 by Dmitriev, Kassian, Khilinsky.

Chaotic Synchronization of Henon Mappings: The Information Approach

A. S. Dmitriev, G. A. Kassian, and A. D. Khilinsky
Institute of Radio Engineering and Electronics, Russian Academy of Sciences, Moscow, Russia

Received November 12, 2001

Abstract—A new scheme of chaotic synchronization, whereby information concerning the state of a guiding system is transferred to the guided system without using a formalism of the symbolic dynamics, is proposed. It is shown that the volume of transferred data necessary for synchronization of the guided system in the proposed scheme is close to a theoretical minimum. *© 2002 MAIK “Nauka/Interperiodica”.*

The phenomenon of chaotic synchronization [1–3] is characterized by a high sensitivity with respect to noise and other perturbations of transmitted signals [4–7]. Is this a basic feature of the phenomenon or a behavior depending on a particular synchronization scheme that can be suppressed by modifying the scheme? Previously [8, 9], we demonstrated that the reason for this sensitivity is related to information on the current state of a guiding system, which is carried by the chaotic oscillations and has to be transferred without distortions to the guided system. We also proposed a new approach to the synchronization of chaotic systems, according to which only information about a chaotic signal sufficient for restoring this signal is transferred (rather than the signal proper) from the guiding to guided system. Recently [10], this approach was generalized to the case of unidirectional synchronization of two hyperbolic Losy mappings. The information was transferred (by analogy with the one-dimensional case) in the form of a symbolic sequence corresponding to the guiding chaotic sequence.

However, the approach based on the transfer of information by a symbolic sequence, followed by restoration of the initial chaotic sequence from these data, is inapplicable in the case of nonhyperbolic transformations such as Henon mappings. In order to elucidate the reasons for this and develop an alternative procedure, let us consider operation of the scheme restoring a chaotic signal from the corresponding symbolic sequence in the case of the Losy mapping:

$$\begin{cases} x_{n+1} = (\alpha - 1) - \alpha|x_n| + y_n, \\ y_{n+1} = \beta x_n. \end{cases} \quad (1)$$

The Jacobian of mapping (1) is constant and equal to β. this implies that the area of a small cell will decrease by a factor of 1/β in each iteration step. However, the cell contracts in one direction and expands in the other direction. The distance between two close points exponentially increases at a rate of λ_1 in the direction of expansion. In the case of inverse iteration, the directions of expansion and contraction reverse. As a result, the rate of expansion of the trajectories becomes $|\lambda_2|$, where λ_2 is the Lyapunov index of minimum rank.

A symbolic dynamics for the Losy mapping, constructed according to the rule $X_n = \mathrm{sgn}(x_n)$ [11], represents a binary sequence. The chaotic sequence x_n is restored from the symbolic sequence X_n by the following procedure. The two-dimensional (2D) Losy mapping is represented by a single iterative equation of the second order:

$$|x_n| = \frac{\alpha - 1}{\alpha} - \frac{1}{\alpha}x_{n+1} + \frac{\beta}{\alpha}x_{n-1}. \quad (2)$$

Note that Eq. (2) is compressive with respect to variables x_{n-1}, and x_{n+1} because the corresponding coefficients β/α and 1/α are less than unity. This implies that, for x_{n-1}, and x_{n+1} known to within a certain accuracy, the $|x_n|$ value is calculated using formula (2) at a higher precision. The sign of x_n is determined by that of the corresponding X_n value.

Let there be an initial estimate for N terms in the x_n sequence: $x_1^{(0)}, \ldots, x_N^{(0)}$. Upon multiple repetition of the procedure of estimating the nth term of the sequence using the $(n - 1)$th and $(n + 1)$th neighbors, we obtain a gradually improved sequence of estimates for x_n. The initial approximation is provided by the symbolic sequence $\{X_n\}$. The restoration proceeds according to the iterative process

$$x_n^i = X_n|x_n^i| = X_n\left[\frac{\alpha - 1}{\alpha} - \frac{1}{\alpha}x_{n+1}^{i-1} + \frac{\beta}{\alpha}x_{n-1}^{i-1}\right], \quad (3)$$

where i is the iteration step number.

Figure 1 (curve *1*) shows a plot of the quality of restoration versus the number of elements for a chaotic sequence of length N. As can be seen from this plot, the

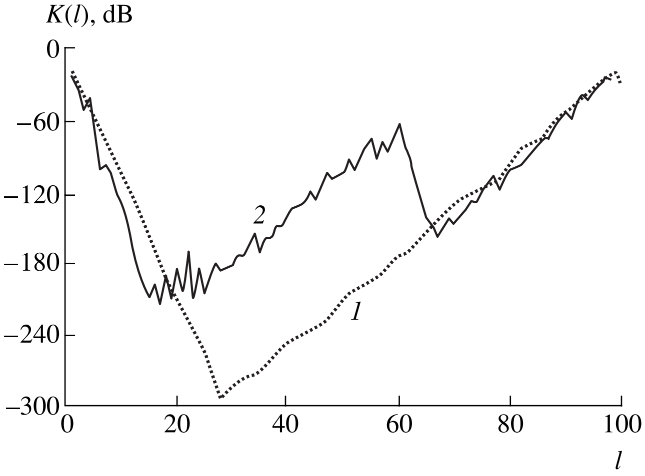

Fig. 1. A plot of the restoration error $K(l)$ versus point number l for a chaotic sequence restored by a symbolic binary sequence of 100 elements using an algorithm proposed for the (*1*) Losy and (*2*) Henon mappings.

quality of restoration at the sequence ends (1 and N) is not improved because these points have no left or right neighbors, respectively. The best quality of restoration is observed for the points with numbers $\approx N/3$. The slopes of the triangle sides are determined by the λ_1 and λ_2 values. Note that, if the initial and final points in the sequence are known with an accuracy of ε (rather than represent elements of a binary sequence as was assumed above), the proposed algorithm allows the entire chaotic trajectory to be restored with an accuracy of about ε.

The Henon mapping

$$\begin{cases} x_{n+1} = 1 - \alpha x_n^2 + y_n, \\ y_{n+1} = \beta x_n \end{cases} \quad \alpha \in [1, 2], \quad \beta \in [0, 1] \quad (4)$$

is a nonhyperbolic transformation. As noted above, the construction of a symbolic dynamics for this mapping is hindered [12] and the approach developed for the Losy mapping is directly inapplicable. However, an attempt at using this approach may help in understanding the reasons of unsatisfactory results and in developing an adequate synchronization algorithm.

Let, similar to the above case of the Losy mapping, a sequence of $X_n = \mathrm{sgn}(x_n)$ to be transferred. Let us write the two-dimensional Henon mapping in the form of a one-dimensional second-order mapping:

$$x_n = \frac{1}{\sqrt{\alpha}}\sqrt{1 - x_{n+1} + \beta x_{n-1}}. \quad (5)$$

Note that the mapping (5) contracts everywhere except for a region of small x_n, $|x_n| < \varepsilon$ ($\varepsilon \sim 0.2$). Outside the latter region, the error of x_n calculated by Eq. (5) is smaller than errors at the points x_{n-1} and x_{n+1} by which the x_n value is estimated. For small $|x_n|$, this statement is generally not valid. For this reason, restoration of a chaotic sequence using an algorithm analogous to that employed above for the Losy mapping cannot provide for a sufficiently high quality of the result. A typical result of using this algorithm is illustrated by curve *2* in Fig. 1. As can be seen, there are regions where the initial signal is restored with a significantly impaired quality; on the other hand, the quality of restoration in some other time intervals is sufficiently high. A decrease in the quality is caused by the lack of contraction in mapping (5) at small $|x_n|$.

Let estimates of the signal values at the time instants n_0 and $n_0 + 1$ at the guided system input be known with a required precision and let a copy of the Henon mapping be available at this input as well. Then we can obtain the values of the binary sequence elements X_n for several points with $n > n_0$ (following the point n_0), proceeding from the x_{n_0} and x_{n_0-1} values. For this purpose, it is sufficient to construct a "forecast" by iteration of the Henon mapping with the initial condition (x_{n_0}, x_{n_0-1}). In the general case, these conditions are known with a finite precision and may slightly differ from the values at the output of the guiding system. For this reason, a correct binary sequence can be obtained only for a sufficiently short part of the trajectory, in which the error of the above forecast is smaller than the characteristic size of the attractor. In addition, the forecast allows us to determine the time instants at which the system trajectory passes through points with small absolute values of the signal.

As was noted above for the algorithm of restoration of the Losy mapping, a chaotic sequence on the time interval from 1 to N can be restored with high accuracy if the x_1 and x_N values are known with the required precision and the binary sequence X_n is known on the interval $n \in [2, N]$. The same is valid for application of this algorithm to the Henon mapping, provided that no points with small absolute values of x_n are present in the interval $n \in [2, N]$.

Thus, we arrive at the following algorithm of the information transfer from the guiding to guided system and of the chaotic sequence restoration. Let ν_i be the numbers of points at which the trajectory most closely approaches zero, and let $\mu_i = [\nu_i, \nu_{i+1}]$ be a region of the trajectory bounded by two adjacent points of this type (Fig. 2). Assuming that an estimate of the chaotic sequence in the μ_i region of the trajectory is available at the input of the guided system, we can take two end points from μ_i as the initial conditions and construct a forecast for the points within μ_{i+1} (the length of μ_{i+1} is unknown). Since the initial conditions for the predicted trajectory are known to within a certain error, while the perturbed and unperturbed trajectories expand on the average exponentially, the accuracy of the forecast will decrease with the distance from ν_i.

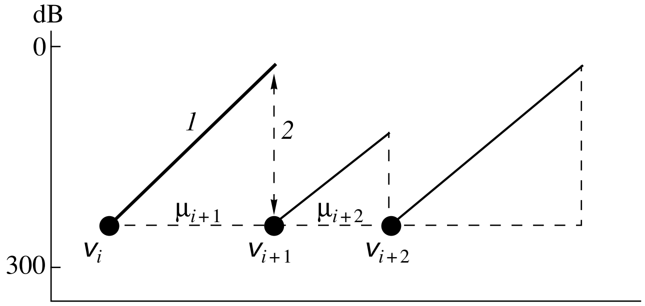

Fig. 2. A schematic diagram illustrating (*1*) a forecast of the chaotic trajectory and (*2*) the volume of transferred information necessary for the signal restoration.

However, provided that the number of points between v_i and v_{i+1} is not very large, we can (i) predict the number v_{i+1} of a point at which the absolute value of the variable is close to zero and (ii) determine the binary sequence X_n for all points from μ_{i+1}. Then, only the value of the variable at the point v_{i+1} has to be determined for completely restoring the chaotic sequence. This value is transferred via the channel at the required velocity. After that, the region μ_{i+1} is restored using the algorithm described previously for the Losy mapping.

Thus, in order to restore a chaotic sequence on the region μ_{i+1}, it is sufficient to transfer the value of the variable at single point (with the number v_{i+1}). Using a slightly modified algorithm, it is possible to reduce the amount of transferred information. Indeed, note that, predicting the values of the variable at the points from μ_{i+1}, we simultaneously obtain a forecast for the v_{i+1} point as well. Therefore, there is no need to transfer all the values of $x_{v_{i+1}}$: we have only to refine the predicted value, that is, to transfer the bits distorted as a result of the exponential expansion of perturbed and unperturbed trajectories.

A numerical realization of the proposed algorithm provides for a high quality of synchronization at a volume of the transferred data ~0.8 bit/reading, which is sufficiently close to the level of information production by the Henon mapping, which is about 0.6 bit/reading.

REFERENCES

1. H. Fujisaka and T. Yamada, Prog. Theor. Phys. **69** (1), 32 (1983).
2. V. Afraĭmovich, N. Verichev, and M. Rabinovich, Izv. Vyssh. Uchebn. Zaved., Radiofiz. **29** (9), 1050 (1986).
3. L. M. Pecora and T. L. Caroll, Phys. Rev. Lett. **64** (8), 821 (1990).
4. Yu. L. Bel'skiĭ and A. S. Dmitriev, Radiotekh. Élektron. (Moscow) **40** (2), 265 (1995).
5. M. Hasler and Yu. L. Maistrenko, IEEE Trans. Circuits Syst., I: Fundam. Theory Appl. **44** (10), 856 (1997).
6. M. N. Lorenzo, M. P. Kennedy, G. Kolumban, and G. Kis, in *Proceedings of the Workshop on Nonlinear Dynamics of Electronic Systems, NDES'98, Budapest, 1998*, p. 249.
7. G. A. Johnson, D. J. Mar, T. L. Caroll, and L. M. Pecora, Phys. Rev. Lett. **80** (18), 3956 (1998).
8. A. S. Dmitriev, Izv. Vyssh. Uchebn. Zaved., Radiofiz. **41** (12), 1497 (1998).
9. A. S. Dmitriev, G. A. Kassian, and A. D. Khilinsky, Int. J. Bifurcation Chaos Appl. Sci. Eng. **10** (4), 749 (2000).
10. A. S. Dmitriev, G. A. Kassian, M. Hasler, and A. D. Khilinsky, Radiotekh. Élektron. (Moscow) **46** (5), 566 (2001).
11. Wei-Mou Zheng, Chaos, Solitons and Fractals **1** (3), 243 (1991).
12. H. Zhao and W.-M. Zheng, Commun. Theor. Phys. **19** (1), 21 (1993).

Translated by P. Pozdeev

Technical Physics Letters, Vol. 28, No. 5, 2002, pp. 374–376. Translated from Pis'ma v Zhurnal Tekhnicheskoĭ Fiziki, Vol. 28, No. 9, 2002, pp. 42–47.
Original Russian Text Copyright © 2002 by Gashinova, I. Kolmakov, Ya. Kolmakov, Vendik.

Modeling the Passive Microwave Devices Based on Planar Multilayer Anisotropic Structures with High-Temperature Superconductors

M. S. Gashinova, I. A. Kolmakov, Ya. A. Kolmakov, and I. B. Vendik
St. Petersburg State Electrotechnical University, St. Petersburg, Russia
e-mail: MWLab@eltech.ru

Received November 14, 2001

Abstract—The electrodynamic properties of an arbitrary multilayer medium, including anisotropic layers and conductors of an arbitrary shape on one of the interfaces, are studied. The conductors represent thin layers of a high-temperature superconductor (HTSC). A system of integral equations for the electric field is solved in the spatial domain. The electrodynamic problem was solved by numerical methods to determine the surface current density by applying the Galerkin procedure and by solving the main matrix equation relative to coefficients of the current density expansion in a basis set of finite functions. The losses in HTSC layers are taken into account by using the concept of the equivalent surface impedance and the Leontovich boundary conditions. The anisotropy is taken into account in determining the Green dyad for a structure with an arbitrary number of anisotropic or isotropic layers. Correctness of the proposed model is confirmed by the results of calculations of the surface current density distribution. *© 2002 MAIK "Nauka/Interperiodica".*

Introduction. The electric properties of high-temperature superconductors (HTSCs) allow these materials to be used in miniature super-narrowband filters and related devices. The most important aspect in designing such devices is the requirement of high accuracy in the calculations of current distribution in the structure, which can be provided by using an adequate electrodynamic model taking into account the particular HTSC parameters and the anisotropy of layers. An allowance for the anisotropy is important, for example, for HTSC films grown on single crystal sapphire substrates.

The analysis of topologically involved multilayer structures reveals advantages of a three-dimensional (3D) analysis over the 2D case. The 3D approach allows us to more readily solve the problems related to taking into account discontinuities in the structures studied.

Formulation of the problem and analysis of the model. Planar structures are conventionally modeled by solving integral equations relating the electric field and electric currents in the plane of signal electrodes to a Green dyad as the kernel of an integral operator [1]. The problem is rendered discrete by introducing a spatial grid in the plane containing conductors and by using a basis set of finite functions for expanding the current density on this grid. The integral operator is reduced to a discrete representation in the form of double series in grid cell indices.

The modeled structure represents a multilayer medium bounded by electric walls, which contains a conductor of an arbitrary shape on one of the interfaces. All interfaces are parallel to the XY coordinate plane. The conductor is divided into two regions: Ω, in which the current density distribution has to be determined, and Q, in which a constant surface density of the excitation current J_{imp} is preset (the excitation region Q overlaps with Ω).

The tangential electric field $\mathbf{E}_t(x, y)$ in the conductor plane can be expressed in terms of the surface current density $\mathbf{J}_t(x, y)$ by an equation

$$j\omega\varepsilon_0\mathbf{E}_t = \iint_{\Omega}\mathbf{G}_E(x, y, x', y')\mathbf{J}_t(x', y')dy'dx', \qquad (1)$$

where

$$\mathbf{E}_t = \begin{pmatrix} E_x \\ E_y \end{pmatrix}, \quad \mathbf{J}_t = \begin{pmatrix} J_x \\ J_y \end{pmatrix}, \quad \mathbf{G}_E = \begin{pmatrix} G_{xx} & G_{xy} \\ G_{yx} & G_{yy} \end{pmatrix}$$

is the Green dyad representing a kernel of the integral operator of a vector equation, ω is the circular frequency, and ε_0 is the permittivity of a vacuum.

Once the spatial grid at the conductor interface is introduced, we can define a basis set of finite functions, representing the products of triangular and rectangular pulses, for expanding the surface current density; the basis set functions differ by a translational shift with respect to the spatial coordinate.

In order to derive expressions for the Green dyad components in the spectral domain, each dielectric layer is described by the corresponding Maxwell equations and characterized by a 6 × 6 tensor composed of

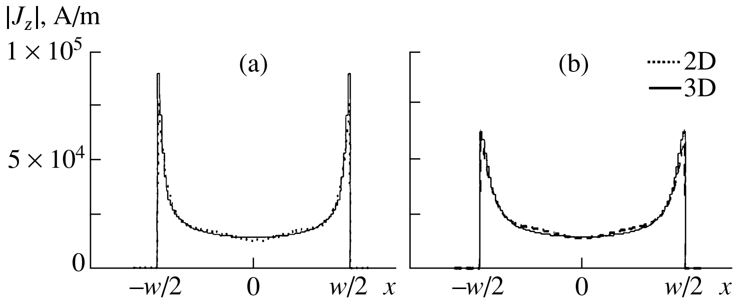

Fig. 1. Longitudinal current distribution in the cross section of a microstrip line (w = 45 μm) calculated for a frequency of 1 GHz and two different temperatures: T = 30 K (a) and 77 K (b). For comparison, we also present the results of calculations based on a 2D model for the same microstrip transmission line [5]. Substrate parameters: thickness h = 0.5 mm, ε = 23.7; YBCO film parameters: thickness t = 0.45 μm, $\lambda_L(0)$ = 0.22 μm, $\sigma_n(T_c) = 2.4 \times 10^6\ (\Omega\ \mathrm{m})^{-1}$, γ = 1.5, α = 10, T_c = 87 K.

the magnetic permeability and dielectric permittivity tensors [2]. This description allows the anisotropy of layers to be taken into account (in contrast to a method based on determining Green's functions as combinations of the input wave impedances of the TE and TM (in Z-direction) waves [3]).

For a shielded structure under consideration, the kernel of the integral operator can be represented as a discrete 2D Fourier transform of the spectral Green function. In order to provide for computational efficiency, the series should be represented by the corresponding partial sums with the upper summation limits determined by a preset estimate of the residual term of the expansion.

The equation relating tangential components of the electric fields of the incident, scattered, and transmitted waves is as follows:

$$\mathbf{E}_{\mathrm{inc}} + \mathbf{E}_{\mathrm{scat}} = \mathbf{E}_{\mathrm{tran}} \longleftrightarrow \iint\limits_{D} (\mathbf{G}J_{\mathrm{imp}} + \mathbf{G}J_t)dS = Z_s J_t, \quad (2)$$

where D is a rectangular cross section of the structure in the XY plane and Z_s is the equivalent surface impedance of the HTSC film. A nonzero term in the right-hand part of Eq. (1) allows the losses to be taken into account in the case of a lossy conductor.

Representing the unknown current density as an expansion over the introduced basis set functions and expressing the source current density in terms of this basis set (with the aid of a Galerkin test procedure for a solution to Eq. (2)), we obtain a system of linear equations relative to the expansion coefficients. The surface impedance Z_s of a thin HTSC film in Eq. (2) can be determined using a phenomenological HTSC model [4]. In order to represent the system of equations in the form of a matrix equation, it is necessary to form an array of the matrix elements; an allowance of the structure symmetry significantly simplifies solution of the resulting determinant equation.

The scattering parameters are elements of the S matrix, which are determined by calculating complex amplitudes of the incident and reflected waves in the selected reference planes [1]. The elements of the scattering matrix S are determined using the following assumptions: (i) each excitation line segment in a device containing n inputs has a sufficiently large length and maintains a single fundamental mode; (ii) the propagation constant β along a line segment is determined from a 2D electrodynamic analysis of the transmission line [5]. For a device containing n inputs, we consider n linearly independent excitation states.

It is physically reasonable to consider an excitation model describing a real current distribution in the cross section of the line under assumption that a fundamental mode is propagating in the feed microstrip line. According to this, a longitudinal current in the line is approximated by the so-called Maxwell weight representing a function of the type $[1 - (2x/w)^2]^{-1/2}$, where w is the line width.

Results and discussion. Figure 1 shows the longitudinal current distribution in the cross section of a microstrip line employing an YBCO film at two temperatures for an excitation current of I = 1 A. For comparison, we also present the results of calculations based on a 2D model of the transmission line [5]. A good agreement of the results of 2D and 3D modeling is qualitatively confirmed by the experimental data for the surface current density distribution in an HTSC structure, obtained from the photoresponse measurements [6], and by the results of theoretical calculations in the quasistatic approximation [7]. The buildup of the current density at the edge of the microstrip reflects an increase in the depth of the magnetic field penetration with increasing temperature. This behavior is consistent with the physical essence of the phenomenon and agrees with the HTSC model proposed in [4].

For calculating the passive HTSC structures, a special program was developed based on the proposed model. Using this program, we have simulated the surface current density distribution in a three-pole filter based on coupled microstrip lines excited by a T-junction (see the inset to Fig. 2a). Figure 2 shows the results of calculations of the current density distribution at two

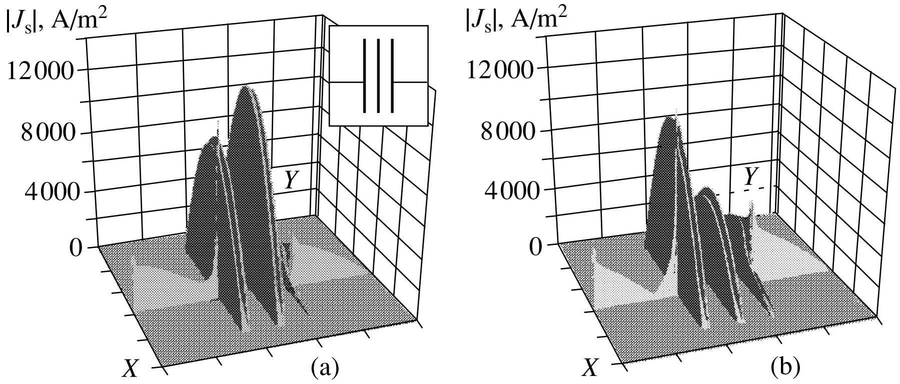

Fig. 2. The surface current density distribution in a three-pole filter at $T = 70$ K calculated for two frequencies within the transmission band: (a) $f_1 = 3.09$ GHz; (b) $f_2 = 3.14$ GHz. Microstrip line parameters: width, 0.5 mm; resonator length, 12 mm; lateral dimensions, $D = 16 \times 16$ mm. The parameters of the substrate and YBCO film are the same as in Fig. 1.

frequencies within the transmission band for an excitation current of $I = 1$ A.

Acknowledgments. This study was performed by contract with the Ministry of Science and Technology of the Russian Federation (no. 107-4(00)-P).

REFERENCES

1. W. Wertgen and R. N. Jansen, Int. J. Numer. Model. **2**, 152 (1989).
2. A. A. Mostafa, C. M. Krowne, and K. A. Zaki, IEEE Trans. Microwave Theory Tech. **35** (12), 1399 (1987).
3. T. Itoh, IEEE Trans. Microwave Theory Tech. **28**, 733 (1980).
4. I. B. Vendik, Supercond. Sci. Technol. **13**, 974 (2000).
5. I. B. Vendik, O. G. Vendik, A. N. Deleniv, *et al.*, IEEE Trans. Microwave Theory Tech. **48**, 1247 (2000).
6. J. C. Culbertson, H. S. Newman, and C. Wilker, J. Appl. Phys. **84** (3), 2768 (1998).
7. D. M. Sheen, S. M. Ali, D. E. Oates, *et al.*, IEEE Trans. Appl. Supercond. **1** (2), 108 (1991).

Translated by P. Pozdeev

Technical Physics Letters, Vol. 28, No. 5, 2002, pp. 377–381. Translated from Pis'ma v Zhurnal Tekhnicheskoĭ Fiziki, Vol. 28, No. 9, 2002, pp. 48–57.

The Effect of Mechanical Loading on the Photoacoustic Response from Radial Cracks in Vickers-Indented Al_2O_3–SiC–TiC Ceramics

K. L. Muratikov, A. L. Glazov, D. N. Rose, and D. E. Dumar

Ioffe Physicotechnical Institute, Russian Academy of Sciences, St. Petersburg, 194021 Russia

Received November 29, 2001

Abstract—The Vickers indentation zones in Al_2O_3–SiC–TiC ceramics were studied by scanning laser photoacoustic microscopy. It is shown that the method of photoacoustic microscopy with a piezoelectric detector is sensitive to external mechanical stresses. Variation of the photoacoustic response signal under the action of normal and tangent stresses in the vicinity of radial cracks was determined. The photoacoustic data can be used to estimate the stress intensity coefficients at the crack end. © *2002 MAIK "Nauka/Interperiodica".*

In recent years, photoacoustic and photothermal microscopy techniques are being successfully employed for the diagnostics of defects in the bulk and surface layers of various materials and structures [1]. It would be also of interest to employ the photoacoustic method for measuring internal stresses: a number of investigations have been reported up to now, showing good prospects in this respect [2–12]. Most of these papers reported on the significant features in behavior of the photoacoustic response near the ends of cracks in brittle materials. At the same time, almost no attention has been paid to the character of the photoacoustic signal variation in the regions with internal stresses immediately upon application of a preset external load. Investigations of such effects would significantly increase our knowledge of mechanisms of the stress effect upon the photoacoustic response and stimulate the development of new methods for measuring the mechanical parameters characterizing internal stresses in the vicinity of cracks.

In this context, we have studied the behavior of the photoacoustic response from solid samples immediately in the course of application of external mechanical stresses. The main attention was devoted to the case when applied stresses were directed along the sample surface. Investigation was performed on the samples of an Al_2O_3–SiC–TiC ceramics with Vickers indentations. An important advantage of this approach is that the structure of cracks, residual stresses, and plastic strain zones in the vicinity of Vickers indentations are known and well reproduced [13]. Previously [11, 12], we have thoroughly analyzed the behavior of the photoacoustic signal in the vicinity of indentation sites in the same ceramics and studied the effect of annealing on this behavior. Therefore, it was possible to compare features of the photoacoustic signals from samples for various external stresses and different mutual arrangement of the source of applied stress and the indentation site.

The experiments were performed on samples of Al_2O_3–SiC–TiC ceramics (Crystalloy 2311 EDX) prepared by hot pressing from a mixture of powdered Al_2O_3 (46.1 vol %), powdered TiC (23.0 vol %), and needle-like SiC crystals (30.9 vol %). The hot pressing was carried out in an inert gas atmosphere at a temperature of 1700–1800°C. The final ceramic samples had a density of 3.915 g/cm^3, which amounted to 99% of the theoretical limit calculated using the densities of the components. The average TiC grain size was about 5 μm, and the average grain size of the Al_2O_3 matrix was 0.3–1.0 μm. The needle-like SiC crystals reinforcing the ceramic composition had an average length of 25 μm and a diameter of about 0.5 μm.

The residual stress fields in the ceramics were generated by indenting the samples according to Vickers under a load of 98 N, using different orientations of the indentor relative to the sample surface. As a result, it was possible to select the indented regions containing radial cracks with various orientations relative to the direction of applied stress. The image of a selected indentation area was obtained by scanning the sample surface in two coordinates at a step of 2.5 μm. The temperature waves and acoustic oscillations were excited by the radiation of an Ar laser (LGN-503 type) modulated by an acoustooptical modulator (ML-210 type). In each experiment, the first photoacoustic image of a given Vickers-indented region of Al_2O_3–SiC–TiC ceramics was obtained in the absence of external stresses. Then the same area of the sample was imaged upon application of a preset mechanical load. Thus, it was possible to detect the stress-induced changes in the photoacoustic response from various regions in the vicinity of Vickers indentations.

Figure 1 shows photoacoustic images typical of the given ceramics, showing the character of changes induced by application of the additional external stress.

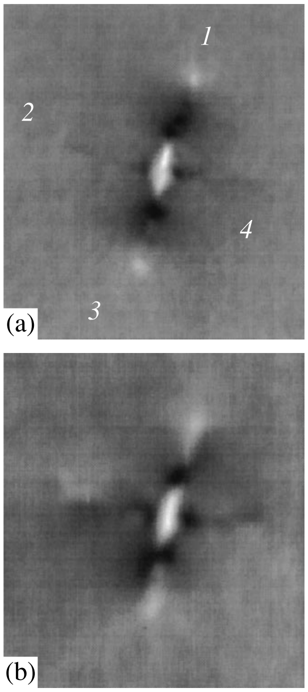

Fig. 1. Scanning photoacoustic microscopy images of the surface of Al_2O_3–SiC–TiC ceramics indented according to Vickers (imaged area size, 450 × 500 μm; excitation laser radiation modulated at 142 kHz): (a) a sample in the free (unloaded) state (numbers indicate radial cracks); (b) the same sample under compressive load of 170 MPa directed left to right in the plane of the image.

As can be seen, changes take place in various parts of the image, including regions at the ends of radial cracks, in the zone of plastic strain, and in the zone of subsurface side cracks. In this study, we concentrated on the behavior of photoacoustic signals in the region at the end of a radial crack. Outside of these regions, the structure of the plastic strain zones and cracks is more complicated and requires additional characterization. As can be seen from Fig. 1, the external stress produced different effects on the behavior of photoacoustic signals from regions at the ends of radial cracks oriented at different angles relative to the direction of applied stress.

In order to explain the experimental data, we will use our theoretical results obtained previously, concerning the nature of the photoacoustic effect in solids with internal stresses, and the data known from the mechanics of strained solids about the behavior of internal stresses at the crack end. It is necessary to emphasize that the photoacoustic images observed in our experiments are formed in a relatively thin surface layer of the samples. In particular, the depth of the thermal wave penetration into the Al_2O_3–SiC–TiC ceramics studied at a modulation frequency of 100 kHz is about 10 μm. In addition, it should be taken into account that internal stresses at the end of a radial crack are directed predominantly along the sample surface. For this reason, below we assume that the strain tensor related to the internal stresses at the crack ends in the region of the photoacoustic signal formation obeys the conditions $U_{xx}, U_{yy} \gg U_{zz}$ (the z axis is directed along the normal to the surface). As was demonstrated in [14, 15], a photoacoustic signal related to the internal stresses in this case can be presented in a linear approximation with respect to U_{xx} and U_{yy}:

$$\Delta V(\omega) = A(U_{xx} + U_{yy}). \tag{1}$$

Here, $A = V_0(\omega)(\beta_0 + 3/2 - 2l')$, $V_0(\omega)$ is the photoacoustic piezoelectric signal from the object measured in the absence of initial strain, $l' = \frac{l}{\rho_0 c_l^2}$, l is the Mournagan constant, ρ_0 is the density of the sample in the initial state, c_l is the longitudinal sound velocity, and β_0 is a coefficient determining dependence of the thermoelastic energy on the initial deformation [14, 15].

The zones of plastic strain are localized immediately at the ends of radial cracks. The zones of internal stress distribution occupy much greater regions, extending beyond the plastic strain zones. In these regions, the residual deformations exhibit an elastic character and can be considered as related to the internal stresses by the Hooke law. Then, according to Eq. (1), the photoacoustic signal must be related to the internal stresses as

$$\Delta V(\omega) = A'(\sigma_{xx} + \sigma_{yy}), \tag{2}$$

where $A' = \frac{1-\nu}{E}A$, ν is the Poisson coefficient, E is the elastic modulus, and σ_{xx} and σ_{yy} are the strain tensor components. Relationship (2) indicates that dependence of the photoacoustic signal on the internal stresses is determined by the same parameters as those involved in the so-called stress pattern analysis by measurement of thermal emission (SPATE). According to [16], the signal measured in the case of SPATE is also proportional to the sum $\sigma_{xx} + \sigma_{yy}$. However, the spatial resolution of SPATE is on the order of millimeters, while our photoacoustic technique is capable of providing for a micron resolution.

As noted above, the photoacoustic signal is formed within a thin surface layer of the sample. Therefore, the internal stresses at the ends of radial cracks near the sample surface can be determined considering these cracks as flat. Then, using expressions for the stress tensor components σ_{xx} and σ_{yy} in the case of flat cracks [17], the photoacoustic signal (2) at the end of the crack can be expressed as

$$\begin{aligned}&\Delta V(\omega)\\ &= A'\frac{2}{\sqrt{2\pi r}}\left[(K_I^{(0)} + K_I)\cos\frac{\theta}{2} - (K_{II}^{(0)} + K_{II})\sin\frac{\theta}{2}\right],\end{aligned} \tag{3}$$

where K_I and K_{II} are the coefficients of stress intensity relative to the applied load components normal and tangent to the crack sides; $K_I^{(0)}$ and $K_{II}^{(0)}$ are the stress intensity coefficients relative to the internal stresses; r is the distance from the crack vertex to the point of observation; and θ is the angle between the crack axis and the direction to the point of observation.

The stress intensity coefficients for a crack in the region affected by external stresses are determined by the magnitude and direction of the applied load. In the case of a flat crack, this relation is described by the formulas [17]

$$K_I = K_I^{(1)}\sin^2\phi, \quad K_{II} = K_{II}^{(1)}\sin\phi\cos\phi, \tag{4}$$

where ϕ is the angle between the crack axis and the direction of loading; $K_I^{(1)}$ and $K_{II}^{(1)}$ are the stress intensity coefficients, which characterize the crack and are independent of the angle ϕ.

Using formulas (3) and (4), we obtain the following expression for the photoacoustic piezoelectric response in the region of the crack end:

$$\Delta V(\omega) = A'\frac{2}{\sqrt{2\pi r}}\Big[(K_I^{(0)} + K_I^{(1)}\sin^2\phi)\cos\frac{\theta}{2} - (K_{II}^{(0)} + K_{II}^{(1)}\sin\phi\cos\phi)\sin\frac{\theta}{2}\Big]. \tag{5}$$

In order to check for the proposed model of the photoacoustic signal formation in the vicinity of radial cracks, we have compared theoretical expression (5) to the experimental data obtained from the photoacoustic images of Vickers indentation sites in Al_2O_3–SiC–TiC ceramics. For this purpose, we analyzed variation of the photoacoustic signal near the crack end in the direction perpendicular to the crack axis. This direction was selected because the distributions of normal and tangent stresses in this case must be significantly different. The photoacoustic signal intensity profiles were measured for the radial cracks oriented at various angles relative to the direction of loading, which allowed us to compare the theoretical and experimental results for cracks under variable loading conditions.

Figure 2 presents the experimental results reflecting variation of the photoacoustic signal in the indicated direction for two cracks in comparison to the theoretical curves calculated using relationship (5). The cracks were selected so as to provide for a significantly different character of the effect of external stresses. Indeed, crack 1 was oriented at $\phi \cong 75°$ and, hence, the external stress was almost perpendicular to the sides crack. For crack 4, the relative orientation angle was $\phi \cong 17°$ and the additional stresses caused by external load were mostly tangent. The theoretical calculations for cracks 1 and 4 were performed using the distance l from the crack vertex to the line of photoacoustic measurements equal to 5 and 20 μm, respectively. The data in Fig. 2 show that the observed character of variation of the photoacoustic signal near the end of the radial crack qualitatively agrees with the theoretical description in both cases.

Our experimental data on the photoacoustic signal variation in the vicinity of the crack end, together with the results known from the theory of cracking, lead to certain conclusions concerning the stress intensity coefficients for cracks in the Al_2O_3–SiC–TiC ceramics studied. According to the theory of cracks [18], the initial stress intensity coefficient for a crack formed at an indentor load P in the general case can be expressed as $K_I^{(0)} = \chi\frac{P}{L^{3/2}}$, where χ is a dimensionless coefficient determined by the crack shape and L is the crack length. By the same token, the stress intensity coefficient relative to an external lad applied at $\phi = 90°$ is $K_I^{(1)} = \psi\sqrt{L}\,\sigma$, where ψ is a different dimensionless coefficient determined by the crack shape.

The experimental data presented in Fig. 2 indicate that compensation of the internal stresses near the end of radial crack 1 must take place at an external compressive stress of about 340 MPa. The length of radial cracks in the Al_2O_3–SiC–TiC ceramics studied at an indentor load of 98 N was about 150 μm. Using these data, we can obtain an approximate relationship between the coefficients χ and ψ: $\chi \cong 0.075\psi$. Note that this estimate quantitatively agrees with an analogous result reported for a ceramic material with Al_2O_3 grains [19]. In addition, our experimental data indicate that $K_I^{(1)} \approx K_{II}^{(1)}$. This result is consistent with the theory of straight cracks in thick plates [17], according to which the two quantities must be equal. In principle, the proposed approach based on the photoacoustic method allows the absolute values of the stress intensity coefficients to be estimated as well. For this purpose, it is necessary, in addition to analysis of the images of the Vickers indentation zones, to study dependence of the photoacoustic signal on the external load for homogeneous regions of the sample. Within the framework of this study, we measured only relative changes of the photoacoustic signal. A subsequent investigation will include the proposed analysis.

Thus, the photoacoustic piezoelectric response quite adequately reproduces the features of variation of the field of internal stresses in the vicinity of radial cracks under the action of both normal and tangent external stresses. This circumstance allows the photoacoustic microscopy with piezoelectric detection to be employed for studying the distribution of internal stresses near the surface cracks in ceramic materials. The results obtained from the photoacoustic measurements on the samples under external loading conditions

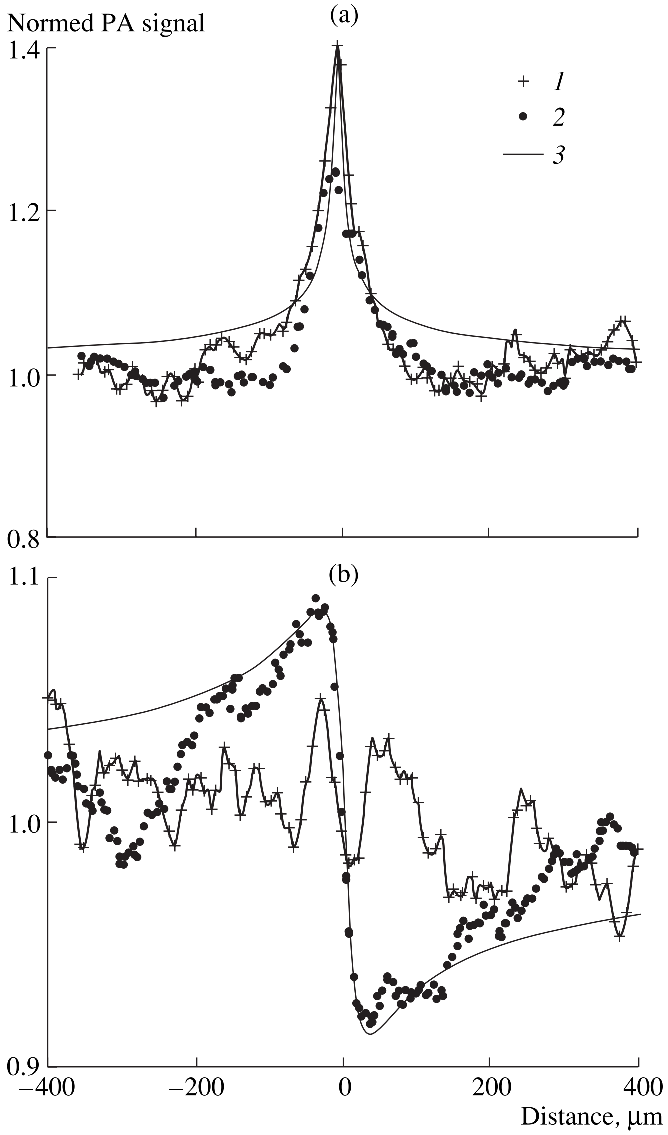

Fig. 2. The photoacoustic signal intensity profiles (normalized to the mean value) measured near the end of radial cracks (a) 1 and (b) 4 (see Fig. 1) along the line perpendicular to the crack axis: (*1*) unloaded sample; (*2*) loaded sample; (*3*) theoretical curve.

can be used for estimating the stress intensity coefficients near crack ends.

Acknowledgments. The work was supported in part by the Russian Foundation for Basic Research (project no. 01-01-00855) and by the US Civilian Research and Development Foundation (grant no. PR1-2366-ST-02).

REFERENCES

1. A. Rosencwaig, in *Progress in Photothermal and Photoacoustic Science and Technology*, Vol. 2: *Non-Destructive Evaluation (NDE)*, Ed. by A. Mandelis (PTR Prentice-Hall, Englewood Cliffs, 1994), pp. 1–23.
2. J. H. Cantrell, M. Qian, M. V. Ravichandran, and K. W. Knowles, Appl. Phys. Lett. **57** (18), 1870 (1990).
3. H. Zhang, S. Gissinger, G. Weides, and U. Netzelmann, J. Phys. IV **4**, C7-603 (1994).
4. R. M. Burbelo and M. K. Zhabitenko, in *Progress in Natural Science* (Taylor and Francis, London, 1996), Suppl. Vol. 6, pp. 720–723.
5. F. Jiang, S. Kojima, B. Zhang, and Q. Yin, Jpn. J. Appl. Phys., Part 1 **37** (5B), 3128 (1998).
6. K. L. Muratikov, A. L. Glazov, D. N. Rose, *et al.*, Pis'ma Zh. Tekh. Fiz. **23** (5), 44 (1997) [Tech. Phys. Lett. **23**, 188 (1997)].
7. K. L. Muratikov, A. L. Glazov, D. N. Rose, and D. E. Dumar, Pis'ma Zh. Tekh. Fiz. **24** (21), 40 (1998) [Tech. Phys. Lett. **24**, 846 (1998)].
8. K. L. Muratikov, A. L. Glazov, D. N. Rose, and J. E. Dumar, in *Proceedings of 10th International Conference "Photoacoustic and Photothermal Phenomena"* (10 ICPPP), AIP Conf. Proc. **463**, 187 (1998).

9. K. L. Muratikov and A. L. Glazov, Zh. Tekh. Fiz. **70** (8), 69 (2000) [Tech. Phys. **45**, 1025 (2000)].
10. K. L. Muratikov, A. L. Glazov, D. N. Rose, and J. E. Dumar, J. Appl. Phys. **88** (5), 2948 (2000).
11. K. L. Muratikov, A. L. Glazov, D. N. Rose, and J. E. Dumar, in *Proceedings of the 4th International Congress on Thermal Stresses, Thermal Stresses'01, Osaka, Japan, 2001*, p. 85.
12. K. L. Muratikov, A. L. Glazov, V. I. Nikolaev, *et al.*, Pis'ma Zh. Tekh. Fiz. **27** (12), 33 (2001) [Tech. Phys. Lett. **27**, 500 (2001)].
13. R. F. Cook and G. M. Pharr, J. Am. Ceram. Soc. **73** (4), 787 (1990).
14. K. L. Muratikov, Pis'ma Zh. Tekh. Fiz. **24** (13), 82 (1998) [Tech. Phys. Lett. **24**, 536 (1998)].
15. K. L. Muratikov, Zh. Tekh. Fiz. **69** (7), 59 (1999) [Tech. Phys. **44**, 792 (1999)].
16. P. Stanley and J. M. Dulieu-Smith, Exp. Tech. **20** (2), 21 (1996).
17. L. M. Sedov, *A Course in Continuum Mechanics* (Nauka, Moscow, 1970; Wolters-Noordhoff, Groningen, 1971–1972).
18. S. M. Smith and R. O. Scattergood, J. Am. Ceram. Soc. **75** (2), 305 (1992).
19. L. M. Braun, S. J. Bennison, and B. R. Lawn, J. Am. Ceram. Soc. **75** (11), 3049 (1992).

Translated by P. Pozdeev

Technical Physics Letters, Vol. 28, No. 5, 2002, pp. 382–384. Translated from Pis'ma v Zhurnal Tekhnicheskoĭ Fiziki, Vol. 28, No. 9, 2002, pp. 58–62.
Original Russian Text Copyright © 2002 by Zelenin, Davydov, Korogodskiĭ, Lebedev.

The Effect of Hydrogen Etching on the Electrical Properties of Autoepitaxial Silicon Carbide Layers

V. V. Zelenin, D. V. Davydov, M. L. Korogodskiĭ, and A. A. Lebedev
Ioffe Physicotechnical Institute, Russian Academy of Sciences, St. Petersburg, 194021 Russia

Received December 26, 2001

Abstract—Experimental data showing that preliminary hydrogen etching of a SiC substrate influences the concentration of donors or acceptors in autoepitaxial SiC layers are presented. The impurity concentration in the epitaxial layers grown on etched and unetched substrates may differ by an order of magnitude. A physical explanation of the observed correlation is proposed. The importance of the effect of competitive etching on the epitaxial growth is pointed out. © *2002 MAIK "Nauka/Interperiodica".*

Introduction. Preparation of a substrate surface is an important stage in the technology of manufacturing perfect epitaxial layers. This statement is especially valid for silicon carbide, a hard and chemically stable material, in which case it is rather difficult to remove a damaged surface layer after mechanical processing. Previously, we have already reported on a favorable effect of the preliminary etching in hydrogen on the structural quality of autoepitaxial SiC layers grown on the etched substrates, which is manifested by a decrease in the halfwidth of the Bragg X-ray scattering peak [1]. In addition to the hydrogen etching, we have studied some other methods of treatment of the surface of SiC substrates, including dry and wet oxidation followed by the oxide layer removal. Multiply repeated cycles of electrolytic oxidation followed by oxide dissolution using a method close to that described in [2] gave the best surface condition, but the X-ray diffraction still indicated the presence of an amorphous layer. Investigations performed with the aid of synchrotron radiation showed that a clear surface atomic structure can be obtained only upon hydrogen etching [3].

The etching of silicon carbide was also studied by other researchers [4–6]. Saidov *et al.* [7] showed that the character of SiC etching in H_2 depends not only on the temperature and velocity of the hydrogen flow, but on the heater material as well. This agrees with our notions about the operation of hydrogen reactors containing carbon parts without protective silicon carbide coating [8].

Recently [9], we have reported on a correlation between the impurity concentration in the epitaxial *n*-layers and the hydrogen pretreatment of substrates. Below we present the results extending this correlation to the *p*-layers as well. It is demonstrated that a difference in the impurity concentrations for epitaxial SiC layers grown on the substrates etched and unetched in hydrogen can amount up to an order of magnitude. The importance of the effect of competitive etching on the epitaxial SiC layer growth under low supersaturation conditions is pointed out.

Experimental procedures and results. The experiments were performed with *p*-6H-SiC (CREE Company) substrates with the orientation (0001)Si, 3° $(11\underline{2}0)$. The epitaxial films were grown in a methane–silane–hydrogen (CH_4–SiH_4–H_2) system using a hot-wall reactor with a glass–carbon composite heater [1]. The growth was conducted under low supersaturation conditions at a temperature of 1450°C and a growth velocity of 0.1–0.3 μm/h. The total flow rate of H_2 was 3 dm^3/min; the flow rate of 5% SiH_4 in Ar was 8 cm^3/min; and the flow rate of 10% CH_4 in Ar was varied so that the atomic ratio C/Si changed from 1 to 10.

The growth regime was attained in two ways: (a) increasing the temperature to a preset level in a hydrogen atmosphere, followed by admitting the active gas components; (b) increasing the temperature to a preset level, 2-h etching in hydrogen, and admitting the active gas components. At the process temperature indicated above, the gas phase in the reactor contains the molecules of CH_4, C_2H_2, and the related radicals (formed as a result of the interaction of hydrogen with carbon parts not protected by a SiC coating) [8]. Thus, the hydrogen etching of substrates proceeds essentially in a hydrogen atmosphere enriched with carbon-containing components; the etching rate is 0.6–0.8 μm/h.

The as-grown epitaxial films exhibited a mirror-smooth surface morphology. No special doping of the samples was carried out. The impurity concentration in the epitaxial layers was estimated using the capacitance–voltage characteristics of the Schottky barriers. Figure 1 shows the results of measurements of the con-

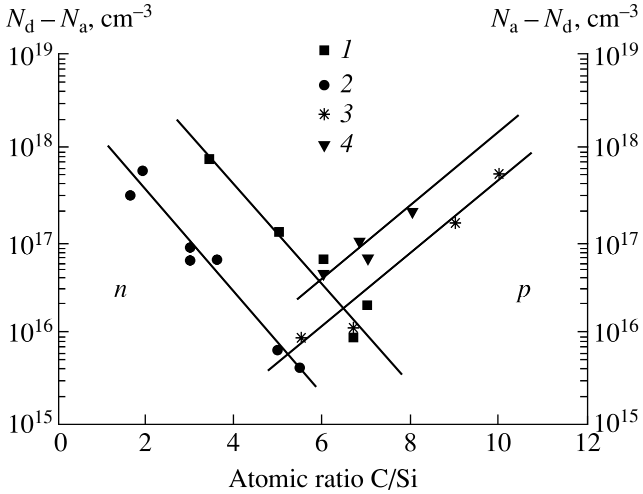

Fig. 1. Plots of the concentration of uncompensated donors ($N_d - N_a$) or acceptors ($N_a - N_d$) versus the atomic ratio C/Si in the gas phase for autoepitaxial layers of the (*1*, *2*) *n*- and (*3*, *4*) *p*-type grown on the substrates (*1*, *4*) unetched and (*2*, *3*) etched in hydrogen.

centration of uncompensated donors (acceptors) in autoepitaxial layers of the *n* and *p* types plotted versus the atomic ratio C/Si in the gas phase. The nature of the *n*- and *p*-type conductivity in SiC is considered elsewhere [8–10].

Discussion of results. As can be seen from Fig. 1, the hydrogen pretreatment of substrates is an important stage which allows the background impurity concentration to be reduced by an order of magnitude. This behavior is characteristic of the materials of both *n*- and *p*-type (cf. curves *1* versus *2* for the *n*-type and *3* versus *4* for the *p*-type in Fig. 1). From general considerations, it is evident that the level of impurity concentration must be related to the surface condition before and after etching. The state of the surface is characterized by the presence of atomic steps, their orientation or disorientation relative to the crystallographic planes, and other surface defects.

As is known, the unit cell of 6H-SiC comprises six SiC bilayers (~6 × 0.2 nm) closely stacked along the principal axis, some of which appear as steps on the disoriented, relatively singular face. The steps are energetically inequivalent. In the course of etching, the less tightly bound atoms leave the surface. Recent investigations of the 6H-SiC and 4H-SiC surfaces by scanning tunneling microscopy (STM) showed that the height of steps on the SiC surface upon prolonged hydrogen etching becomes equal to half of the lattice parameter of 6H- and 4H-SiC (3 and 2 bilayers along the principal axis, respectively [4]). An analogous pattern was observed for the SiC surface etched with hydrogen chloride [5]. Thus, prolonged hydrogen etching does not consist in simple removal of the defect layer from the surface. Based on these results, it was suggested [5] that etching removes the most energetic steps (belonging to the upper three bilayers) from the surface. The remaining, less energetic steps (most strongly incorporated into the layer) determine the surface morphology.

For the growth conditions used in our experiments, the growth rate (0.1–0.3 μm/h) competes with the etching rate. Therefore, we may suggest that the epitaxial growth under conditions admitting competitive etching is accompanied by the removal of the most energetic steps, so that the growth surface retains the structure of the etched substrate surface. Thus, the number of adsorption sites decreases, which eventually leads to a decrease in the concentration of uncompensated donors (acceptors).

Figure 2 shows the surface morphology of an epitaxial layer grown on a substrate preliminarily etched in hydrogen. The patterns were obtained by atomic force microscopy (AFM). The scale corresponds to an average roughness height not exceeding 2–3 6H-SiC bilayers. Thus, the above considerations qualitatively explain the observed difference of impurity concentrations in the layers grown on the etched and unetched substrates.

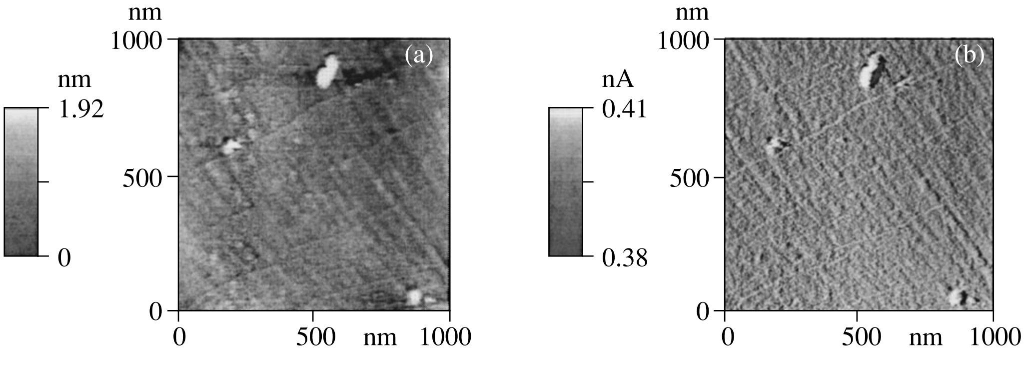

Fig. 2. AFM images showing the surface morphology of epitaxial 6H-SiC layers grown at [C]/[Si] ~ 5 on a hydrogen-etched substrate.

Conclusion. Prolonged etching in hydrogen (for $t \sim 2$ h at $T = 1450°\mathrm{C}$) makes the substrate surface less developed. The epitaxial growth under the conditions of competition with hydrogen etching retains the structure of the etched substrate surface and decreases the number of centers for impurity adsorption. The above considerations, together with the AFM data on the surface morphology, qualitatively explain the observed difference of impurity concentrations in the layers grown on the etched and unetched substrates.

Acknowledgments. The authors are grateful to Prof. W. Rihter and Dr. B. Schroeter (Friedrich-Schiller-University, Jena) for conducting the AFM measurements.

This study was supported by the Russian Foundation for Basic Research, project no. 00-02-16688.

REFERENCES

1. V. V. Zelenin, A. A. Lebedev, S. Starobinets, and V. E. Chelnakov, Mater. Sci. Eng. B **46**, 300 (1997).
2. M. I. Abaev, A. A. Vol’fson, M. I. Karklina, *et al.*, Izv. Akad. Nauk SSSR, Neorg. Mater. **15** (12), 2232 (1979).
3. T. S. Argunova, V. V. Zelenin, L. S. Kostina, *et al.*, in *Proceedings of the 4th All-Russia Conference on Physics of Semiconductors, Novosibirsk, 1999.*
4. T. L. Chu and R. B. Campbell, J. Elecrochem. Soc. **112** (9), 955 (1965).
5. V. Pamachandra, M. F. Brady, A. R. Smith, *et al.*, J. Electron. Mater. **27** (24), 308 (1998).
6. Chun-inchi Nakamura, T. Kimoto, H. Matsunami, *et al.*, Appl. Phys. Lett. **76** (23), 3412 (2000).
7. M. S. Saidov, Kh. Shamuratov, and M. A. Kadyrov, J. Cryst. Growth **87**, 519 (1988).
8. V. V. Zelenin, M. L. Korogodskiĭ, and A. A. Lebedev, Fiz. Tekh. Poluprovodn. (St. Petersburg) **35** (10), 1169 (2001) [Semiconductors **35**, 1117 (2001)].
9. V. V. Zelenin, M. L. Korogodskiĭ, and A. A. Lebedev, Fiz. Tekh. Poluprovodn. (St. Petersburg) **35** (10), 1172 (2001) [Semiconductors **35**, 1120 (2001)].
10. V. V. Zelenin, A. A. Lebedev, M. G. Rastegaeva, *et al.*, Mater. Sci. Eng. B **61**–**62**, 183 (1999).

Translated by P. Pozdeev

Technical Physics Letters, Vol. 28, No. 5, 2002, pp. 385–390. Translated from Pis'ma v Zhurnal Tekhnicheskoĭ Fiziki, Vol. 28, No. 9, 2002, pp. 63–76.
Original Russian Text Copyright © 2002 by Popov.

The Theory of Quasistatic Nanomachines

V. L. Popov

Paderborn University, 33098 Paderborn, Germany;
Institute of Strength Physics and Materials Science, Siberian Division, Russian Academy of Sciences, Tomsk, 634055 Russia
e-mail: popov@phys.uni.-paderborn.de

Received December 13, 2001

Abstract—The motion of a system of several bodies linked by bonds of variable length in a spatially periodic potential is studied. It is shown that quasistatic periodic variations of the system parameters in time can induce translational motion of the system in the absence of directed external forces, or motion in the direction opposite to that of an external force. To provide for the possibility of the induced translational motion, the system parameters (e.g., bond lengths) must vary in the space of these parameters according to closed trajectories containing one or several closed bifurcation sets of the given system. The bifurcation sets for some model systems are found. It is demonstrated that the proposed mechanism of the translational motion induction can be realized, in particular, by applying an alternating elliptically polarized electric field to particles of nanometer dimensions occurring on a chemically inert crystal (e.g., graphite) surface. *© 2002 MAIK “Nauka/Interperiodica”.*

Understanding the principles governing induction of a directed motion on the atomic level is important for development of the methods of controlled transport of nanodimensional objects or macromolecules on high-quality (atomically smooth or containing a limited number of defects) inert crystal surfaces. Examples of such surfaces are offered by the cleavages of mica or graphite. Investigations of the cleaved samples of these materials showed that large areas of virtually atomically smooth surface can be obtained [1]. Recently [2], it was demonstrated that a body or a group of bodies occurring in a spatially periodic potential can be driven so as to perform a directed macroscopic motion by applying a temporally periodic action. Following Porto *et al.* [3], objects of atomic or nanoscale dimensions, driven by external periodic actions to perform controlled motions, will be referred to below as nanomachines.

Previously [2], we considered the conditions necessary to induce the directed motion of a system of nanodimensional objects by an external dynamic action at a frequency comparable to the fundamental frequency of oscillations of this system occurring in the minimum of a spatially periodic potential. In this paper, it will be demonstrated that the frequency of such an external action, for which a directed macroscopic motion of the system is possible, is not limited from below. For small frequencies of the external action, the motion of the system can be considered as quasistatic. An analysis of this motion reduces to investigation of the singular points and lines in the space of slowly varying parameters of the system (bifurcation sets). The principles of such investigation proposed below, based on the search for singular sets of a system studied, will be illustrated by examples of the simplest model systems. Finally, the possibility of a practical realization of the induced motion of nanodimensional objects will be discussed.

The first example is offered by a nanomachine considered in [3]. In the simplest variant, the nanomachine comprises a system of three bodies, linked by rigid bonds of lengths l_1 and l_2, occurring in a spatially periodic harmonic potential. The total potential energy of this system is

$$U = U_0[\cos(k(x-l_1)) + \cos(kx) + \cos(k(x+l_2))], \quad (1)$$

where $k = 2\pi/a$ and a is the period of the potential. This expression can be rewritten as

$$U = U_0\sqrt{(\sin kl_1 - \sin kl_2)^2 + (1+\cos kl_1 + \cos kl_2)^2} \times \cos(kx-\varphi), \quad (2)$$

$$\tan\varphi = \frac{\sin kl_1 - \sin kl_2}{1+\cos kl_1+\cos kl_2}. \quad (3)$$

The phase φ is a continuous and uniquely determined function of parameters l_1 and l_2 along any trajectory in the (l_1, l_2) plane not passing through singular points, where the potential amplitude (2) becomes zero and the phase (3) is undetermined. The positions of such points are determined by the conditions

$$\begin{gathered} \sin kl_1 - \sin kl_2 = 0, \\ 1+\cos kl_1+\cos kl_2 = 0 \end{gathered} \quad (4)$$

or

$$kl_1 = \pi \pm \frac{\pi}{3} + 2\pi n, \quad kl_2 = \pi \pm \frac{\pi}{3} + 2\pi m, \quad (5)$$

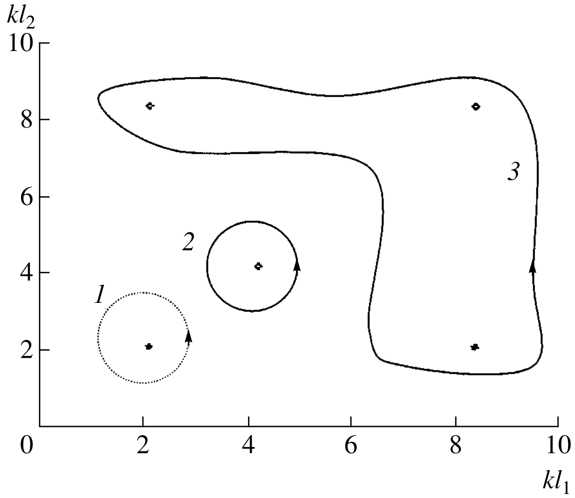

Fig. 1. The singular points of potential (1). When the bond lengths l_1 and l_2 vary along a closed contour *1* (*2*), the system moves by one spatial period in the negative (positive) direction.

where m and n are integers. Figure 1 shows the (l_1, l_2) plane on which the positions of several singular points are indicated. All such points are obtained by periodic continuation of the two points closest to the origin: $(kl_1, kl_2) = \left(\frac{2\pi}{3}, \frac{2\pi}{3}\right)$ and $(kl_1, kl_2) = \left(\frac{4\pi}{3}, \frac{4\pi}{3}\right)$. Upon going around a closed contour containing the first point in the (l_1, l_2) plane (Fig. 1, dashed contour *1*), the phase decreases by 2π, while going around the second point in the same direction (Fig. 1, solid contour *2*) increases the phase by 2π. The first point is assigned a topological index +1 and the second, –1. It can be readily checked in the general case that, when the bond lengths vary so that the system traverses an arbitrary closed contour not passing through singular points, the phase changes by $2\pi I$, where I is the sum of indices over all points contained inside the contour. For example, contour *3* in Fig. 1 contains three singular points, each indexed –1, so that traversing the contour changes the phase by -6π. Since changing the phase by a multiple of 2π is equivalent to translating the system of three bodies under consideration by one spatial period of the potential, we may conclude that any periodic variation of the lengths of bonds l_1 and l_2 corresponding to the system moving in the (l_1, l_2) plane along any closed contour containing singular points with a nonzero sum of indices would drive the system to perform a macroscopic translational motion. On the other hand, a periodic variation of the bond lengths corresponding to going around a contour either containing no singular points or containing such points with a zero sum of indices will not lead to macroscopic translation of the system.

Note that, in order to induce a directed macroscopic motion in the model considered above, it is sufficient to go around any singular point by a contour of arbitrarily small size. This property is not retained on the passage to models with periodic but anharmonic potentials. In this sense, the models with strictly harmonic potentials are structurally unstable. Consider a potential of the type

$$\Phi = U_0 \cos kx + U_1 \cos 2kx, \tag{6}$$

containing the second Fourier component with a small amplitude U_1. The total potential energy of the system of three bodies is

$$\begin{aligned} U = {} & U_0[\cos(k(x-l_1)) + \cos(kx) + \cos(k(x+l_2))] \\ & + U_1[\cos(2k(x-l_1)) + \cos(2kx) + \cos(2k(x+l_2))]. \end{aligned} \tag{7}$$

Let us find a bifurcation set for this potential, determined as a set of parameters for which the number of equilibrium states of the potential exhibits a change (thus violating continuous and unique dependence of the system equilibrium on the control parameters). The equilibrium states are determined by the condition

$$\partial U/\partial x = 0. \tag{8}$$

A bifurcation results in merging of the points of stable and unstable equilibrium, after which both these points disappear. Therefore, at the instant of bifurcation, the vanishing stationary point represents a point of inflection where

$$\partial^2 U/\partial x^2 = 0. \tag{9}$$

Thus, the system of equations (8) and (9) determines a bifurcation set for the given potential. In the case of a potential given by expression (7), these equations can be written in the following equivalent form:

$$\begin{aligned} & (\sin kl_1 - \sin kl_2) + 2(U_1/U_0)\cos kx(\cos^2 kx + 3\sin^2 kx) \\ & \times (\sin 2kl_1 - \sin 2kl_2) \\ & - 4(U_1/U_0)\sin^3 kx(1 + \cos 2kl_1 + \cos 2kl_2) = 0, \end{aligned} \tag{10}$$

$$\begin{aligned} & (1 + \cos kl_1 + \cos kl_2) + 2(U_1/U_0) \\ & \times \sin kx(\sin^2 kx + 3\cos^2 kx)(\sin 2kl_1 - \sin 2kl_2) \\ & + 4(U_1/U_0)\cos^3 kx(1 + \cos 2kl_1 + \cos 2kl_2) = 0. \end{aligned} \tag{11}$$

Obviously, the condition $U_1 = 0$ corresponds to a bifurcation set degenerating into a set (5) of isolated singular points. For $U_1/U_0 \ll 1$, the bifurcation set occurs in the vicinity of points (5). Therefore, to the first approximation, we can put $\sin 2kl_1 - \sin 2kl_2 \approx 0$ and $1 + \cos 2kl_1 + \cos 2kl_2 \approx -1$ in Eqs. (10) and (11), after which these equations acquire the form of

$$(\sin kl_1 - \sin kl_2) + 4(U_1/U_0)\sin^3 kx = 0,$$

$$(1 + \cos kl_1 + \cos kl_2) - 4(U_1/U_0)\cos^3 kx = 0.$$

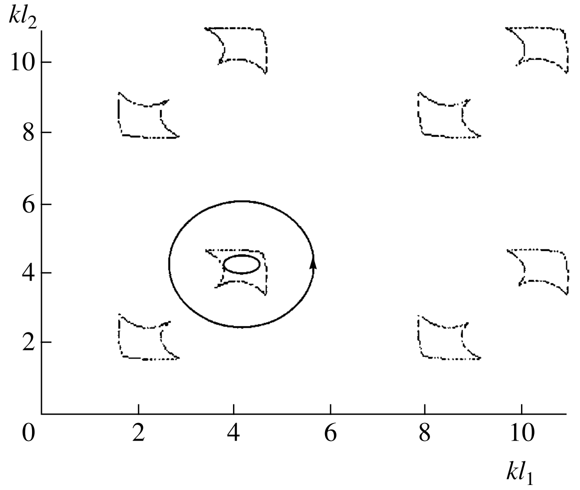

Fig. 2. Bifurcation sets of a tree-body system with potential energy (7) for $U_1/U_0 = 0.2$. The system performs translational motion only when the parameters vary along a contour containing the closed bifurcation sets.

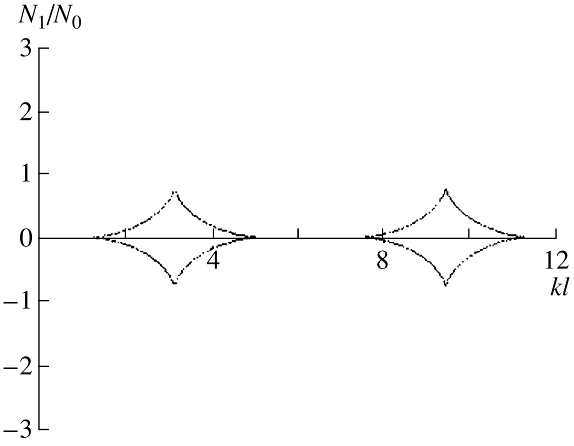

Fig. 3. Bifurcation sets of a two-particle nanomachine with an anharmonic spatially-periodic potential (6) for $U_1/U_0 = 0.2$.

From these relationships, it follows that

$$\begin{aligned}&(\sin kl_1 - \sin kl_2)^{2/3}\\&+ (1 + \cos kl_1 + \cos kl_2)^{2/3} = (4U_1/U_0)^{2/3}.\end{aligned} \tag{12}$$

Figure 2 shows a bifurcation set of the system for $U_1/U_0 = 0.2$. When the parameters l_1 and l_2 vary along a contour containing one of the bifurcation sets (see solid external loop in Fig. 2), the phase changes by ±2π (with the sign depending on the particular singular region and the direction of traversing). A periodic action corresponding to the motion around such a contour would drive the system to perform a translational motion during one period of action. On the contrary, variation of the parameters along the contour inscribed into a bifurcation set (see the internal loop in Fig. 2) leaves the phase unchanged, which corresponds to oscillations about an equilibrium position.

The second example is offered by a system of two bodies, linked by a bond of length l, occurring in a spatially periodic potential. It is suggested that the system models an electrically polarized object on the surface of a crystal. Application of an external electric field would change the object length and the forces of normal pressure acting upon the bodies (due to the electric field component perpendicular to the "substrate" surface); note that the forces applied to the first and second body are oriented in the opposite directions. This would lead to an increase in amplitude of the periodic potential for one of the bodies and to a decrease in this amplitude for another body. The system under consideration can be modeled by a potential energy of the type

$$\begin{aligned}U &= (N_0 + N_1)\cos(k(x - l/2))\\&\quad + (N_0 - N_1)\cos(k(x + l/2))\\&= 2\sqrt{N_0^2\cos^2\frac{kl}{2} + N_1^2\sin^2\frac{kl}{2}}\cos(kx - \varphi),\end{aligned} \tag{13}$$

$$\tan\varphi = \frac{N_1}{N_0}\tan\frac{kl}{2}, \tag{14}$$

where N_0 is the average amplitude of the periodic potential and N_1 is the variation of this amplitude under the action of the normal component of the electric field.

The set of singular points in which the phase φ is undetermined corresponds to the conditions $N_1 = 0$, $\cos(kl/2) = 0$. In the plane of parameters $(N_1/N_0, kl)$, this set corresponds to points $(0, \pi + 2\pi n)$. A change in the phase by 2π, corresponding to translation of the system by one spatial period, takes place upon going around any of these points by a closed contour of arbitrarily small radius. Similar to the first example, this behavior is not retained on the passage to anharmonic periodic potentials. For example, the appearance of the second Fourier harmonic transforms the singular points into closed bifurcation figures (Fig. 3). In such a case, the translational motion can be induced only by varying the system parameters along a contour containing such a bifurcation figure.

The above models are of interest for the development of methods for manipulation with nanodimensional objects, including systems capable of transporting a "load." An important problem is determining the conditions under which such objects can move in the direction opposite to that of the average external force. This possibility was considered in detail in [2]. For an analysis of this problem, let us return to the nanomachine comprising three bodies occurring in a strictly harmonic potential in the presence of a constant external force $-F$, which is modeled by the term Fx in the

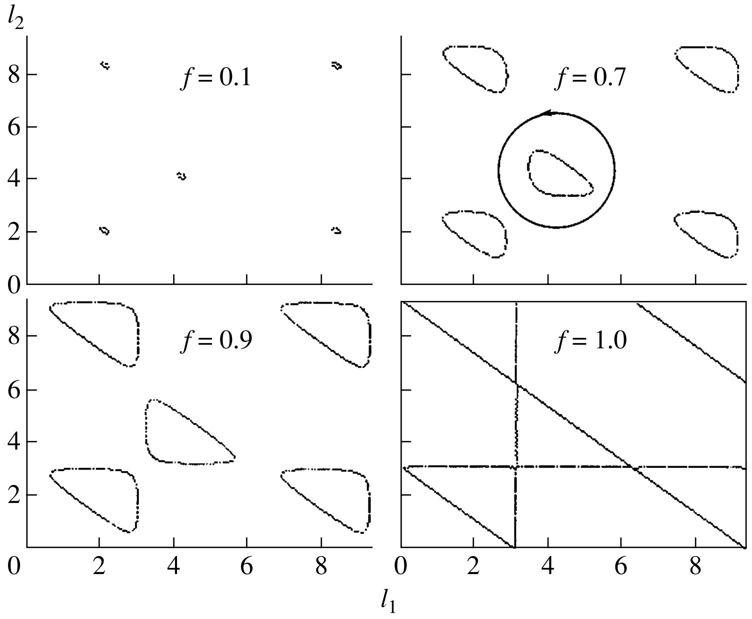

Fig. 4. Bifurcation sets of a tree-particle nanomachine in the presence of a constant external force. A contour containing a bifurcation set can be drawn only provided that $f < 1$.

potential energy. The total potential energy of this system is

$$U = U_0[\cos(k(x - l_1)) + \cos(kx) + \cos(k(x + l_2))] + Fx, \quad (15)$$

and the bifurcation set is determined by the conditions

$$\frac{1}{U_0k}\frac{\partial U}{\partial x} = -(1 + \cos kl_1 + \cos kl_2)\sin kx + (\sin kl_1 - \sin kl_2)\cos kx + \frac{F}{U_0k} = 0, \quad (16)$$

$$\frac{1}{U_0k^2}\frac{\partial^2 U}{\partial x^2} = -(1 + \cos kl_1 + \cos kl_2)\cos kx - (\sin kl_1 - \sin kl_2)\sin kx = 0. \quad (17)$$

Multiplying Eq. (16) by sinkx, Eq. (17) by coskx, and summing the products, we obtain

$$(1 + \cos kl_1 + \cos kl_2) = \frac{F}{U_0k}\sin kx. \quad (18)$$

Multiplying Eq. (16) by coskx, Eq. (17) by sinkx, and subtracting the products, we obtain

$$\sin kl_2 - \sin kl_1 = \frac{F}{U_0k}\cos kx. \quad (19)$$

Taking the squares of the two last equations and adding the obtained relations, we arrive at the equation

$$(1 + \cos kl_1 + \cos kl_2)^2 + (\sin kl_1 - \sin kl_2) = \left(\frac{F}{U_0k}\right)^2. \quad (20)$$

Figure 4 shows the bifurcation sets corresponding to this equation for several values of the parameter $f = F/U_0k$. Here, a translational motion is induced only when the parameters l_1 and l_2 vary along a contour containing the bifurcation set. Obviously, this is possible only when $f < 1$. Thus, a maximum pulling force of this nanomachine (however, still unattainable in practice) is $F_{\max} = U_0k$.

A fully analogous calculation for the machine comprising two bodies with the potential energy $U = (N_0 + N_1)\cos(k(x - l/2)) + (N_0 - N_1)\cos(k(x + l/2)) - Fx$ leads to a bifurcation set (Fig. 5) determined by the equation

$$\cos^2\frac{kl}{2} + \left(\frac{N_1}{N_0}\right)^2\sin^2\frac{kl}{2} = \left(\frac{F}{2N_0k}\right)^2. \quad (21)$$

Here, the possibility of inducing a translational motion by varying parameters over a contour containing singular sets in the plane of parameters is retained for $f = F/2N_0k < 1$. In this case, the maximum pulling force is $F_{\max} = 2N_0k$.

The systems considered above are models of a polarized particle (dipole) occurring in an alternating electric field. From a practical standpoint, of much greater interest is the possibility of manipulating neutral and unpolarized particles. Let us formulate a model of a nanoparticle, possessing electrostriction properties, occurring on the surface of a crystal in an alternat-

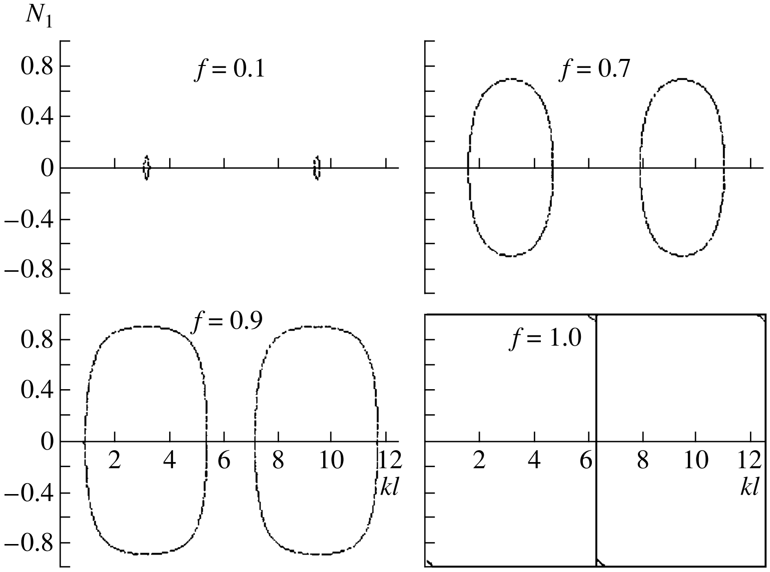

Fig. 5. Bifurcation sets of a two-particle nanomachine in the presence of a constant external force. A contour containing a bifurcation set can be drawn only provided that $f < 1$.

ing periodic electric field containing both tangential and normal components. Under the action of this field, the particle dimensions exhibit variations. In the case of the particle representing a compound belonging to a space symmetry group possessing the center of inversion, a change in linear dimensions of the particle is a second-order effect in the field strength. Simultaneously, the field induces polarization of the particle (proportional to the tangential component of the field strength) and opposite changes in the pressure at the positively and negatively charged ends of the particle. This system can be described by the potential energy (13) with

$$l = l_0 + \beta E^2, \quad N_1 = \alpha E_\perp E_\parallel, \tag{22}$$

where $E_\perp$ and $E_\parallel$ are the normal and tangential components of the electric field strength, $E^2 = E_\perp^2 + E_\parallel^2$, β is the electrostriction constant, and α is the polarizability of the particle. In the case of an elliptically polarized alternating field with the components varying by the harmonic law, $E_\perp = E_{\perp,0}\cos\omega t$ and $E_\parallel = E_{\parallel,0}\sin\omega t$, we obtain

$$l = l_0 + \frac{\beta}{2}(E_{\perp,0}^2 + E_{\parallel,0}^2) + \frac{\beta}{2}(E_{\perp,0}^2 - E_{\parallel,0}^2)\cos 2\omega t, \tag{23}$$

$$N_1 = \frac{\alpha}{2}E_{\perp,0}E_{\parallel,0}\sin 2\omega t, \tag{24}$$

which yields

$$\left(\frac{l - l_0 - \frac{\beta}{2}(E_{\perp,0}^2 + E_{\parallel,0}^2)}{\frac{\beta}{2}(E_{\perp,0}^2 - E_{\parallel,0}^2)}\right)^2 + \left(\frac{N_1}{\frac{\alpha}{2}E_{\perp,0}E_{\parallel,0}}\right)^2 = 1. \tag{25}$$

The set of l and N_1 values satisfying this equation represents an ellipse centered at $(l, N_1) = \left(l_0 + \frac{\beta}{2}(E_{\perp,0}^2 + E_{\parallel,0}^2), 0\right)$. If we select $l_0 + \frac{\beta}{2}(E_{\perp,0}^2 + E_{\parallel,0}^2) = \pi + 2\pi n$, the elliptic contour (25) contains the singular point and, hence, traversing this contour translates the system through one spatial period of the potential. Note that one period of variation of the electric field strength corresponds to two passages along the closed contour (this frequency doubling is seen from Eqs. (23) and (24)), so that the system travels over two spatial periods of the potential during one period of oscillations of the electric field.

How can the above models be realized in practice? Now it will be demonstrated that a system representing two bodies linked by the bond of a variable length models a crystalline particle in contact with a solid crystal surface. Indeed, consider a crystalline particle of length L with a lattice period of $2\pi/k_2$ occurring on the surface of a crystal substrate with a lattice period of $2\pi/k_1$ (Fig. 6). Below, u denotes the current coordinate of the points on the particle surface (u is counted from the particle center of gravity), and x is the coordinate of the center of gravity measured on the substrate surface. Let the interaction between particle and substrate be so weak that we can ignore deformation of the particle due to this interaction. Estimates show that this assumption is valid for the particles of nanometer size, provided that the interaction with substrate has a van-der-Waals character (e.g., for nearly any particles on the graphite surface). For calculating the dependence of the potential energy of the particle on the coordinate of the center

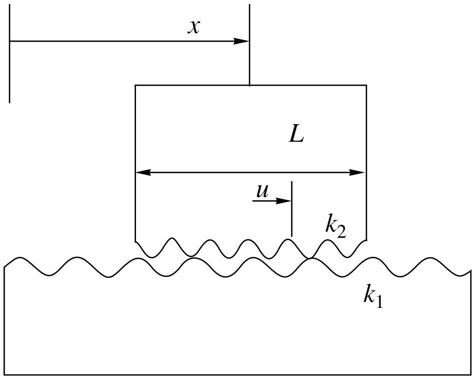

Fig. 6. Schematic diagram of a crystalline nanoparticle with a lattice period of $2\pi/k_2$ occurring on the flat surface of a crystal substrate with a lattice period of $2\pi/k_1$.

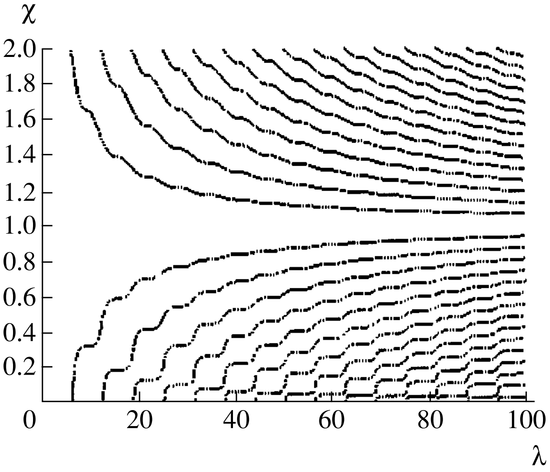

Fig. 7. Solutions to Eq. (28) determining the positions of singular points (critical length) of a crystalline particle on the surface of a crystal substrate for various ratios κ of lattice periods of the particle and substrate.

of gravity, we assume that the charge density distribution on the particle surface has the form of $q = q_0\cos k_2 u$, and the potential created by the substrate can be written as $\varphi = \varphi_0\cos k_1(x + u)$. Then the potential energy of interaction between the particle and the substrate is

$$U = \int_{-L/2}^{L/2} q_0\varphi_0\cos k_2 u\cos k_1(x+u)\,du = q_0\varphi_0\cos k_1 x \times\left[\frac{\sin\left((k_1+k_2)\frac{L}{2}\right)}{k_1+k_2} + \frac{\sin\left((k_1-k_2)\frac{L}{2}\right)}{k_1-k_2}\right]. \qquad (26)$$

In order to reveal an analogy with the models considered above, let us first consider the case of close (but not equal!) lattice periods ($k_1 - k_2 \ll k_1 + k_2$). In this case, we can neglect the first term in (26) in comparison with the second term, and the potential energy simplifies to

$$U = \frac{q_0\varphi_0}{k_1-k_2}\cos k_1 x\sin\left((k_1-k_2)\frac{L}{2}\right),$$

which coincides in form with the potential of a pair of particles in a potential with the wavevector k_1 and the effective bond length

$$l_{\text{eff}} = \frac{\pi}{k_1} + \left(1 - \frac{k_2}{k_1}\right)L. \qquad (27)$$

In the general case, the potential energy (26) cannot be reduced to the potential energy of a system of two bodies. Nevertheless, the general case can be also analyzed by methods analogous to those employed above. In particular, the singular points of potential (26) are determined by the condition of zero amplitude:

$$\frac{\sin\left((k_1+k_2)\frac{L}{2}\right)}{k_1+k_2} + \frac{\sin\left((k_1-k_2)\frac{L}{2}\right)}{k_1-k_2} = 0.$$

Using the notation $k_1 L = \lambda$ and $k_2/k_1 = \kappa$, we can rewrite this relationship as

$$\frac{\sin((1+\kappa)\lambda/2)}{1+\kappa} + \frac{\sin((1-\kappa)\lambda/2)}{1-\kappa} = 0. \qquad (28)$$

Figure 7 shows the solutions to this equation. Each ratio of the lattice periods of the particle and substrate corresponds to a discrete set of values of the particle length L for which the potential amplitude equals zero. Upon going around a closed contour containing such points in the (L, N_1) plane, the particle will be translated by one spatial period of the substrate. As was demonstrated above, this can be performed using the electrostriction properties of the particle. Thus, the models considered above demonstrate the possibility of a directed motion of nanoparticles along a crystal surface under the action of oscillating elliptically polarized electric field. The direction of particle motion is determined by the polarization orientation (and, hence, by the direction of going around the singular points in the plane of parameters).

Acknowledgments. The author is grateful to O.K. Dudko for valuable remarks and to M.V. Popov for manufacturing an acting model favoring better understanding of the conditions of induced directed motion in a periodic field. Special thanks to the Academic Exchange Agency of Germany (DAAD) for financial support.

REFERENCES

1. H. Hölscher, U. D. Schwarz, O. Zwörner, and R. Wiesendanger, Phys. Rev. B **57** (4), 2477 (1998).
2. V. L. Popov, Zh. Tekh. Fiz. (2002) (in press).
3. M. Porto, M. Urbakh, and J. Klafter, Phys. Rev. Lett. **84** (26), 6058 (2000).

Translated by P. Pozdeev

Technical Physics Letters, Vol. 28, No. 5, 2002, pp. 391–394. Translated from Pis'ma v Zhurnal Tekhnicheskoĭ Fiziki, Vol. 28, No. 9, 2002, pp. 77–84.
Original Russian Text Copyright © 2002 by Latyshev, Yushkanov.

The Onsager Relations Analyzed Using an Ellipsoidal Statistical Equation

A. V. Latyshev and A. A. Yushkanov
Moscow State Pedagogical University, Moscow, Russia
e-mail: latyshev@orc.ru; yushkanov@inbox.ru

Received December 3, 2001

Abstract—Validity on the well-known Onsager reciprocal relations $L_{12} = L_{21}$ is verified in the kinetic theory of gases taking into account mass and heat transfer near the surface. Using an analytical solution to the ellipsoidal statistical equation (providing for the true Prandtl number), it is demonstrated that the Onsager relations are obeyed, at least to within exponential corrections of the type exp(–1/Kn) in the Knudsen number. © *2002 MAIK "Nauka/Interperiodica".*

This paper continues our study [1] devoted to verification of the Onsager relation proceeding from the Boltzmann–Krook–Welander (BKW) equation. However, this equation leads to incorrect Prandtl number of Pr = 1 [2]. Therefore, the task of justifying the Onsager relations based on a kinetic equation corresponding to a true Prandtl number (Pr ≈ 2/3) remained unsolved. The purpose of this study was to fill the gap. To this end, we will employ an ellipsoidal statistical equation leading to a correct (true) Prandtl number.

Let us consider a classical problem on the motion of a gas, involving the mass and heat transfer, in a channel under the action of temperature and pressure gradients [2]. The relative drops of temperature and pressure are assumed to be small so as to allow the problem to be linearized. We will assume that the Knudsen number Kn, representing the ratio of the mean free path of molecules in the gas phase to the channel thickness, is small as well. Note that some of the flows are localized in the Knudsen layer. Therefore, the Kn value, albeit small, cannot be considered equal to zero.

Consider a Cartesian system of coordinates with the origin at the center of the channel and the *yz* plane parallel to the top and bottom of the channel. Let the mass and heat flows be parallel to the *z* axis and the relative temperature and pressure changes obey the conditions $|\Delta T|/T \ll 1$ and $|\Delta p|/p \ll 1$, where $\Delta T = T_2 - T_1$; $\Delta p = p_2 - p_1$; and T_1, p_1 and T_2, p_2 are the gas temperature and pressure at the channel input and output cross sections. The fluxes of mass J_M and heat J_Q along the channel are proportional to the pressure and temperature drops and can be described as follows [3]:

$$J_m = -2L_{11}(aL)v\frac{\Delta p}{p} - 2L_{12}(aL)\frac{\Delta T}{T^2},$$

$$J_Q = -2L_{21}(aL)v\frac{\Delta p}{p} - 2L_{22}(aL)\frac{\Delta T}{T^2},$$

where $v = 1/\rho = 1/(nm)$ is the specific volume, a is the channel thickness, and L is the channel length (along the y axis).

As indicated above, our purpose is to prove the Onsager reciprocal relations. Let us present the linearized distribution function in the form of $f = f_0(1 + \varphi)$, where f_0 is the absolute Maxwellian and introduce the dimensionless velocity of gas molecules $\mathbf{c} = \sqrt{\beta}\,\mathbf{v}$, $\beta = m/2kT$. The mass and heat fluxes can be expressed via the function φ,

$$\sqrt{\beta}J_M = nm\pi^{-3/2}\int dxdy\int\exp(-c^2)c_z\varphi d^3c,$$

$$\sqrt{\beta}J_Q = nkT\pi^{-3/2}\int dxdy\int\exp(-c^2)c_z\left(c^2-\frac{5}{2}\right)\varphi d^3c,$$

$$\int dxdy = \int dy\int_{-a}^{a}dx = \frac{L}{\nu\sqrt{\beta}}\int_{-b}^{b}dx', \quad b = a\sqrt{\beta}\nu \sim 1/\mathrm{Kn}.$$

Now we can write the mass and heat fluxes in the dimensionless form

$$J'_M = \frac{\nu}{4aLnkT}J_M, \quad J'_Q = \frac{m\nu}{4aLnk^2T^2}J_Q,$$

or in terms of L_{ij},

$$J'_M = -\frac{v\nu}{2}L_{11}\frac{\Delta p}{p} - \frac{\nu}{2Tp}L_{12}\frac{\Delta T}{T},$$

$$J'_Q = -\frac{\nu}{2pT}L_{21}\frac{\Delta p}{p} - \frac{\rho\nu}{2p^2T}\frac{\Delta T}{T}.$$

Introducing the dimensionless Onsager coefficients L'_{ij}, we can rewrite these fluxes as

$$J'_M = -L'_{11}\frac{\Delta p}{p} - L'_{12}\frac{\Delta T}{T}, \quad J'_Q = -L'_{21}\frac{\Delta p}{p} - L'_{22}\frac{\Delta T}{T},$$

1063-7850/02/2805-0391$22.00 © 2002 MAIK "Nauka/Interperiodica"

$$L'_{12} = \frac{\nu}{2Tp}L_{12}, \quad L'_{21} = \frac{\nu}{2Tp}L_{21},$$

and returning to the function φ, as

$$J'_M = \pi^{-3/2}\int_{-b}^{b} dx'\int \exp(-c^2)c_z\varphi d^3c,$$

$$J'_Q = \pi^{-3/2}\int_{-b}^{b} dx'\int \exp(-c^2)c_z\left(c^2-\frac{5}{2}\right)\varphi d^3c.$$

Finally,

$$J'_M = -S_{11}k_p - S_{12}k_t, \quad J'_Q = -S_{21}k_p - S_{22}k_t,$$

$$k_t = \frac{\partial \ln T}{\partial z'}, \quad k_p = \frac{\partial \ln p}{\partial z'},$$

$$\frac{\Delta p}{p} = z'_0 k_p, \quad \frac{\Delta T}{T} = z'_0 k_t,$$

$$z'_0 = \nu\sqrt{\beta}z_0, \quad S_{ij} = L'_{ij}z'_0,$$

where z'_0 and z_0 are the dimensionless and dimensional channel lengths, respectively, and ν is the frequency of collisions.

Now we have to prove that $S_{12} = S_{21}$. Representing the function φ as a sum of two terms proportional to k_p and k_t,

$$\varphi = \varphi_p k_p + \varphi_t k_t, \tag{1}$$

we can express the mass and heat fluxes as

$$-S_{12} = \pi^{-3/2}\int_{-b}^{b} dx'\int \exp(-c^2)c_z\varphi_t d^3c,$$

$$-S_{21} = \pi^{-3/2}\int_{-b}^{b} dx'\int \exp(-c^2)c_z\left(c^2-\frac{5}{2}\right)\varphi_p d^3c.$$

Consider the ellipsoidal statistical equation in dimensionless variables:

$$\begin{gathered} c_x\frac{\partial\varphi}{\partial x} + c_z k_p + c_z\left(c^2-\frac{5}{2}\right)k_t + \varphi(x, \mathbf{c}) \\ = 2c_z\pi^{-3/2}\int \exp(-c'^2)c'_z(1-c_xc'_x)\varphi(x, \mathbf{c}')d^3c'. \end{gathered} \tag{2}$$

Assuming that the gas molecules exhibit diffuse reflection from the channel walls,

$$\varphi(\pm b, c_x) = 0, \quad \mp c_x > 0, \tag{3}$$

we can write a partial solution to Eq. (2),

$$\begin{aligned} \varphi_0(x, \mathbf{c}) = {} & c_z\Big[2U + 2\left(x - \frac{2}{3}c_x\right)k_t \\ & + \left(2c_x^2 - 2xc_x + \frac{3}{2}x^2\right)k_p - \left(c^2 - \frac{5}{2}k_t\right)\Big]. \end{aligned}$$

Using expression (1), we can separate the problem formulated by Eqs. (2) and (3) into two, proportional to k_p and k_t.

Thus, we obtain problem 1,

$$\begin{gathered} c_x\frac{\partial\varphi_p}{\partial x} + \varphi_p(x, \mathbf{c}) + c_z \\ = 2c_z\pi^{-3/2}\int \exp(-c'^2)c'_z(1-c_xc'_x)\varphi_p(x, \mathbf{c}')d^3c', \\ \varphi_p(\pm b, c_x) = 0, \quad \mp c_x > 0, \end{gathered}$$

and problem 2,

$$\begin{gathered} c_x\frac{\partial\varphi_t}{\partial x} + \varphi_t(x, \mathbf{c}) + c_z\left(c^2 - \frac{5}{2}\right) \\ = 2c_z\pi^{-3/2}\int \exp(-c'^2)c'_z(1-c_xc'_x)\varphi_t(x, \mathbf{c}')d^3c', \\ \varphi_t(\pm b, c_x) = 0, \quad \mp c_x > 0. \end{gathered}$$

A solution to problem 1 will be found in the form of

$$\varphi_p = c_z\psi(x, \mu), \ \mu = c_x.$$

This yields problem 1',

$$\begin{gathered} \mu\frac{\partial\psi}{\partial x} + \psi(x, \mu) + 1 \\ = \frac{1}{\sqrt{\pi}}\int_{-\infty}^{\infty} \exp(-\mu'^2)(1-\mu\mu')\psi(x, \mu')\psi(x, \mu')d\mu', \end{gathered} \tag{4}$$

$$\psi(\pm b, \mu) = 0, \quad \mp\mu > 0,$$

which has a partial solution

$$\psi_0(x, \mu) = 2U_p + \left(2\mu^2 - 2x\mu + \frac{3}{2}x^2\right).$$

Consider a homogeneous equation corresponding to the inhomogeneous Eq. (4):

$$\begin{gathered} \mu\frac{\partial\psi}{\partial x} + \psi(x, \mu) \\ = \frac{1}{\sqrt{\pi}}\int_{-\infty}^{\infty} \exp(-\mu'^2)(1-\mu\mu')\psi(x, \mu')d\mu'. \end{gathered} \tag{5}$$

Separating variables in Eq. (5),

$$\psi_\eta(x, \mu) = \exp(-x/\eta)F(\eta, \mu),$$

where η is a spectral parameter, we obtain a characteristic equation

$$(\eta-\mu)F(\eta,\mu)=\frac{1}{\sqrt{\pi}}\eta,\quad \int\limits_{-\infty}^{\infty}\exp(-\mu^2)F(\eta,\mu)d\mu\equiv 1.$$

A solution to this characteristic equation is taken in the space of generalized functions [4]

$$F(\eta,\mu)=\frac{1}{\sqrt{\pi}}P\frac{1}{\eta-\mu}+\exp(\eta^2)\lambda(\eta)\delta(\eta),$$

where

$$\lambda(z)=1+\frac{1}{\sqrt{\pi}}z\int\limits_{-\infty}^{\infty}\exp(-u^2)\frac{du}{u-z}$$

is the dispersion function of Cercignani [5].

By analogy with [1], one can readily check that a solution to problem 1' has the following form:

$$\psi(x,\mu)=\psi_0(x,\mu)+\int\limits_{-\infty}^{\infty}\exp(-x/\eta)F(\eta,\mu)d\eta,$$

where $a(\eta)$ is an unknown function (a coefficient of the continuous spectrum).

By analogy with [1], we also obtain

$$2U_p=2(V_1^2/2-3/4)-2V_1(b+V_1)-3b^2/2,$$

$$2\sqrt{\pi}i\mu a_p(\mu)\exp(b/\mu)$$

$$=2(b+V_1+\mu)\left(\frac{1}{X^+(\mu)}-\frac{1}{X^-(\mu)}\right),$$

where

$$X(z)=\frac{1}{z}\exp\left(\frac{1}{\pi}\int\limits_0^{\infty}\frac{\theta(u)-\pi}{u-z}du\right),$$

$$V_1=-\frac{1}{\pi}\int\limits_0^{\infty}[\theta(u)-\pi]du,$$

$$\theta(u)=\arg\lambda^+(u),\quad \theta(0)=0.$$

Now we can determine the heat flux,

$$-S_{21}=\frac{1}{2\sqrt{\pi}}\int\limits_{-b}^{b}dx'\int\limits_{-\infty}^{\infty}\exp(-\mu^2)\left(\mu^2-\frac{1}{2}\right)\psi_p(x,\mu)d\mu$$

$$=b+(b+V_1)\left(\frac{V_1^2}{2}-\frac{3}{4}\right)+V_3^*,$$

where

$$V_3^*=-\frac{1}{2\pi i}\int\limits_0^{\infty}\left[\frac{1}{X^+(u)}-\frac{1}{X^-(u)}\right]udu.$$

A solution to problem 2 will be found in the form of

$$\varphi_t=c_z[f(x,\mu)+(c_y^2+c_z^2-2)\xi(x,\mu)],\quad \mu=c_x,$$

which separates into problem 2a,

$$\mu\frac{\partial f}{\partial x}+f(x,\mu)+\mu^2-\frac{1}{2}$$

$$=\frac{1}{\sqrt{\pi}}\int\limits_{-\infty}^{\infty}\exp(-\mu'^2)(1-\mu\mu')f(x,\mu')d\mu',$$

$$f(\pm b,\mu)=0,\quad \mp\mu>0$$

(where $f_{to}(x,\mu)=2U_t-\left(\mu^2-\frac{1}{2}\right)$ and problem 2b

$$\mu\frac{\partial\xi}{\partial x}+\xi(x,\mu)=0,\quad \xi(\pm b,\mu)=0,\quad \mp\mu>0.$$

A solution to problem 2b is not required, while the one to problem 2a is as follows:

$$f(x,\mu)=f_{to}(x,\mu)+\int\limits_{-\infty}^{\infty}\exp(-x/\eta)F(\eta,\mu)a_t(\eta)d\eta,$$

where

$$2U_t=V_1^2-1/2-V_1^2/2+3/4=(V_1^2+1/2)/2,$$

$$2\sqrt{\pi}i\mu a_t(\mu)\exp(b/\mu)=-(V_1+\mu)\left[\frac{1}{X^+(\mu)}-\frac{1}{X^-(\mu)}\right].$$

Now we can determine the mass flux

$$-S_{21}=\frac{1}{2\sqrt{\pi}}\int\limits_{-b}^{b}dx'\int\limits_{-\infty}^{\infty}\exp(-\mu^2)f(x',\mu)d\mu$$

$$=\frac{1}{2\sqrt{\pi}}\int\limits_{-b}^{b}dx'\int\limits_{-\infty}^{\infty}\exp(-\mu^2)$$

$$\times\left[2U_t-\left(\mu^2-\frac{1}{2}\right)+2\int\limits_0^{\infty}\exp(-x'/\eta)F(\eta,\mu)a_t(\eta)d\eta\right]d\mu$$

$$=2bU_t+\frac{1}{\sqrt{\pi}}\int\limits_0^{\infty}\exp(b/\eta)\eta a_t(\eta)d\eta$$

$$=b+(b+V_1)(V_1^2/2-3/4)+V_3^*,$$

which exactly coincides with the expression for $-S_{12}$.

Note that the quantities S_{12} and S_{21} can be presented in the following form:

$$S_{ij}=2br_{ij}\ (i,j=1,2;\ i\neq j),\quad r_{ij}=r_{ij}^{(0)}+\frac{1}{b}r_{ij}^{(1)}.\quad (6)$$

Since $2b$ is a dimensionless channel thickness, the quantities $r_{ij}^{(0)}$ and $r_{ij}^{(1)}$ correspond to fluxes per unit channel thickness and obey the relationships

$$r_{12}^{(0)} = r_{21}^{(0)}, \quad r_{12}^{(1)} = r_{21}^{(1)}. \tag{7}$$

Since $1/b \sim \mathrm{Kn}$, expressions (6) represent the expansions of r_{12} and r_{21} into series in powers of Kn. These expansions contain all nonzero terms, except for the omitted terms proportional to exp(– 1/Kn) (which cannot be expanded into a series in powers of Kn).

Of the two relationships (7), only the first was considered previously [6, 7], using the approximated method of moments (for the BCV equation). In our paper, validity of both relationships (7) is proved analytically in terms of the ellipsoidal statistical equation.

Thus, the Onsager reciprocal relations are strictly obeyed for the kinetic ellipsoidal statistical equation, at least to within exponential corrections of the type exp(–1/Kn) in the Knudsen number.

Acknowledgments. This study was partly supported by the Russian Foundation for Basic Research, project no. 99-01-00336.

REFERENCES

1. A. V. Latyshev and A. A. Yushkanov, Izv. Akad. Nauk, Mekh. Zhidk. Gaza, No. 1, 173 (2001).
2. M. N. Kogan, *Dynamics of Rarefied Gas. Kinetic Theory* (Nauka, Moscow, 1967).
3. S. R. de Groot and P. Mazur, *Nonequilibrium Thermodynamics* (North-Holland, Amsterdam, 1962; Mir, Moscow, 1964).
4. V. S. Vladimirov, *Generalized Functions in Mathematical Physics* (Nauka, Moscow, 1976).
5. C. Cercignani, *Mathematical Methods in Kinetic Theory* (Plenum, New York, 1969; Mir, Moscow, 1973).
6. Yu. I. Yalamov and M. N. Gaĭdukov, Kolloidn. Zh. **38** (6), 1149 (1976).
7. Yu. I. Yalamov, M. N. Gaĭdukov, and A. M. Golikov, Kolloidn. Zh. **39** (6), 1132 (1977).

Translated by P. Pozdeev

Technical Physics Letters, Vol. 28, No. 5, 2002, pp. 395–398. Translated from Pis'ma v Zhurnal Tekhnicheskoĭ Fiziki, Vol. 28, No. 9, 2002, pp. 85–91.
Original Russian Text Copyright © 2002 by Ginzburg, Zaĭtsev, Ilyakov, Kulagin, Rozental'.

Self-Modulated Generation Observed in a Delayed Feedback Relativistic Microwave Gyrotron

N. S. Ginzburg, N. I. Zaĭtsev, E. V. Ilyakov, I. S. Kulagin, and R. M. Rozental'
Institute of Applied Physics, Russian Academy of Sciences, Nizhni Novgorod, Russia
e-mail: rrz@appl.sci-nnov.ru

Received November 22, 2001

Abstract—Self-modulated generation regimes were studied in a delayed feedback relativistic gyrotron operating on the H_{01} mode with a central frequency of 9.2 GHz. At a fixed electron beam energy of 230 keV, an increase in the electron beam current from 10 to 45 A led to the transition from a stationary to periodic self-modulated generation regime. The modulation period was about 16 ns, while the relative amplitude of the modulation increased in proportion to the beam current, reaching up to 90%. The microwave pulse duration exceeded 6 μs at an average power of up to 1 MW. The experimental data obtained agree well with the results of simulation using the PIC code KARAT. © *2002 MAIK "Nauka/Interperiodica".*

At present, considerable effort of researchers is devoted to the investigation of a nonlinear dynamics of powerful microwave generators with a view to the possibility of obtaining high-power multimode and noise radiation. In particular, recently we observed periodic and stochastic self-modulated regimes at an average power of up to 2 MW in a relativistic 3-cm backward-wave tube [1]. The purpose of this experimental study was to observe self-modulated generation regimes in a relativistic gyrotron. As is known, gyrotrons with subrelativistic electron beams are the most powerful sources of radiation in the millimetric wavelength range [2]. Recently, Moiseev *et al.* [3] demonstrated that gyrotrons can retain a high efficiency when pumped with relativistic electron beams. This was experimentally confirmed in [4], where a 3-cm gyrotron with an optimized resonator profile and electron beam parameters produced an output power of up to 7 MW at an efficiency of about 50%.

Thus, the potential possibilities of gyrotrons are by no means exhausted—neither in the output radiation power level nor with respect to a competitive operating range. This statement can be also valid with respect to the possible generation regimes, in view of the possible multifrequency operation modes. However, theoretical analysis of the dynamics of gyrotrons possessing a traditional configuration of the interaction space (in the form of a weakly nonregular waveguide section matched to the output tract) shows that the bifurcation currents for which the self-modulated generation regimes become possible are higher by approximately one order of magnitude than the typical operating currents [5]. This circumstance hinders observation of such regimes using the existing gyrotron facilities. At the same time, it was previously demonstrated [6] that the values of bifurcation currents could be significantly reduced by introducing additional delayed reflections at the collector end of the interaction space. This effect was used to observe the expanded generation spectrum in weakly relativistic continuous gyrotrons [7], where additional reflections were introduced by a mismatch of the gyrotron output window.

Below we present the results of an experimental observation of the self-modulated generation regimes in a relativistic gyrotron operating in the H_{01} mode, in which a delayed feedback was provided by introducing a special narrowing in the output tract of the generator. The region of a resonance interaction between the electron beam and the H_{01} mode field had a configuration corresponding to the experimental conditions described in [4]. The reflector, spaced by $L \approx 9$ cm from a joint of the resonator opening and the output waveguide section, represented a narrowing waveguide with a circle-arc-shaped profile. For the reflector with an internal radius of $R_0 = 1.9$ cm, the power reflection coefficient in the operating frequency range was about 80%.

The electron beam energy was reduced (as compared to that employed in [4]) to 230 keV. The cathode operated in the regime of temperature-controlled emission, in which the current could be varied from 15 to 65 A. Further increase in the beam energy was limited by breakdowns in the electrodynamic system of the generator, which were probably related to the excitation of nonsymmetric modes. For such modes, the presence of tangential electric field components on the walls of the electrodynamic system could initiate a microwave discharge.

Figure 1 shows typical oscillograms of the accelerating voltage pulses and the output signals observed for various beam currents. As can be seen, the relative modulation amplitude monotonically increases with the current, to reach a maximum level of 90% at 45 A.

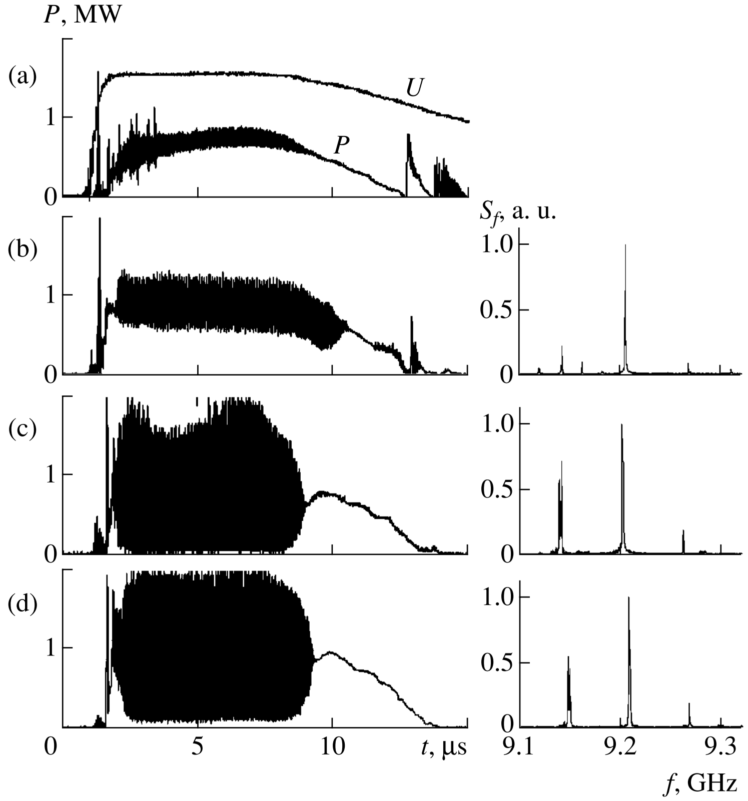

Fig. 1. Oscillograms of the accelerating voltage pulse *U* and the output signal power *P* measured for the beam currents of (a) 17, (b) 28, (c) 45, and (d) 64 A and the corresponding spectral density distributions *S*.

As the current grows, the average power increases from 0.7 to 1 MW. When the currents increases above 45 A, the output signal remains virtually unchanged: both the relative modulation amplitude and the average output power are retained on the maximum level. The efficiency of operation gradually decreases: from 15–20% at 15–20 A to 5–6% at a current on the order of 60 A. In all cases, the total duration of a self-modulated portion of the pulsed signal exceeded 6 μs, which corresponded to the length of the flat part of the accelerating voltage pulse. Figure 1 also presents the spectra of the output signal measured by a heterodyne method in the same flat part of the accelerating voltage pulse. According to the results of these spectral measurements, the self-modulation period varied within 16.6–16.9 ns. In addition, the spectral amplitude of the low-frequency satellite always exceeded that of the high-frequency component. This result is not an experimental artifact and requires additional investigation.

Nonstationary processes in the relativistic gyrotron were also studied using the PIC code KARAT, which allowed the Maxwell equations to be directly modeled in combination with the equations of motion for macroparticles involved in the process. Due to the axial symmetry of the system and the operating mode (TE_{01}), it was possible to employ a two-dimensional variant of the PIC code. The simulations were performed assuming that a 230-keV beam with a zero transverse velocity scatter was injected into the resonator. A pitch factor on the order of unity was selected based on the results of special modeling of screw beam formation in a magnetron injector gun.

Figure 2 shows the interaction space geometry and the instantaneous distribution of macroparticles in the course of modeling. Electrons initially moved in a magnetic field of the coil with a nearly homogeneous field strength distribution in the region from 0 to 30 cm.

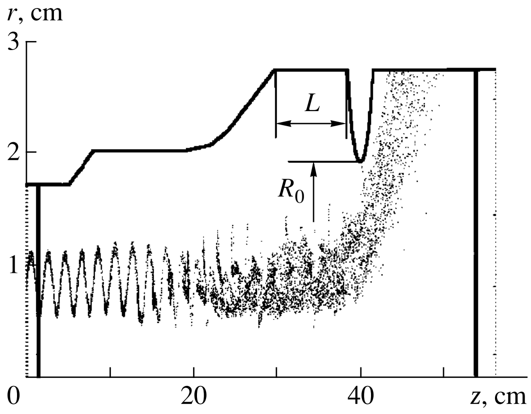

Fig. 2. Geometry of the interaction space (solid curve) and the instantaneous positions of macroparticles simulated by PIC code KARAT.

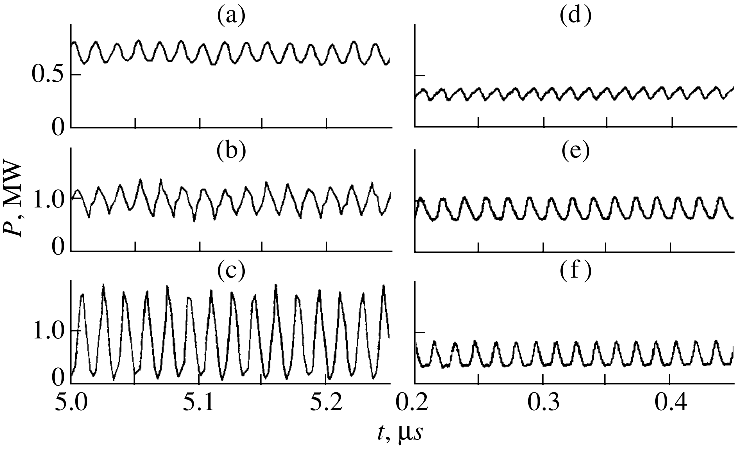

Fig. 3. A comparison of the experimental and simulated patterns of time variation of the output signal: (a–c) oscillograms measured at a beam current of 17, 28, and 45 A, respectively; (d–f) simulations obtained for the injected currents of 15, 30, and 45 A, respectively.

Then the electron beam deposited onto the waveguide wall under the action of the solenoid edge field. The magnetic field strength varied within 4.2–4.5 kOe, depending on detuning from the cyclotron resonance conditions. It should be noted that, according to the results of our simulations, electrons must strike the wall immediately behind the reflector, whereas in the experiment this took place over a distance on the order of 50 cm. Nevertheless, the results of modeling of the stationary operation regimes showed that, for a waveguide with a radius significantly exceeding a certain critical value interaction of the beam with the output radiation could be ignored because the cyclotron resonance conditions at a given frequency were essentially broken.

Figure 3 shows the patterns of time variation of instantaneous power (averaged over 1 ns) simulated for the injected electron currents of 15, 30, and 45 A in comparison to the experimental oscillograms measured at 17, 28, and 45 A. As can be seen, the simulated patterns also reveal an increase in the relative modulation amplitude with the current; the value of the modulation period agreed well with the experimental data and approximately corresponded to the time required for the corresponding perturbation to travel over the feedback chain.

According to the results of simulation, an increase in the injected current above 30 A leads to excitation of an additional H_{02} mode on the second harmonic of the cyclotron frequency. As a result, the relative amplitude of modulation drops (due to a decrease in the efficiency of interaction with the operating mode) as compared to the level observed in the experiment (where the cyclotron frequency harmonics were suppressed due to significant scatter of the transverse velocities of electrons). Allowance for the initial scatter of the transverse electron velocities in our simulations also led to suppression of the cyclotron frequency harmonics; however, this required a manifold increase in the number of particles and, hence, in the computational time. In this case, no satisfactory agreement with experiment was obtained for large beam currents.

In concluding, it should be noted that subsequent development of the experimental investigations in this direction is related to an increase in the average output power and the efficiency of the self-modulated generation regimes. In this respect, the results of simulation show that an increase in the efficiency can be provided by optimization of the coefficient of reflection from a nonregular waveguide section. Figure 4 shows plots of the average output power and the relative amplitude of modulation versus the internal radius of the reflector for a beam current of 30 A. As is seen, the power increases in proportion to the gap, while the maximum relative modulation amplitude reaches 70% for $R_0 \approx 1.95$ cm. In this case, the average output radiation power is on the order of 1 MW at an efficiency of about 15%. For the reasons indicated above, we did not simulate the gyrotron operation at large beam currents. Nevertheless, it can be expected that analogous dependences will take place for high-power beams. Provided that the spu-

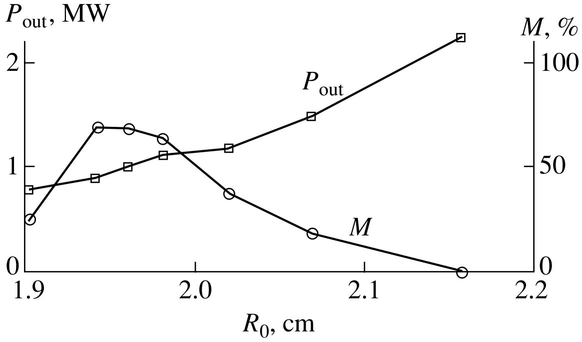

Fig. 4. Plots of the average output power P_{out} and relative modulation amplitude M versus reflector radius R_0 for a beam current of 30 A.

rious mode generation will be effectively suppressed, this would allow the experimental output power to be increased up to a level of several megawatts at an efficiency exceeding 15%.

Acknowledgments. This study was supported by the Russian Foundation for Basic Research, project no. 00-02-16412.

REFERENCES

1. N. S. Ginzburg, N. I. Zaĭtsev, E. V. Ilyakov, *et al.*, Zh. Tekh. Fiz. **71** (11), 73 (2001) [Tech. Phys. **46**, 1420 (2001)].
2. A. L. Gol’denberg, G. G. Denisov, V. E. Zapevalov, *et al.*, Izv. Vyssh. Uchebn. Zaved., Radiofiz. **39** (6), 635 (1996).
3. M. A. Moiseev, V. E. Zapevalov, and N. A. Zavolsky, Int. J. Infrared Millim. Waves **22** (6), 813 (2001).
4. N. I. Zaĭtsev, N. S. Ginzburg, E. V. Ilyakov, *et al.*, Pis’ma Zh. Tekh. Fiz. **27** (7), 8 (2001) [Tech. Phys. Lett. **27**, 266 (2001)].
5. N. S. Ginzburg, G. S. Nusinovich, and N. A. Zavolsky, Int. J. Electron. **61**, 881 (1986).
6. N. S. Ginzburg, M. Yu. Glyavin, N. A. Zavol’skiĭ, *et al.*, Pis’ma Zh. Tekh. Fiz. **24** (11), 53 (1998) [Tech. Phys. Lett. **24**, 436 (1998)].
7. M. Yu. Glyavin, V. E. Zapevalov, A. N. Kuftin, and A. G. Luchinin, Izv. Vyssh. Uchebn. Zaved., Radiofiz. **43** (5), 440 (2000).

Translated by P. Pozdeev

Technical Physics Letters, Vol. 28, No. 5, 2002, pp. 399–400. Translated from Pis'ma v Zhurnal Tekhnicheskoĭ Fiziki, Vol. 28, No. 9, 2002, pp. 92–95.
Original Russian Text Copyright © 2002 by Chekalova, Grigor'ev, Denisov.

The Friction Drag of a Turbulent Flow Reduced on the Surface with a Molecular Film of Foleox Polymer

L. A. Chekalova, V. Yu. Grigor'ev, and É. P. Denisov
Krylov Institute, St. Petersburg, Russia

Received September 21, 2001; in final form, December 18, 2001

Abstract—We have experimentally studied the possibility of reducing the friction drag of a flow over a metal surface by applying a fluorine-containing polymer (foleox) onto the surface. It is shown that the foleox coating significantly decreases the friction drag of a turbulent flow. © *2002 MAIK "Nauka/Interperiodica".*

As is known, a decrease in the drag of a fluid flowing over a surface can be provided by imparting a regular microroughness to the surface, for example, in the form of a pattern of riblets, which, however, is effective only for a certain constant flow velocity [1]. A decrease in the drag can be also reached by introducing a substance with "long" molecules, for example, of a poly(ethylene oxide) based synthetic polymer PEO-301 (polyox), but this effect is achieved only for a finite time determined by the consumed polymer stock [2, 3]. These limitations can be partly eliminated by coating a streamlined metal surfaces with a fluorine-containing polymer of the foleox type developed in various modifications at the Lebedev Institute of Synthetic Rubber (St. Petersburg).

The molecules of foleox, belonging to the class of polar–nonpolar compounds, comprise a polar "head" part capable of strong binding to a substrate material and the nonpolar "tail" containing fluorine atoms. The latter parts form a monomolecular layer possessing a flexible roughness. The presence of fluorine decreases the surface energy, which additionally reduces wetting and decreases the drag [4].

In order to evaluate the effect of foleox coatings upon the friction drag of fluids, we have studied a developed turbulent flow of water and air in a rectangular cylindrical channel with an internal diameter of 13 mm. The experimental setup allowed the water flow to be studied in a range of Reynolds numbers Re = 5×10^3–5×10^5. The air flow in the same channel was controlled within Re = 7×10^3–7×10^6.

The technology of foleox application to the internal surface of titanium tubes was as follows. First, the surface to be coated was thoroughly degreased and dried (sometimes, the tube was annealed at a high temperature). Then the tube was filled with a foleox solution in an organic solvent, from which the polymer deposited onto the tube wall. After a certain time, the solution was discharged and the tube with a coating was dried. The results of experiments were processed and presented in terms of the drag as a function of the flow velocity: $\lambda = f(\mathrm{Re})$. The experimental error with respect to the Blasius relationship $\lambda = 0.3164/\mathrm{Re}^{0.25}$ did not exceed 2%.

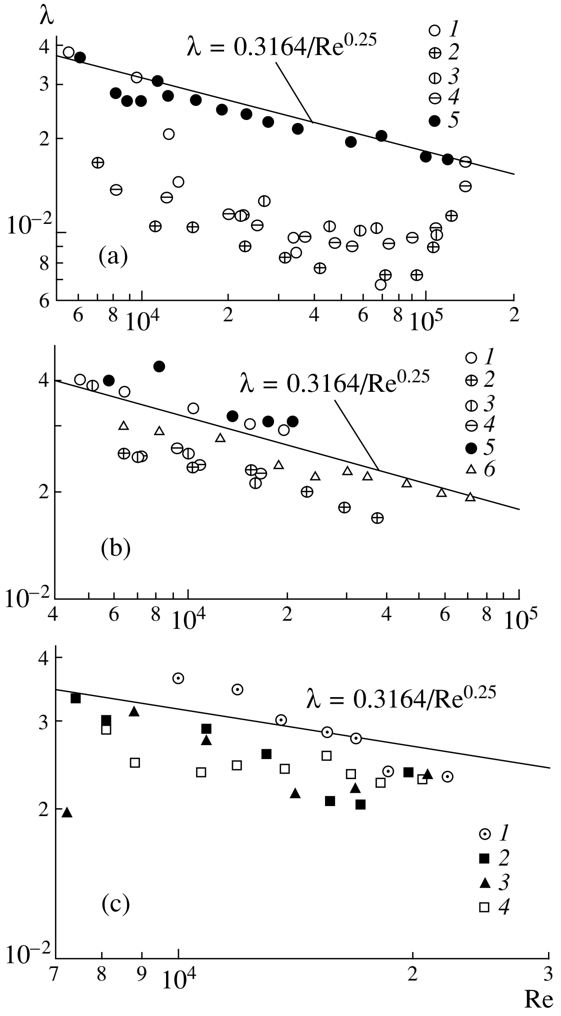

Fig. 1. Plots of the drag coefficient versus Reynolds number for fluids flowing in a foleox-coated (grade 14-1) tube in a series of sequential experiments (run numbers are indicated at the symbols): (a) water flow; (b) water flow in the same tube after 2.5-month storage; (c) air flow.

1063-7850/02/2805-0399$22.00 © 2002 MAIK "Nauka/Interperiodica"

For the experiments with water flow, a maximum (65%) decrease in the friction drag was observed in the tube with a single-layer foleox coating deposited from a 1% solution of 14-1 grade foleox (Fig. 1a). An analysis of the experimental data for this coating revealed the following results (typical of some other foleox grades as well):

(i) Initially, at a small shear stress level (the first experiment, flow rate below Re = (5–8) × 10^3), the polymer coating does not influence the flow; however, as the shear stress increases, the presence of the polymer film is manifested.

(ii) The polymer molecules begin to rotate (activation) when the shear stress reaches a certain threshold level τ (for the given coating, the threshold stress was $\tau \cong 2.5$ N/m^2); on reaching $\tau \cong 4.0$ N/m^2 for Re = 10^4, the mechanism of the polymer film action is completely operative.

(iii) When the shear stress exceeds a certain limit (in the given case, this value was $\tau \cong 100$ N/m^2 for RE = 9 × 10^4), the coating is destroyed; for the shear stresses not exceeding this fracture limit, the polymer film operates stably for a long time.

The antidrag activity of the polymer coating was rather high (≅25%) even after a storage for about 2.5 months (Fig. 1b). However, this long interruption, in addition decreasing the efficiency, reduced the critical flow velocity: the antidrag effect fully vanished at Re = 3.5×10^4 and was not restored in subsequent tests. It was established that the properties of a coated surface could be restored by redepositing foleox only upon the thorough and labor-consuming process of cleaning the metal surface from the previous polymer film.

The experiments with foleox-coated samples in an air flow showed an effect analogous to that observed for water (Fig. 1c). Moreover, the antidrag activity is retained even under conditions when the effect in water ceases.

Conclusions. (1) A monomolecular layer of foleox deposited onto a streamlined surface decreases the drag of both water and air flow over the surface, which is indicative of a common nature of this phenomenon.

(2) The fundamental possibility of significantly reducing the friction drag of a turbulent flow over a polymer-coated surface suggests that further investigations are expedient for optimization of the efficiency and stability of long polar–nonpolar molecules on the surface of various materials.

REFERENCES

1. *Viscous Flow Drag Reduction,* Ed. by G. R. Hough (American Inst. of Aeronautics and Astronautics, New York, 1980; Mashinostroenie, Moscow, 1984).
2. E. M. Khabakhpasheva and B. V. Perepelitsa, Inzh.-Fiz. Zh. **18** (6), 1094 (1970).
3. Yu. F. Ivanyuta and L. A. Chekalova, Inzh.-Fiz. Zh. **26** (5), 799 (1974).
4. É. P. Denisov, V. Yu. Grigor’ev, L. A. Chekalova, *et al.*, RF Patent No. 2073129, Byull. Izobr., No. 4 (1997).

Translated by P. Pozdeev

Technical Physics Letters, Vol. 28, No. 5, 2002, pp. 401–402. Translated from Pis’ma v Zhurnal Tekhnicheskoĭ Fiziki, Vol. 28, No. 10, 2002, pp. 1–6.
Original Russian Text Copyright © 2002 by Tchen.

The Harmonic Oscillator Equation for Ultracold Neutrons Moving in an Inhomogeneous Magnetic Field

T. Tchen
Moscow State Academy of Fine Chemical Technology, Moscow, Russia
e-mail: docent65@mtu-net.ru

Received July 16, 2001

Abstract—The motion of ultracold neutrons in a magnetic field featuring a quadratic inhomogeneity is considered. A partial solution to the stationary Schrödinger equation is found, which leads to a harmonic oscillator equation for the *X* coordinate. It is demonstrated that, under certain conditions, it is basically possible to provide for a spatial focusing of neutrons with the formation of either a single point focus or two side foci. Dependence of the focusing on the degree of monochromaticity of the neutron beam is considered. *© 2002 MAIK “Nauka/Interperiodica”.*

The focusing properties of inhomogeneous magnetic fields have been studied since the 1970s [1–3] in view of creating magnetic lenses for ultracold neutrons (UCNs). Below we will theoretically demonstrate that the possibility of spatially focusing UCNs in a magnetic field under certain conditions follows from a solution to the Schrödinger equation.

Consider the motion of UCNs under the action of gravitational and magnetic fields. The magnetic field H is assumed to be quadratically inhomogeneous in the X coordinate:

$$H = H_0 + \alpha_2 x^2, \quad \alpha_2 > 0. \tag{1}$$

The stationary Schrödinger equation for the neutron wave function $\Psi(\mathbf{r})$ will be solved by separating variables: $\Psi(\mathbf{r}) = \Psi_1(x)\Psi_2(z)$, where $\Psi_1(x) \neq 0$ and $\Psi_2(z) \neq 0$. Let us find a partial solution to the Schrödinger equation by reducing it to a system of two differential equations for the functions $\Psi_1(x)$ and $\Psi_2(z)$:

$$\begin{gathered} d^2\Psi_1/dx^2 + \{2m[mv^2/2 \pm \mu(H_0 + \alpha_2 x^2)]/\hbar^2\}\Psi_1 = 0, \\ d^2\Psi_2/dz^2 + (2m^2 gz/\hbar^2)\Psi_2 = 0. \end{gathered} \tag{2}$$

Here, m is the neutron mass, g is the acceleration of gravity, $\hbar$ is the Planck constant, v is the UCN velocity, and $\mu = 6.02 \times 10^{-8}$ eV/T is the magnetic moment of the neutron.

The first equation in system (2) reduces to an equation of the harmonic oscillator and yields the following solution:

$$\Psi_1(x) = CD_n(Ax), \quad A = (8m\mu\alpha_2/\hbar^2)^{1/4}, \tag{3}$$

where

$$n = -1/2 + (mv^2/2 - \mu H_0)/[\hbar(2\mu\alpha_2/m)^{1/2}] \tag{4}$$

and $D_n(t)$ is the Weber function (parabolic cylinder). Using the normalization condition $\int_{-\infty}^{+\infty}|\Psi_1(x)|^2 dx = 1$, we obtain the constant C for the function $\Psi_1(x)$: $C = (A/(2\pi)^{1/2}n!)^{1/2}$.

Taking $n = 0$, we obtain the wave function of UCNs polarized antiparallel to the magnetic field H:

$$\Psi_1(x) = CD_0(Ax) = C\exp(-A^2x^2/4), \tag{5}$$

which exhibits a maximum at $x = 0$. Thus, the system with $n = 0$ is characterized by a maximum density of the probability of finding neutrons on the axis. This result can be interpreted as the UCN beam focusing at $x = 0$. The size Δx of the focal spot can be evaluated as a distance over which $|\Psi_1(x)|^2$ drops by a factor of $\mathbf{e}$ relative to the maximum. With this definition, Eq. (5) yields for the focus width

$$\Delta x = 2(2)^{1/2}/A = (\hbar^2/2m\mu\alpha_2)^{1/4}. \tag{6}$$

Note that for $\hbar \longrightarrow 0$ we obtain $\Delta x \longrightarrow 0$, which indicates that the UCN focusing is a quantum-mechanical effect.

Let us numerically estimate Δx for $H_0 \approx 1.5$ T, $\Delta H = H - H_0 \approx 0.5$ T, and $d \sim 1$ mm (the transverse size of an output UCN beam determined by a particular focusing system design). In this case, $\alpha_2 \approx 4\Delta H/d^2$ and $\Delta x \sim 20$ μm. Thus, for an input UCN beam size of $D \sim 1$ cm, the output flux density is higher than the input value by 2–3 orders of magnitude.

Now let us study the influence of the degree of monochromaticity of the UCN beam on the focusing for $n = 0$. A change in the neutron velocity by ΔV leads to the following variation of the parabolic function index:

$$\Delta n = (E/\Delta E)(\Delta V/V), \tag{7}$$

where $E = mv^2/2$ and $\Delta E = E - \mu H_0$. Consider the case of $E \sim 10^{-7}$ eV and $\Delta E \sim 10^{-9}$ eV. For a supermonochro-

1063-7850/02/2805-0401$22.00 © 2002 MAIK “Nauka/Interperiodica”

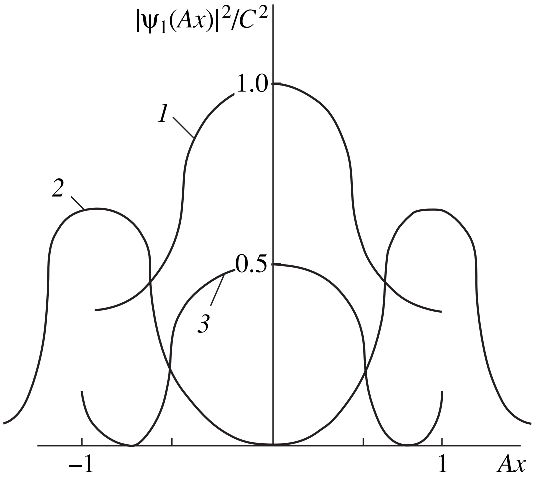

Fig. 1. Plots of the wave function amplitude versus distance illustrating the effect of monochromaticity on the UCN focusing ($E = 10^{-7}$ eV; $\Delta E = 10^{-9}$ eV): (*1*) $\Delta V/V = 10^{-3}$ (n = 0.1); (*2*) $\Delta V/V = 10^{-2}$ (n = 1); (*3*) $\Delta V/V = 2 \times 10^{-2}$ (n = 2).

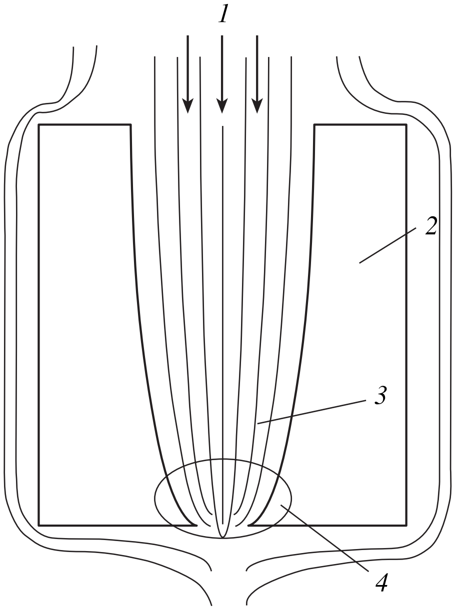

Fig. 2. A schematic diagram of the system for UCN focusing: (*1*) UCN beam; (*2*) superconductor; (*3*) magnetic field lines; (*4*) inhomogeneous magnetic field region.

matic neutron beam with $\Delta V/V \ll 10^{-2}$ (see, e.g., [4]), formula (7) implies that $\Delta n \ll 1$. Calculations show that the focusing of such neutrons is rather insignificantly affected by the degree of monochromaticity. However, for $\Delta V/V \sim 10^{-2}$ and the same relative variation of E and ΔE, the parabolic function index n is unity and the central maximum splits into two side peaks symmetric relative to $x = 0$ (Fig. 1).

For $\alpha_2 = 0$, the above solution becomes

$$\Psi_1(x) = C_1 \exp(ikx) + C_2 \exp(-ikx),$$

where

$$k = \{2m(mv^2/2 - \mu H_0)/\hbar^2\}^{1/2}.$$

This plane-wave solution implies the absence of focusing for $\alpha_2 = 0$, which is also evident from formula (6). An additional increase in the neutron flux density can be provided along the Y axis. The total increase in the output neutron flux density can reach up to 5–6 orders of magnitude.

A solution to the second equation in system (2) is offered by Airy’s function,

$$\Psi_2(z) = C\Phi(-t), \quad t = z(2m^2g/\hbar^2)^{1/3}, \qquad (8)$$

where C is a constant factor. The maximum of Airy’s function is attained for $t \approx -1.02$, that is, at the point with the coordinate $z_{\max} = -1.02/(2m^2g/\hbar^2)^{1/3} \approx -6$ μm. This fixed position of maximum on the Z axis is a restriction related to the selected form of the partial solution to the Schrödinger equation.

It should be noted that one of the most interesting practical applications of inhomogeneous magnetic fields is the Meissner effect in superconductors (Fig. 2). A transverse gradient of the magnetic field strength can be created by selecting an appropriate shape of the superconductor surface. In the case when the magnetic field strength H is below the critical value H_c breaking the superconducting state, an inhomogeneous magnetic field is generated at the output gap of the superconductor, where the magnetic field lines converge. The μH_c value can be considered as the “critical” energy for a given superconductor. Taking the UCN energy equal to this value, $E = E_c = mv_c^2/2 \approx \mu H_c$, we can determine the maximum UCN velocity for which the inhomogeneous magnetic field gradient caused by the Meissner effect would produce focusing of the UCN beam. For neutrons with velocities $V > V_c$, the dominant effect is reflection from the superconductor walls. This can be accompanied by a spatial confinement of the neutron flux at the superconductor output as a result of the total external reflection from the walls. For this purpose, the UCN energy must be lower than the effective potential of the superconductor.

REFERENCES

1. G. I. Terekhov, Pis’ma Zh. Tekh. Fiz. **3** (23), 1275 (1977) [Sov. Tech. Phys. Lett. **3**, 526 (1977)].
2. R. Golub and P. Carter, Nucl. Instrum. Methods **91**, 205 (1971).
3. A. I. Frank, Usp. Fiz. Nauk **151** (2), 229 (1987) [Sov. Phys. Usp. **30**, 110 (1987)].
4. T. Chen and R. N. Kuz’min, Pis’ma Zh. Tekh. Fiz. **17** (10), 51 (1991) [Sov. Tech. Phys. Lett. **17**, 371 (1991)].

Translated by P. Pozdeev

Technical Physics Letters, Vol. 28, No. 5, 2002, pp. 403–405. Translated from Pis’ma v Zhurnal Tekhnicheskoĭ Fiziki, Vol. 28, No. 10, 2002, pp. 7–12.
Original Russian Text Copyright © 2002 by I. Dzedolik, A. Dzedolik.

Nonlinear Modes in Optical Fibers

I. V. Dzedolik and A. I. Dzedolik
Tauric National University, Simferopol, Crimea, Ukraine
e-mail: dzedolik@crimea.edu

Received September 24, 2001; in final form, January 10, 2002

Abstract—It is shown that the electromagnetic field generated in an optical fiber operating in a nonlinear regime has the form of nonlinear guided modes—cnoidal (periodic) waves which transform into monochromatic fiber modes in the linear operating regime. The cnoidal modes are generated due to nonlinear polarization effects in the dielectric medium. These effects can be described by equations with sinusoidal nonlinearity. *© 2002 MAIK “Nauka/Interperiodica”.*

As is well known, the electromagnetic field generated by a continuous laser radiation in optical fibers operating in the linear regime propagates in the form of guided fiber modes with harmonic dependence on time and the longitudinal coordinate [1]. High-intensity continuous radiation or a pulsed operation may cause nonlinear interactions of the electromagnetic field with the medium. In most theoretical studies, this interaction is described by equations for the envelope of a plane monochromatic wave depending on the longitudinal coordinate and time [2–4]. However, in the nonlinear operating mode, the electromagnetic field can no longer be described by the linear fiber modes.

In several papers [5, 6], the dynamics of the complex envelope of the monochromatic field was studied as a function of both transverse and longitudinal coordinates and time, which satisfies the Schrödinger equation with cubic nonlinearity written for an unbounded axially symmetric medium. In this study, we attempt to find expressions for nonlinear modes in a bounded axially symmetric dielectric medium (an optical fiber) with allowance for sinusoidal nonlinearity.

Let us consider conditions for the generation of nonlinear polarization and electromagnetic waves in an optical fiber. For this purpose, we write the Maxwell equations for the electromagnetic field in a quartz fiber,

$$\nabla \times \mathbf{B} = \frac{1}{c}\frac{\partial \mathbf{D}}{\partial t}, \quad \nabla \mathbf{D} = 0,$$
$$\nabla \times \mathbf{E} = -\frac{1}{c}\frac{\partial \mathbf{B}}{\partial t}, \quad \nabla \mathbf{B} = 0, \tag{1}$$

together with the constitutive equation

$$\mathbf{D} = \mathbf{E} + 4\pi\mathbf{P}, \tag{2}$$

where $\mathbf{P} = -eN\mathbf{r}$ is the medium polarization vector. Using Eqs. (1) and (2) and taking into account that $\nabla\mathbf{E} + 4\pi\nabla\mathbf{P} = 0$, we obtain

$$\left(\nabla^2 - \frac{1}{c^2}\frac{\partial^2}{\partial t^2}\right)\mathbf{E} = -4\pi\left[\nabla(\nabla\mathbf{P}) - \frac{1}{c^2}\frac{\partial^2\mathbf{P}}{\partial t^2}\right]. \tag{3}$$

The unit cell of quartz has a center of symmetry; therefore, the potential of the crystal lattice can be approximated by an even function $U = -f_0\cos\left(\frac{2\pi}{r_0}r\right)$, where r_0 is the mean atomic radius. Let us write the equation of motion for the optical electron in an atom located at the site of the quartz crystal lattice. If the electron is acted on by the periodic force of the electric field with a frequency that lies far from the quartz absorption band, this equation can be written as

$$m\frac{d^2\mathbf{r}}{dt^2} = -\nabla U - e\mathbf{E}, \tag{4}$$

where $-\nabla U = -\mathbf{f}_0\sin\left(\frac{2\pi}{r_0}r\right)$ is the averaged restoring force of the crystal lattice. Let us multiply Eq. (4) by $-eN$ and divide it by the electron mass m. As a result, we obtain an equation for the polarization vector,

$$\frac{d^2\mathbf{P}}{dt^2} = -\mathbf{f}_m\sin(\mathbf{qP}) + \nu_e^2\mathbf{E}, \tag{5}$$

where $\mathbf{f}_m = eN\mathbf{f}_0/m$, $\mathbf{q} = \mathbf{1}(2\pi/r_0eN)$, and $\nu_e^2 = e^2N/m$. System (3)–(5) describes the nonlinear modes in an optical fiber.

Upon obtaining a solution for the electric field from (3)–(5), the magnetic field can be found from (1) as

$$\mathbf{B} = -c\nabla \times \int dt\mathbf{E}. \tag{6}$$

Let us solve system (3)–(5) in the simplest case of the TM modes in a step-index fiber [1]. Choosing the cylindrical coordinate system with the z axis coinciding with the fiber axis, we assume that $\mathbf{E} = \mathbf{1}_r E(z, t)$ and $\mathbf{P} = \mathbf{1}_r P(z, t)$. Then, taking into account that $\nabla\mathbf{P} = 0$, we obtain from (3)–(5) the system of equations

$$\begin{gathered}\left(\nabla^2 - \frac{1}{c^2}\frac{\partial^2}{\partial t^2}\right)E = \frac{4\pi}{c^2}\frac{\partial^2 P}{\partial t^2},\\ \frac{d^2 P}{dt^2} + f_m\sin(qP) = \nu_e^2 E.\end{gathered}\tag{7}$$

Assume that the field components of a uniform wave packet with a stationary profile are periodic functions of the longitudinal coordinate and time [7]: $E = E_0\exp(i\phi)$, $B = B_0\exp(i\phi)$, and $P = P_0\exp(i\phi)$, where $\phi = \omega t - \beta z$. Then the first equation of system (7) transforms to the equation

$$\left(-\beta^2 + \frac{\omega^2}{c^2}\right)E = -\frac{4\pi}{c^2}\omega^2 P,$$

from which we can express the electric field as

$$E = -\frac{4\pi\omega^2}{\omega^2 - c^2\beta^2}P.\tag{8}$$

Substituting (8) into the second equation of system (7) and replacing time t with ϕ, we obtain an equation for the polarization,

$$\frac{d^2P}{d\phi^2} + f_S\sin(qP) + a_0 P = 0,\tag{9}$$

where $f_S = f_m/\omega^2$ and $a_0 = \omega_e^2/(\omega^2 - c^2\beta^2)$. Upon integrating Eq. (9) with the initial conditions $P(\phi = 0) = 0$ and $(dP/d\phi)_0 = \xi = \text{const}$, we obtain the first integral:

$$\left(\frac{dP}{d\phi}\right)^2 = \xi^2 + \frac{2f_S}{q}[\cos(qP) - 1] - a_0 P^2.\tag{10}$$

For a low-intensity electric field, $qP \ll 1$, we can readily obtain from (10) the second integral,

$$\phi = \pm\int\frac{dP}{\sqrt{\xi^2 - (a_0 + f_S q)P^2}} = \begin{cases}\arcsin(P/b_0),\\ \arccos(P/b_0),\end{cases}$$

where $b_0 = \xi/\sqrt{a_0 + f_S q}$. As is well known, the polarization in this case is linear and can be described by harmonic functions:

$$P = \begin{cases}b_0\sin(\sqrt{a_0 + f_S q}\,\phi),\\ b_0\cos(\sqrt{a_0 + f_S q}\,\phi).\end{cases}\tag{11}$$

In order to take into account nonlinear properties of the polarization, we consider the next term in the expansion of cosine function. As a result, we obtain from (10) the following formula:

$$\phi = \pm\int\frac{dP}{\sqrt{\xi^2 - (a_0 + f_S q)P^2 + (f_S q^3/12)P^4}}.$$

This integral can be rewritten as

$$\int_0^x\frac{dx}{\sqrt{(a^2 - x^2)(b^2 - x^2)}} = \frac{1}{a}F\left(\tilde{\varphi}, \frac{b}{a}\right),$$

where $F(\tilde{\varphi}, b/a)$ is the elliptic integral of the first kind, $\tilde{\varphi} = \arcsin(x/b)$, and a and b are constants determined by the relationships $a^2b^2 = 12\xi^2/f_S q^3$ and $a^2 + b^2 = 12(a_0 + f_S q)/f_S q^3$ as

$$a^2 = \frac{\xi^2}{(a_0 + f_S q)/2 \pm \sqrt{(a_0 + f_S q)^2/4 - \xi^2}},$$

$$b^2 = \frac{6(a_0 + f_S q)}{f_S q^3} \pm \sqrt{\frac{36(a_0 + f_S q)^2}{f_S^2 q^6} - \frac{12\xi^2}{f_S q^3}}.$$

Then, upon inverting the elliptic integral, we obtain an expression for the nonlinear polarization:

$$P = \pm b\,\mathrm{sn}(a\sqrt{f_S q^3/12}\,\phi, b/a).\tag{12}$$

The expression for the electric field strength can be found by substituting (12) into (8):

$$E_r = \mp\frac{4\pi\omega^2 b}{\omega^2 - c^2\beta^2}\mathrm{sn}(a\sqrt{f_S q^3/12}\,\phi, b/a).\tag{13}$$

Upon substituting (13) into (6), we obtain an expression for the magnetic field strength of TM modes:

$$\begin{aligned}B_\varphi = -c\frac{\partial}{\partial z}\int dt E &= \mp\frac{4\pi\omega c\beta b^2}{a(\omega^2 - c^2\beta^2)}\frac{\mathrm{sn}(u)\mathrm{cn}(u)}{\sqrt{dn^2(u) + b^2/a^2 - 1}}\\ &= \mp\frac{4\pi\omega c\beta b}{\omega^2 - c^2\beta^2}\mathrm{sn}(a\sqrt{f_S q^3/12}\,\phi, b/a).\end{aligned}\tag{14}$$

In the case under study, the Poynting vector characterizing the energy flux density of the electromagnetic field in the fiber is

$$\begin{aligned}\mathbf{S} &= \frac{c}{4\pi}\mathbf{E}\times\mathbf{B} = \frac{c}{4\pi}\mathbf{1}_z E_r B_\varphi\\ &= \mathbf{1}_z\frac{4\pi\omega^3 c^2\beta b^2}{(\omega^2 - c^2\beta^2)^2}\mathrm{sn}^2(a\sqrt{f_S q^3/12}\,\phi, b/a).\end{aligned}\tag{15}$$

Thus, in the general case, the electromagnetic field propagates in the optical fiber in the form of wave packets representing a set of cnoidal (periodic) waves which degenerate into harmonic waves (linear fiber modes) only in the particular case of low-intensity field. The critical intensity of electromagnetic field at which the fiber modes become nonlinear equals $I \sim 10^{12}$ W/cm^2 [2].

REFERENCES

1. A. W. Snyder and J. D. Love, *Optical Waveguide Theory* (Chapman and Hall, London, 1983; Radio i Svyaz', Moscow, 1987).
2. S. A. Akhmanov, V. A. Vysloukh, and A. S. Chirkin, *The Optics of Femtosecond Pulses* (Nauka, Moscow, 1988).
3. M. B. Vinogradova, O. V. Rudenko, and A. P. Sukhorukov, *The Theory of Waves* (Nauka, Moscow, 1990).
4. I. O. Zolotovskiĭ and D. I. Sementsov, Pis'ma Zh. Tekh. Fiz. **27** (14), 1 (2001) [Tech. Phys. Lett. **27**, 572 (2001)].
5. D. Rosas, C. T. Law, and G. A. Swartzlander, Jr., J. Opt. Soc. Am. B **14** (11), 3054 (1997).
6. Y. S. Kivshar, A. Nepomnyashchy, V. Tikhonenko, *et al.*, Opt. Lett. **25** (2), 123 (2000).
7. G. B. Whitham, *Linear and Nonlinear Waves* (Wiley, New York, 1974; Mir, Moscow, 1977).

Translated by A. Kondrat'ev

Technical Physics Letters, Vol. 28, No. 5, 2002, pp. 406–408. Translated from Pis'ma v Zhurnal Tekhnicheskoĭ Fiziki, Vol. 28, No. 10, 2002, pp. 13–18.
Original Russian Text Copyright © 2002 by Boriskov, Velichko, Pergament, G. Stefanovich, D. Stefanovich.

The Effect of Electric Field on Metal–Insulator Phase Transition in Vanadium Dioxide

P. P. Boriskov, A. A. Velichko, A. L. Pergament, G. B. Stefanovich, and D. G. Stefanovich
Petrozavodsk State University, Petrozavodsk, Karelia, Russia
e-mail: gstef@mainpgu.karelia.ru

Received December 28, 2001

Abstract—The effect of a strong electric field on the metal–insulator phase transition in vanadium dioxide was studied. It was found that the field application to a silicon–silicon oxide–silicon nitride–vanadium dioxide ($Si–SiO_2–Si_3N_4–VO_2$) heterostructure shifts the critical temperature of this transition toward lower values under conditions when the thermal effects are minimized. Numerical modeling of the current–voltage characteristics of the vanadium dioxide-based sandwich-type switches measured at various temperatures in the range from 15 to 350 K showed that the applied electric field influences the critical concentration and temperature of the phase transition. *© 2002 MAIK "Nauka/Interperiodica".*

The phenomenon of metal–insulator phase transition (MIPT) in the oxides of transition elements offers a promising basis for creating electron devices exhibiting a sharp thresholdlike variation of the electrical and optical properties in response to some external parameters reaching critical values. Despite rather universal behavior, the systems featuring MIPT can be conditionally subdivided into two groups with respect to the initial mechanism of the ground state instability development [1]. In the first group, changes in the crystal lattice (structural phase transition) result in splitting of the electron conduction band and, hence, in transition to the insulator state. In the other group, the transition is satisfactorily described within the framework of purely electron models (such as the Mott transition). Evidently, electron MIPT is more promising for the development of devices possessing high switching rates.

Vanadium dioxide, belonging to the first group and featuring MIPT at $T_t = 68°C$ [1], is a classical object for the investigation of such phase transitions. Some investigations were devoted to the effect of electric field upon MIPT in VO_2-based planar structures [2, 3]. These experiments demonstrated that the external electric field influences the characteristics of switching or phase transition, but the effects were rather weak and could not be unambiguously interpreted in terms of MIPT. Alternative explanations were based on a mediated inverse piezoelectric transition or an additional Joule heating of the material by leak currents passing through the gate insulators.

In our opinion, the thermal effect can be excluded by studying the field effect in planar structures of the $Si–SiO_2–Si_3N_4–VO_2$ type where the carrier injection via silicon oxide into nitride can provide for the accumulation of a sufficiently large charge. Should the nitride layer be sufficiently thin, the trapped charge would create an electric field on the external side of the structure, thus acting upon the electron subsystem of VO_2.

The experiments were performed with heterostructures of two types. The samples of type I were formed on *n*-Si substrates and had silicon oxide and nitride layer thicknesses of 60 and 100 nm, respectively; in the samples of type II formed on *p*-Si substrates, the oxide and nitride layer thicknesses were 50 and 100 nm, respectively. A vanadium dioxide layer was deposited above the semiconductor structure by laser ablation of a metal vanadium target in an oxygen-containing medium. The sample preparation was completed by depositing aluminum electrodes. The sample structures were characterized by measuring the capacitance–voltage (*C*–*V*) characteristics and the conductivity jump upon MIPT in vanadium dioxide. The samples were studied in the regime of tunneling injection of carriers (electrons and holes in the samples of types I and II, respectively) and their accumulation in the nitride layer. The charge accumulation was monitored by measuring the *C*–*V* curves and was manifested by a shift of the flat-band voltage ($\Delta V_{FB} \approx 6–8$ V). Finally, the conductivity of vanadium dioxide was measured by the four-point-probe technique. No electric field effect was observed in the structures of type I, while the samples of type II exhibited a shift of the temperature dependence of the conductivity (a hysteresis curve) toward lower temperatures (Fig. 1).

Another direction in investigating the effect of strong electric fields upon MIPT in vanadium dioxide structures is based on the study of switching properties. The switching is usually interpreted by recourse to a model based on the phenomenon of Joule heating of the material up to a critical temperature, followed by a conductivity jump as a result of the transition to a metallic

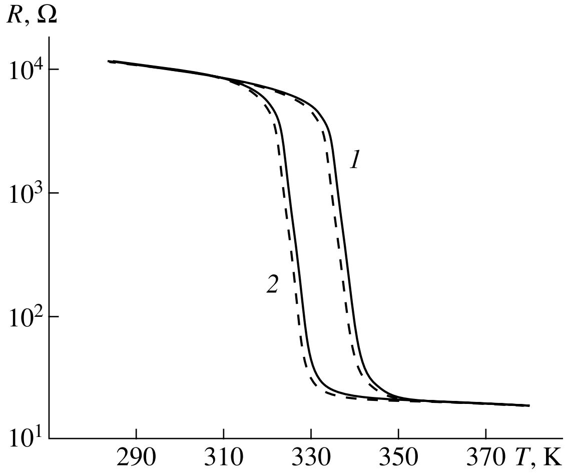

Fig. 1. The plots of resistance R versus temperature T of VO_2 (*1*) in the initial state and (*2*) upon charge accumulation.

conduction state. This is manifested by the appearance of a negative resistance (S-like) region on the I–V curve (critical temperature model [1]).

Previously [4, 5], we have demonstrated that application of a sufficiently strong electric field to an amorphous anodic vanadium film leads to the formation of a crystalline vanadium dioxide channel in the electrode, which features both MIPT and the switching effect. Using this technology for the crystalline VO_2 layer formation, it is possible to study MIPT and switching in sandwich structures under the action of electric fields with a strength of 10^5–10^6 V/cm, which is inaccessible in conventional planar switching structures.

We have studied the I–V curves of the VO_2-based sandwich structures in the temperature range from 12 to 350 K (Fig. 2). An analysis of the temperature dependence of the threshold parameters of switching showed that the process at $T \longrightarrow T_t$ agrees well with the critical temperature model. At the same time, behavior in the region of low temperatures exhibits significant deviations from the simple thermal model, which can be interpreted as the field effect upon MIPT [6]. A correct interpretation of the observed results requires more thorough consideration based on an analysis of the temperature, field strength, and electron concentration variation in the threshold region of the I–V curves. For this purpose, we have numerically modeled distributions of the temperature, field strength, and electron concentration in the conducting channel by a method based on the thermal conductivity and current continuity equations at various temperatures and applied voltages.

The results of modeling exhibited significant dependence on the channel conductivity. Within the framework of a simple thermal model, whereby the conductivity is modeled by the experimental temperature dependence irrespective of the applied field strength, no numerical solution could be found that would agree with the experimental I–V curves. This result indicates that the thermistor model of instability taking into account the presence of a positive feedback (implying an increase in conductivity upon Joule heating of the material) in the system cannot explain the experimental results. The discrepancy was especially pronounced in the low-temperature range, where the field strengths are really high.

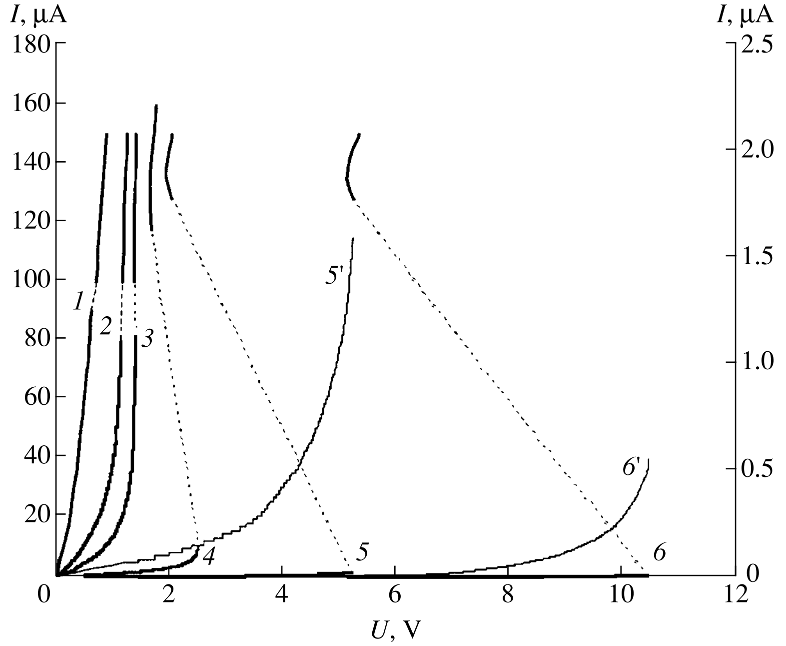

Fig. 2. Experimental current–voltage characteristics of VO_2-based switches at various temperatures (K): (*1*) 293; (*2*) 241; (*3*) 211; (*4*) 144; (*5*) 91; (*6*) 15; (*5*', *6*') low-conductivity regions of curves *5* and *6* on an extended scale, respectively (right-hand ordinate axis). Dashed lines indicate unstable (transient) regions of the I–V curves.

Assuming that the field effects can play a significant role in the subthreshold switching regime, we have studied various types of the field dependence of the conductivity. The best fit to experiment was observed for a relationship of the type $\sigma(T, E) = \sigma_0(T)f(E, T)$, where $f(E, T) = \exp\{\alpha(\sqrt{E} - \sqrt{E_p})/k_BT\}$ for $E \geq E_p$ and $f(E, T) = 1$ for $E < E_p$ (E_p is the threshold field strength at which the I–V curve begins to deviate significantly from the Ohm law, α is an empirical constant selected from the condition of best fit of experimental and theoretical I–V curves, and k_B is the Boltzmann constant). Note that similar relationships ($\sigma \sim \exp\{\alpha\sqrt{E}/k_BT\}$) are typical of various mechanisms of the carrier-concentration-related conductivity growth in a strong electric field. In our opinion, this dependence most closely corresponds to the Poole–Frenkel effect. The role of donor centers in the structures studied can belong to nonstoichiometric defects of the oxygen vacancy type.

The results of calculation of the temperature distribution in the switching channel for various I–V curve types showed that a maximum temperature at the point of switching drops with increasing field strength. Assuming that the critical temperature of MIPT is field-dependent, we may suggest that the maximum observed temperature precisely corresponds to the new temperature of transition to the metallic conduction state corresponding to a given field strength. In this case, the experimental results can be explained in terms of the critical temperature model with an allowance for a nonuniform temperature distribution in the channel and for the $T_t(E)$ relationship.

The effect of nonequilibrium charge carriers on MIPT is usually interpreted in terms of the Mott transition [1]. This model stipulates that attaining a certain critical concentration n_c is a necessary condition for the transition (taking into account data from [7], $n_c \sim 10^{18}$–10^{19} cm^{-3} for VO$_2$). Based on the numerical model employed, we have estimated the maximum concentration of conduction electrons in the channel at the instant of switching (using a virtually temperature-independent value of the electron mobility ~1 cm^2/(V s) in crystalline vanadium dioxide [1]). It was established that $n \approx n_c$ at $T_0 \geq 200$ K, whereas the concentration of electrons at low temperatures is smaller than n_c by one to two orders of magnitude.

Thus, adequate explanation of the mechanism of switching observed in the region of low temperatures and high electric field strengths requires, in addition to the field-induced increase in the carrier concentration (the Poole–Frenkel effect), an additional mechanism stipulating, probably, a direct influence of the field on the energy spectrum of the electron subsystem and, eventually, on the MIPT temperature.

The above data demonstrate the possible influence of the electric field on MIPT in various experimental situations. These results show that thin-film vanadium dioxide-based structures can be potential elements for high-rate switching devices of micro- and optoelectronics. Note that the measured switching time in the structures studied did not exceed 10^{-10} s.

REFERENCES

1. A. A. Bugaev, B. P. Zakharchenya, and F. A. Chudnovskii, *Metal–Semiconductor Phase Transition and Its Application* (Nauka, Leningrad, 1979).
2. V. V. Mokrousov and V. N. Kornetov, Fiz. Tverd. Tela (Leningrad) **16** (10), 3106 (1974) [Sov. Phys. Solid State **16**, 2005 (1974)].
3. G. P. Vasil'ev, I. A. Serbinov, and L. A. Ryabova, Pis'ma Zh. Tekh. Fiz. **3** (8), 342 (1977) [Sov. Tech. Phys. Lett. **3**, 139 (1977)].
4. F. A. Chudnovskii and G. B. Stefanovich, J. Solid State Chem. **98**, 137 (1992).
5. A. L. Pergament and G. B. Stefanovich, Thin Solid Films **322**, 33 (1998).
6. A. L. Pergament, G. B. Stefanovich, and F. A. Chudnovskii, Pis'ma Zh. Tekh. Fiz. **19** (20), 69 (1993) [Tech. Phys. Lett. **19**, 663 (1993)].
7. A. Mansing, R. Singh, and M. Sayer, Phys. Status Solidi A **49**, 773 (1978).

Translated by P. Pozdeev

Technical Physics Letters, Vol. 28, No. 5, 2002, pp. 409–410. Translated from Pis'ma v Zhurnal Tekhnicheskoĭ Fiziki, Vol. 28, No. 10, 2002, pp. 19–23.
Original Russian Text Copyright © 2002 by Levin, Semenov, Ostapenko.

Photovoltaic Converters Based on $Cd_xZn_{1-x}S/Cu_2S$ Variband Heterostructures

M. N. Levin, V. N. Semenov, and O. V. Ostapenko
Voronezh State University, Voronezh, Russia
e-mail: levin@lev.vsu.ru

Received January 18, 2002

Abstract—A new design of photovoltaic cells for ground solar energy converters based on $Cd_xZn_{1-x}S/Cu_2S$ heterostructures is proposed. A technology for fabricating the variband heterostructures is developed, which employs pyrolysis of aerosols of aqueous solutions of metal thiocarbamide complexes. © *2002 MAIK "Nauka/Interperiodica".*

At present, the problems of system design and materials selection for thin-film photovoltaic solar energy converters are considered generally solved. However, the large-scale production of such converters possessing optimum combination of cost, efficiency, and reliability is hindered by the lack of appropriate technologies.

This study is devoted to development of a technology for the fabrication of $SnO_2/Cd_xZn_{1-x}S/Cu_2S$ heterostructures for thin-film photovoltaic converters. The technological process employs pyrolysis of the aerosols of aqueous solutions of thiocarbamide complexes of the corresponding metals.

Figure 1 shows the energy band diagram of a three-layer $SnO_2/Cd_xZn_{1-x}S/Cu_2S$ heterostructure. Thick lines refer to the diagram constructed by the data reported in [1, 2]. Thin lines indicate the limits of modification of the base diagram related to variation of the regime of the Cu_2S layer formation or upon substitution of a $Cd_xZn_{1-x}S$ layer for CdS.

Using the proposed technology, it is possible to grow $Cd_xZn_{1-x}S$ layers with composition varying in depth, thus creating variband structures with a pulling field across the entire barrier layer thickness. Expansion of the region of separation of the light-induced electron–hole pairs increases the photoresponse and converter efficiency. In addition, the variband layer formation leads to an increase in the solar radiation spectrum absorbed in the converter, thus also contributing to converter efficiency.

The converter heterostructure is obtained by sequentially depositing SnO_2, $Cd_xZn_{1-x}S$, and Cu_2S layers onto quartz glass substrates. The Cu_2S film is electrochemically coated with copper and zinc layers so as to provide for an ohmic contact with low-resistivity copper sulfide. Technological requirements on the SnO_2 film are determined by the need for combining high optical transparency and high conductivity of the electron type. The electron work function for the n^+-SnO_2 layer must be not lower than that of the adjacent n-$Cd_xZn_{1-x}S$ layer in order to avoid the appearance of a barrier for collected electrons.

The longwave (red) part of the spectrum is absorbed in the narrow-gap Cu_2S layer of the p^+-Cu_2S–n-$Cd_xZn_{1-x}S$ heterojunction. The main requirement on the Cu_2S layer consists in a composition stoichiometry that provides for a high potential barrier at the boundary with the $Cd_xZn_{1-x}S$ layer and a high open-circuit voltage in combination with low serial resistance of the photovoltaic converter cell. All layers in the heterostructure under consideration transmit the infrared part of the solar spectrum. Reaching the metal layer coating the Cu_2S film, this radiation is partly absorbed in the metal and partly reflected out of the heterostructure.

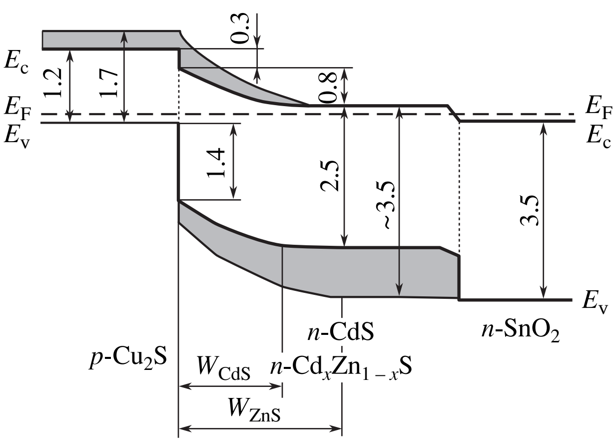

Fig. 1. The energy band diagram of a three-layer $SnO_2/Cd_xZn_{1-x}S/Cu_2S$ heterostructure: E_c, conduction band bottom; E_v, valence band top; E_F, Fermi level; W, space-charge region width (all energies indicated in electronvolts).

1063-7850/02/2805-0409$22.00 © 2002 MAIK "Nauka/Interperiodica"

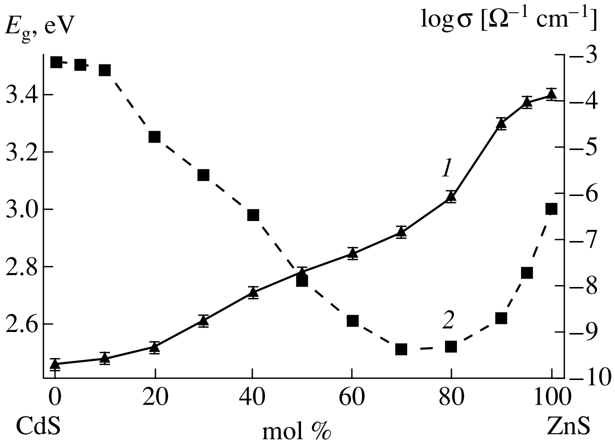

Fig. 2. Plots of the (*1*) optical bandgap and (*2*) conductivity versus composition for the films of a quasibinary CdS–ZnS system.

Fabrication of the $Cu_2S/Cd_xZn_{1-x}S$ rear-barrier photovoltaic converter cell begins with deposition of a transparent conducting SnO_2 layer on a chemically clean quartz substrate. This film is obtained by pyrolysis (T ~ 700–750 K) of a $SnCl_4$ solution containing additives of copper, antimony, or manganese salts. The SnO_2 layer resistance amounts to 5–10 Ω/cm^2; the film must possess a transmission coefficient of not less than 90% in the entire visible range of the solar radiation spectrum.

The SnO_2 layer is followed by a $Cd_xZn_{1-x}S$ film with a thickness of 3–4 μm, which is obtained by spraying an aqueous solution of $CdCl_2$, $ZnCl_2$, and $(NH_2)_2CS$ components mixed in a certain proportion. The substrate temperature is maintained at 600–680 K. It was established that a reaction between components in the aqueous solution leads to the formation of thiocarbamide complexes $[Cd(N_2H_4CS)_2Cl_2]$ and $[Zn(N_2H_4CS)_2Cl_2]$, the pyrolytic decomposition of which results in deposition of a metal sulfide layer on the substrate. The deposits are characterized by a high adhesion to substrates.

The Cu_2S layer is deposited by spraying a solution of copper chloride and thiourea (taken in a molar ratio of 1 : 3) onto the substrate at a temperature of 550 K. In this case, a coordination compound with the composition $[Cu(N_2H_4CS)_3Cl]$ is formed in the solution, the pyrolytic decomposition of which results in deposition of a layer with a composition closest to stoichiometric Cu_2S [3]. The optical bandgap of such Cu_2S layers was ~1.7 eV.

The optical properties of the films representing a quasibinary system CdS–ZnS vary smoothly with the composition. Figure 2 shows variation of the optical bandgap and the conductivity of such films on the passage from pure CdS to pure ZnS. Note that the behavior of both characteristics deviates from linear. An increase in the bandgap with the Zn content is accompanied by a growth in the open-circuit voltage U_{oc} of the photovoltaic converter based on the $Cu_2S–Cd_xZn_{1-x}S$ heterojunction, while the short-circuit current I_{sc} tends to decrease. The plot of conductivity versus composition exhibits a minimum corresponding to the composition $Cd_{0.2}Zn_{0.8}S$, which can be explained by an increase in the concentration of defects involved in the scattering of charge carriers. According to [4], the films grown in the CdS–ZnS system are characterized by a wurtzite structure in the interval of ZnS concentrations from 0 to 70 mol %, which transforms into a sphalerite structure above 70 mol % ZnS. A combination of these data is evidence for the formation of a continuous series of solid solutions in the CdS–ZnS system, which allows $Cd_xZn_{1-x}S$ layers to be obtained with the composition varying in depth, thus creating variband structures with a pulling field across the entire barrier layer thickness.

The photovoltaic conversion efficiency was evaluated as the product $U_{oc}I_{sc}$ determined for the heterostructures illuminated by radiation of a globar modeling the solar spectrum with a total radiation power of ~100 mW/cm^2. In the best samples, the open-circuit voltage and the short-circuit current density were U_{oc} = 450 mV and I_{sc} = 15 mA/cm^2, respectively. For these U_{oc} and I_{sc} values, the estimated photovoltaic converter efficiency amounts to ~7%.

The above results show advantages of the proposed technology of obtaining $SnO_2/Cd_xZn_{1-x}S/Cu_2S$ heterostructures by pyrolysis of the aqueous solutions of thiocarbamide complexes of the corresponding metals. This technology can be employed for the fabrication of thin-film photovoltaic solar energy converters for ground applications, providing for an acceptable combination of efficiency and cost.

REFERENCES

1. K. L. Chopra and S. R. Das, *Thin Film Solar Cells* (Plenum, New York, 1983; Mir, Moscow, 1986).
2. M. Savelli and J. Bougnot, Top. Appl. Phys. **31**, 213 (1979).
3. V. N. Semenov and A. V. Naumov, Zh. Neorg. Khim. **46** (3), 427 (2001).
4. V. N. Semenov, E. M. Averbakh, and Ya. A. Ugaĭ, Izv. Akad. Nauk SSSR, Neorg. Mater. **26** (10), 2030 (1990).

Translated by P. Pozdeev

Technical Physics Letters, Vol. 28, No. 5, 2002, pp. 411–413. Translated from Pis'ma v Zhurnal Tekhnicheskoĭ Fiziki, Vol. 28, No. 10, 2002, pp. 24–29.
Original Russian Text Copyright © 2002 by Yalamov, Lebedeva.

On the Oscillatory Motion of Aerosol Particles

Yu. I. Yalamov and A. L. Lebedeva
Moscow State Pedagogical University, Moscow, Russia

Received December 24, 2001

Abstract—The oscillatory motion of moderately large, spherical, solid aerosol particles occurring in a binary gas mixture under the action of a periodic external force is considered. The system is described within the framework of a mathematical and physical approach developed by Landau and Fuks [1, 2] for a generalized problem considered with an allowance for the isothermal sliding. This effect arises when the medium features a mass-average velocity gradient. Estimates show that the influence of isothermal sliding on the character of oscillations of moderately large aerosol particles depends on the frequency and can reach up to 20% of the total velocity. *© 2002 MAIK “Nauka/Interperiodica”.*

Consider a spherical particle of radius R performing translational oscillatory motion at a circular frequency ω according to the law $U = U_{\mathrm{m}}\cos(\omega t + \alpha)$, where U is the linear velocity of the particle. The function U is conveniently presented as the real part of a complex expression $U = \mathrm{Re}\{U_0\exp(-i\omega t)\}$ with a complex amplitude $U_0 = U_{\mathrm{m}}\exp(-i\alpha)$, where the constant U_0 can always be made real by properly selecting the initial time instant. Below we will omit the sign of taking the real part and perform all transformations as if U would be real, after which the real part can be taken from the final expression. Thus, we consider the motion of a spherical particle with the velocity

$$U = U_0\exp(-i\omega t) \tag{1}$$

in an external medium characterized by the density ρ and the viscosity η. Since the aerosol particle (a droplet) has a spherical shape, it is convenient to perform calculations in a spherical coordinate system (r, θ, φ). The origin of the coordinate system is placed at the point where the particle center occurs at the given time instant, and the polar axis is oriented in the direction of oscillations.

The distribution of velocities and pressure in the medium satisfies a system of linear differential equations

$$\frac{\partial \mathbf{V}}{\partial t} = -\frac{1}{\rho}\operatorname{grad} p + \frac{\eta}{\rho}\Delta\mathbf{V}, \tag{2}$$

$$\operatorname{div}\mathbf{V} = 0, \tag{3}$$

where p is the pressure and $\mathbf{V}$ is the velocity of the medium. Using a mathematical formalism developed in [1], we obtain a general expression for the velocity of oscillatory motion of the spherical particle:

$$\begin{aligned}\mathbf{V} = a\exp(ikr)\Bigg(\mathbf{U}\left(\frac{1}{r^2} - \frac{1}{ikr^3} - \frac{ik}{r}\right) \\ + (\mathbf{U},\mathbf{n})\mathbf{n}\left(\frac{ik}{r} - \frac{3}{r^2} + \frac{3}{ikr^3}\right)\Bigg) + \frac{b}{r^3}(\mathbf{U} - 3(\mathbf{U},\mathbf{n})\mathbf{n}),\end{aligned} \tag{4}$$

where $\mathbf{n} = \mathbf{r}/r$ is the unit vector in the direction of radius-vector $\mathbf{r}$. In the spherical coordinates, the velocity components have the form

$$V_r = U\cos\theta\left(a\exp(ikr)\left(-\frac{2}{r^2} + \frac{2}{ikr^3}\right) - \frac{2b}{r^3}\right), \tag{5}$$

$$V_\theta = -U\sin\theta\left(a\exp(ikr)\left(\frac{1}{r^2} - \frac{1}{ikr^3} - \frac{ik}{r}\right) + \frac{b}{r^3}\right). \tag{6}$$

The constant coefficients a and b in the above equations can be determined from the boundary conditions on the particle surface [3]:

$$V_r\big|_{r=R} = U\cos\theta, \tag{7}$$

$$V_\theta\big|_{r=R} = -U\sin\theta + C_{\mathrm{m}}\lambda\left(r\frac{\partial}{\partial r}\left(\frac{V_\theta}{r}\right) + \frac{1}{r}\frac{\partial V_r}{\partial\theta}\right). \tag{8}$$

In expression (8), the term with the coefficient C_{m} describes the isothermal sliding [4, 5] and λ is the mean free path of molecules in the external medium.

Using Eqs. (5)–(8), we obtain

$$a = -\frac{3R}{ik}\exp(ikR)C'_{\mathrm{m}}, \tag{9}$$

$$b = -\frac{R^3}{2}\left(1 - \left(\frac{3}{ikR} + \frac{3}{k^2R^2}\right)C'_{\mathrm{m}}\right), \tag{10}$$

1063-7850/02/2805-0411$22.00 © 2002 MAIK “Nauka/Interperiodica”

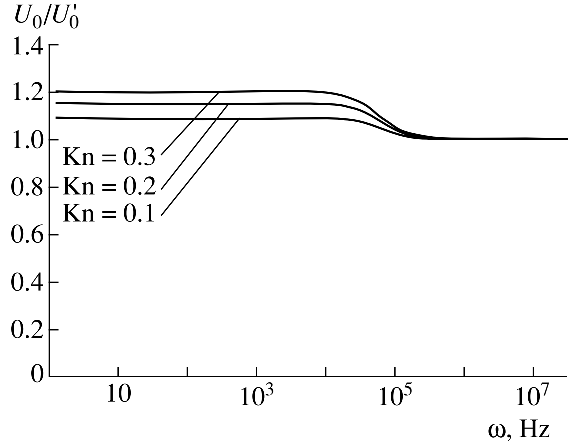

Fig. 1. The plots of U_0/U_0' versus frequency ω for a particle with $R = 1$ μm, showing the effect of isothermal sliding at various Knudsen numbers.

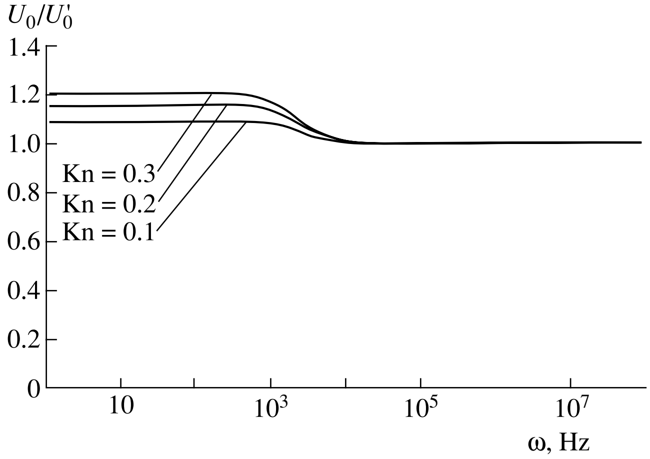

Fig. 2. The plots of U_0/U_0' versus frequency ω for a particle with $R = 5$ μm.

where the coefficient C_m' is expressed by the formula

$$C_\mathrm{m}' = \frac{(1 + 2C_\mathrm{m}\mathrm{Kn})\exp(i\varphi)}{\sqrt{\left(1 + 3C_\mathrm{m}\mathrm{Kn} + C_\mathrm{m}\mathrm{Kn}\frac{R}{\delta}\right)^2 + \left(C_\mathrm{m}\mathrm{Kn}\frac{R}{\delta}\right)^2}}. \quad (11)$$

Here, Kn = λ/R is the Knudsen number and φ is the phase shift determined from the relations

$$\cos\varphi = \frac{1 + 3C_\mathrm{m}\mathrm{Kn} + C_\mathrm{m}\mathrm{Kn}\frac{R}{\delta}}{\sqrt{\left(1 + 3C_\mathrm{m}\mathrm{Kn} + C_\mathrm{m}\mathrm{Kn}\frac{R}{\delta}\right)^2 + \left(C_\mathrm{m}\mathrm{Kn}\frac{R}{\delta}\right)^2}}, \quad (12)$$

$$\sin\varphi = -\frac{C_\mathrm{m}\mathrm{Kn}\frac{R}{\delta}}{\sqrt{\left(1 + 3C_\mathrm{m}\mathrm{Kn} + C_\mathrm{m}\mathrm{Kn}\frac{R}{\delta}\right)^2 + \left(C_\mathrm{m}\mathrm{Kn}\frac{R}{\delta}\right)^2}}. \quad (13)$$

By the same token, we obtain an expression for the pressure distribution around the oscillating particle:

$$p = p_0 + \eta U\cos\theta\frac{k^2}{r^2}b. \quad (14)$$

Using the above formulas, we can calculate the force of pressure produced by a flowing medium upon the oscillating particle. The total force F acting upon the spherical particle is

$$F = \int(-p\cos\theta + \sigma_{rr}\cos\theta - \sigma_{r\theta}\sin\theta)|_{r=R}df, \quad (15)$$

where

$$df = \int_0^{2\pi} R^2\sin\theta d\theta d\varphi = 2\pi R^2\sin\theta d\theta.$$

The components of viscous stress tensors σ_{rr} and $\sigma_{r\theta}$ are given by the expressions

$$\begin{aligned}\sigma_{rr} &= 2\eta\frac{\partial V_r}{\partial r} \\ &= 2\eta U\cos\theta\left(a\exp(ikr)\left(-\frac{2ik}{r^2} + \frac{6}{r^3} - \frac{6}{ikr^4}\right) + \frac{6b}{r^4}\right),\end{aligned} \quad (16)$$

$$\begin{aligned}\sigma_{r\theta} &= \eta\left(\frac{1}{r}\frac{\partial V_r}{\partial\theta} + \frac{\partial V_\theta}{\partial r} - \frac{V_\theta}{r}\right) \\ &= -\eta U\sin\theta\left(a\exp(ikr)\left(\frac{3ik}{r^2} - \frac{6}{r^3} + \frac{6}{ikr^4} + \frac{k^2}{r}\right) - \frac{6b}{r^4}\right).\end{aligned} \quad (17)$$

Using these formulas, we eventually obtain for the force

$$\begin{aligned}F &= 6\pi\eta R\left(1 + \frac{R}{\delta}\right)C_\mathrm{m}'U \\ &+ 3\pi R^2\sqrt{\frac{2\eta\rho}{\omega}}\left(C_\mathrm{m}' + \frac{2}{9}\frac{R}{\delta}\right)\frac{dU}{dt}.\end{aligned} \quad (18)$$

Equation (18) shows that an allowance for the isothermal sliding leads to the phase shift φ between the velocity of the oscillating particle and the drag force. Note also that the force varies with time.

We have used expression (18) to refine the formula describing the velocity of oscillatory motion of an aerosol particle under the action of a periodic external force [2]. The final expression for the velocity amplitude is as follows:

$$U_0 = \frac{F_0 f}{\omega m C_\mathrm{m}'\sqrt{\frac{f^2}{C_\mathrm{m}'^2} + 3\beta\frac{f}{C_\mathrm{m}'} + \frac{9}{2}\beta^2 + \frac{9}{2}\beta^3 + \frac{9}{4}\beta^4}}, \quad (19)$$

where F_0 is the external force amplitude, m is the particle mass, f and β are constant coefficients given by the formulas

$$f = \frac{2\rho_i}{3\rho}; \quad \beta = \frac{1}{R}\sqrt{\frac{2\eta}{\omega\rho}}, \tag{20}$$

and ρ_i is the particle density.

Denoting by U_0' the velocity amplitude of the oscillating particle in the case of $C_\mathrm{m}' = 1$, we can express the ratio U_0/U_0' as a function of the oscillation frequency. Figures 1 and 2 show this ratio for water droplets of different size in air under normal conditions. At a frequency not exceeding $\approx 10^4$ Hz, the isothermal sliding significantly influences the velocity of oscillating particles, which increases by 15–20% (depending on the Knudsen number). At higher frequencies, this effect can be ignored.

REFERENCES

1. L. D. Landau and E. M. Lifshitz, *Course of Theoretical Physics*, Vol. 6: *Fluid Mechanics* (Nauka, Moscow, 1988; Pergamon, New York, 1987).
2. N. A. Fuks, *Mechanics of Aerosols* (Akad. Nauk SSSR, Moscow, 1955; Pergamon, Oxford, 1964).
3. Yu. G. Yalamov and V. S. Galoyan, *Dynamics of Drops in Inhomogeneous Viscous Media* (Yerevan, 1985).
4. Yu. I. Yalamov and M. N. Gaĭdukov, in *Abstracts of Reports of the 4th All-Union Conference on Dynamics of Rarefied Gas, Moscow, 1975*, p. 32.
5. Yu. I. Yalamov, M. N. Gaĭdukov, and A. A. Yushkanov, Inzh.-Fiz. Zh. **9** (3), 489 (1975).

Translated by P. Pozdeev

Technical Physics Letters, Vol. 28, No. 5, 2002, pp. 414–415. Translated from Pis'ma v Zhurnal Tekhnicheskoĭ Fiziki, Vol. 28, No. 10, 2002, pp. 30–34.
Original Russian Text Copyright © 2002 by Shuman, Ratnikov, Savkina.

Effects of Substrate Doping on the Properties of Porous Silicon Carbide Layers

V. B. Shuman, V. V. Ratnikov, and N. S. Savkina
Ioffe Physicotechnical Institute, Russian Academy of Sciences, St. Petersburg, 194021 Russia
e-mail: nata.sav@pop.ioffe.rssi.ru

Received December 14, 2001

Abstract—Effects of the (n)6H-SiC substrate doping in the interval from 4×10^{17} to 4.2×10^{18} cm^{-3} on the properties of porous silicon carbide layers (pore diameter, relative porosity, pore concentration) were studied for samples prepared by the Lely method. It is established that porous SiC layers obtained by this method in strongly doped substrates are characterized by smaller pore diameter and volume and several times greater pore concentration as compared to analogous values for slightly doped substrates. *© 2002 MAIK "Nauka/Interperiodica".*

Among porous semiconductors, silicon has been the most extensively studied with respect to relationships between parameters of the porous layers, etching regimes, and initial material characteristics [1, 2]. Analogous investigations of porous silicon carbide (por-SiC) began more recently [3] and almost no data on such relationships have been reported until now. The study of the properties of por-SiC and determination of the general laws of porous layer formation is complicated by the fact that SiC usually contains a much greater number of structural defects than silicon. The presence of defects (dislocations, grain boundaries, blocks, etc.) significantly influences the properties of porous layers. For example, the porous layers obtained on the substrates prepared by a modified Lely method [4] were characterized by an average pore diameter of 20 nm, while the diameter of pores in a more defective substrate etched in the same regime [5] was as large as 110 nm. However, both investigations showed an increase in the pore diameter with current density.

The purpose of this study was to establish a relationship between characteristics of the por-SiC layer and the doping level of the initial material. Taking into account the aforementioned role of defectiveness of the initial material, we employed only SiC crystals grown by the Lely method, which are assumed to be less defective as compared to those obtained using the modified technique.

The experiments were performed with 15 polished n-SiC substrates doped with nitrogen in a broad concentration range. The concentration of uncompensated impurity (Nd–Na) was determined by measuring the optical absorption at $\lambda = 630$ nm. According to [6], the photon absorption cross section at this wavelength can be estimated at $\sigma = (5.32 \pm 0.5) \times 10^{-18}$ cm^2. The impurity concentration determined by this method was within 4×10^{17}–4.2×10^{18} cm^{-3}. After forming an ohmic contact on the C face, a por-SiC layer was formed on the Si face by electrochemical etching in an HF–H_2O–C_2H_5OH (1 : 1 : 2) mixture. The etching process was performed under UV illumination for 15 min at a current density of 20 mA/cm^2. The porous layer thickness on most samples was determined using a scanning electron microscope and the relative porosity was evaluated gravimetrically. The average pore diameter was determined from X-ray diffraction data [4]. In contrast to a method based on the low-temperature gas adsorption isotherms which provides data on the pore size distribution in each substrate [2], the X-ray technique gives only the average pore diameter; however, this method is more rapid and does not contaminate the samples.

The X-ray diffraction measurements were performed on a double-crystal diffractometer using Cu$K_{\alpha 1}$ radiation. The structural perfection of por-SiC layers was evaluated by the full angular width of the diffraction curve at half-maximum (FWHM) for the (0006) symmetric Bragg's reflection. The X-ray rocking curves of all samples with por-SiC layers on single crystal SiC substrates exhibit the same shape, comprising a narrow peak on a broad diffuse background. According to [7], this broad low-intensity background of the rocking curve is connected with the diffuse scattering from the porous structure; therefore, the diffuse spectrum width ω_{ds} can be used to calculate the effective pore diameter. As is known, the pores in SiC form either a zigzag pattern or a chain of tetrahedra [3, 4]. Nevertheless, the results of X-ray diffraction measurements can be expressed in terms of the "effective" pore diameter, assuming that the pores possess a cylindrical shape and emerge on the surface so as to form a square grid. Correctness of this approach was confirmed by data reported in [4], where the d_{ef} values calculated from ω_{ds} showed satisfactory agreement with the data

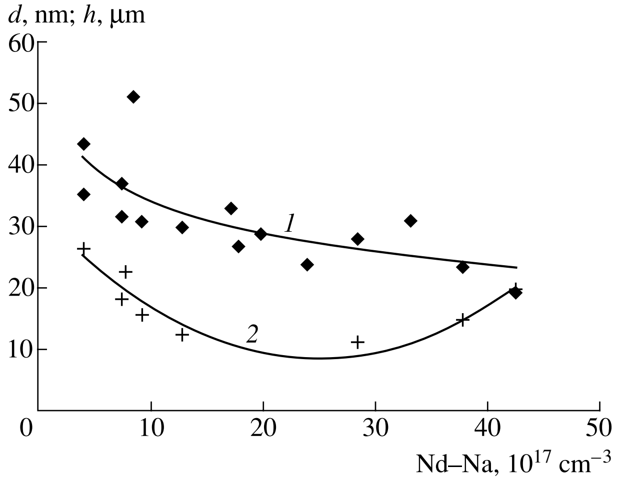

Fig. 1. Plots of the (*1*) effective pore diameter d_{ef} and (*2*) thickness h of the por-SiC layer versus substrate doping level (Nd–Na) for the samples etched for 15 min at a current density of 20 mA/cm^2.

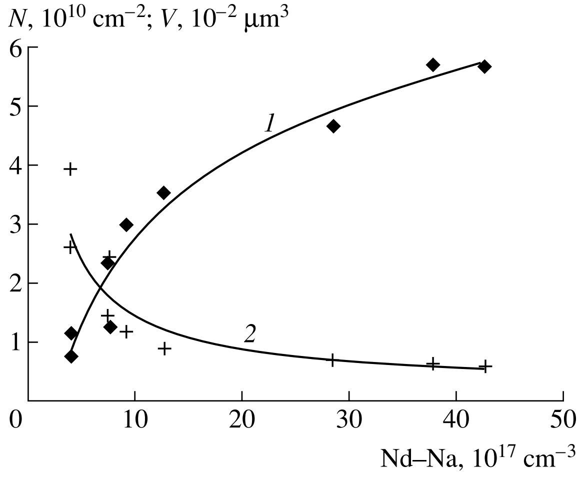

Fig. 2. Plots of the (*1*) surface concentration N of pores and (*2*) average pore volume V in the por-SiC layer versus substrate doping level (Nd–Na) for the samples etched for 15 min at a current density of 20 mA/cm^2.

of scanning electron microscopy. The plots of d_{ef} and por-SiC layer thickness versus substrate doping level are presented in Fig. 1.

Once the porous layer thickness h, the relative porosity, and the d_{ef} value are known, one can readily estimate the average pore volume and the number of pores per square centimeter (surface concentration) of the por-SiC sample. Since the por-SiC layers in all samples were formed in the same regime, the weight (and, hence, volume) of the material removed by etching (per unit surface area) was also the same (~1 mg/cm^2). Therefore, the results can only vary depending on the doping level and defectiveness of the (otherwise identical) substrates.

As can be seen from Fig. 1, a tenfold increase in the doping level leads to a decrease in d_{ef} by approximately half. The h value passes through a minimum. Accordingly, the relative porosity (proportional to h^{-1}) varies between 11.5 and 28% and exhibits a maximum. As the doping level grows, the average pore volume decreases (Fig. 2) by a factor of approximately six, while the pore concentration accordingly increases to the same extent. Thus, an increase in the uncompensated impurity concentration leads to the formation of a significantly greater number of pores possessing a smaller diameter, at a comparatively small variation in the relative porosity. The scatter of data observed is probably related to inhomogeneous doping and the presence of structural defects.

The dependence of d_{ef} on the etching current density was studied for several samples and for por-SiC areas formed in various regions of the same initial crystal. An increase in the current density is accompanied by a weak increase in the average pore diameter and by an increase in the growth rate of the porous layer, as was previously reported for 6H-SiC grown by the modified Lely method [4].

It is interesting to compare the results obtained to the behavior of porous silicon (por-Si) [1, 2]. In silicon, the average pore diameter and the growth rate of the porous layer also increase with the current density, but the relative porosity exhibits a minimum (rather than a maximum as in por-SiC) at a dopant concentration of [Nd] ~ 10^{16}–10^{17} cm^{-3}. For the same etching regime, the average pore diameter in por-Si is several times smaller than that in por-SiC, while the relative porosity is significantly higher in silicon than in silicon carbide. From this we may conclude that the behavior observed in one of these porous semiconductors cannot be automatically extended to the other. The properties of por-SiC require further thorough investigation.

Acknowledgments. This study was supported by the Russian Foundation for Basic Research, project nos. 01-02-17907, 00-02-16760, and 01-02-17657.

REFERENCES

1. V. Arita and Y. Sunohara, J. Electrochem. Soc. **124** (2), 285 (1977).
2. R. Herino, C. Bomchil, C. Barla, *et al.*, J. Electrochem. Soc. **134** (8), 1994 (1987).
3. J. S. Shor, J. Grimberg, B. Weiss, *et al.*, Appl. Phys. Lett. **62** (22), 2836 (1993).
4. N. S. Savkina, V. V. Ratnikov, and V. B. Shuman, Fiz. Tekh. Poluprovodn. (St. Petersburg) **35** (2), 159 (2001) [Semiconductors **35**, 153 (2001)].
5. N. S. Savkina, L. M. Sorokin, J. L. Hutchison, *et al.*, Appl. Surf. Sci. (2002) (in press).
6. E. I. Radovanova, Author's Abstract of Candidate's Dissertation (Fiz.-Tekh. Inst. im. A. F. Ioffe Akad. Nauk SSSR, Leningrad, 1973).
7. D. Bellet, G. Dolino, M. Lideon, *et al.*, J. Appl. Phys. **71** (1), 145 (1992).

Translated by P. Pozdeev

Technical Physics Letters, Vol. 28, No. 5, 2002, pp. 416–418. Translated from Pis'ma v Zhurnal Tekhnicheskoĭ Fiziki, Vol. 28, No. 10, 2002, pp. 35–40.
Original Russian Text Copyright © 2002 by Esepkina, Kruglov, Rozanov, Saenko, Solomonov.

Characteristics of an Acoustooptical Spectrometer for Remote Atmospheric Sounding in the Millimeter Wavelength Range

N. A. Esepkina, S. K. Kruglov, S. B. Rozanov, I. I. Saenko, and S. V. Solomonov
St. Petersburg State Technical University, St. Petersburg, 195251 Russia
Lebedev Institute of Physics, Russian Academy of Sciences, Moscow, 117924 Russia

Received January 16, 2002

Abstract—We consider the main characteristics and application features of an acoustooptical spectrometer with a 500 MHz bandwidth employed in a ground setup for remote measurements of the atmospheric ozone emission band with a central frequency of 142.175 GHz. The results of determination of the instrument parameters and the examples of atmospheric ozone spectra are presented. © *2002 MAIK "Nauka/Interperiodica".*

Deterioration of the condition of the protective ozone layer in the Earth's atmosphere as a result of unfavorable processes and anomalous phenomena stimulate increasing interest in the development of methods for studying the spatiotemporal distribution of atmospheric ozone and of the corresponding equipment capable of ensuring rapid and reliable ozone monitoring. The remote sounding of atmospheric ozone in the millimeter wavelength range offers one of the most effective methods for such investigations. By studying the shape of pressure-broadened rotational spectral lines of the intrinsic thermal emission of ozone measured from the Earth's surface, it is possible to determine the vertical distribution of ozone in the atmosphere from about 15 to 75 km [1, 2].

For realization of the well-known advantages of remote ozone sensing by microwave radiometry (the possibility of continuous 24-h observations, weak dependence on weather conditions, broad range of probed heights), it is necessary to design high-sensitivity radiometers and broadband (up to several hundred megahertz), stable, and reliable spectrometers. An important place in this equipment belongs to acoustooptical spectrometers (AOSs).

Acoustooptical spectrum analyzers designed and constructed at the St. Petersburg State Technical University were successfully employed in radioastronomic receiving stations [3, 4]. Below we will consider some characteristics of an AOS intended for use in a microwave ozonometer developed at the Lebedev Institute of Physics (Moscow) [2, 5].

The input part of the ozonometer represents a double-beam superheterodyne detecting radiation in a 2-mm wavelength range. The parallel beams (with a width of about 1.5° on a –3 dB level) are switched at a frequency of 75 Hz with the aid of an obturator and a system of mirrors. One of these beams (reference) is absorbed by a blackbody cooled with liquid nitrogen, occurring at a brightness temperature of $T_c = 110$ K. For the other beam (signal), directed skyward, the frequency dependence of the brightness temperature is determined primarily by the rotational spectral line of ozone with a central frequency of 142.175 GHz ($10_{0.10}$–$10_{1.9}$ transition). In the detector calibration stage, this beam is absorbed by a load occurring at room temperature (T_0).

The input signal, together with oscillations of the first heterodyne tuned to 140.42 GHz, are fed via a quasioptical diplexer (representing a modified Mach–Zehnder interferometer) and a scalar horn into a waveguide mixer. The mixer (based on a planar Schottky diode) converts the signal into a working frequency band of the AOS (1.5–2.0 GHz). By changing a path difference in the diplexer, the detector is tuned to operate in a double- or single-band mode. The double-band noise temperature of the detector amounts to 650–700 K in the middle part of the analyzed frequency band. The phase-lock system of the first heterodyne provides for a short-time (0.2 s) relative frequency stability of about 2×10^{-8}.

The detected signal, converted into the 1.5–2.0 GHz frequency range and amplified, is processed in the acoustooptical spectrum analyzer. The AOS is essentially an optoelectronic system with the optical part representing a traditional acoustooptical Fourier-transform processor with spatial integration, including a coherent light source (He–Ne laser), an anamorphosing light-beam collimation system, a lithium niobate crystal acoustooptical deflector (central frequency, 1750 MHz; time aperture, 1.5 μs; efficiency, 1.5×10^{-2} W^{-1}), and a Fourier objective. A linear charge-coupled-device (CCD) photodetector array situated in the output plane of the Fourier processor contains 2048 (14 × 14 μm) sensor cells. The optical processor is designed as a module with dimensions of 400 × 250 × 120 mm, accommodating several independently adjusted optomechanical units mounted on the surface of a common base plate.

The illuminance distribution along one of the coordinate axes measured in the output plane of the optical processor is proportional to the distribution of the spectral power of the detected signal. The readout, digitization, and conversion of this distribution into electric signal is performed by the CCD photodetector array. The charge packets accumulated in the photodetector cells are integrated and sequentially fed to the shift register output, where a digital signal spectrum is formed. The transmission bandwidth of an equivalent filter of each channel and the total number of channels are determined by the characteristics of elements of the optical processor and photodetector. A high precision of adjustment of the whole set of spectral channels is ensured by the high accuracy of arrangement of the photodetector cells.

Figure 1a presents the frequency calibration of the AOS channels performed in the stage of setup preparation to the observations. The spectrometer bandwidth on a –3 dB level amounts to 500 MHz. The maximum deviation of the frequency scale calibration from the linear approximation does not exceed ±0.25% of the analyzed band. This nonlinearity leads to small variations in the bandwidth of spectral channels, which does not exceed ±2% of the average channel bandwidth in the entire analyzed band. Figure 1b shows an example of the frequency characteristics of three adjacent channels of the AOS. The bandwidth of each channel on a –3 dB level is 0.9 MHz, and the frequency step between channels is about 0.6 MHz.

The need for prolonged accumulation of weak signals poses rather strict requirements with respect to stability of the amplitude and frequency characteristics of the AOS. Measurements of the long-term stability of the frequency calibration of the AOS showed that the frequency scale shifts as a whole in response to the ambient temperature variations, while barely changing in shape. Therefore, the temperature correction of the frequency calibration of the AOS can be performed in the stage of the secondary data processing, provided that the position of a stable-frequency reference marker relative to selected photodetector elements is monitored in the course of measurements [4].

The long-term stability of the amplitude calibration of the AOS was checked by measuring the spectrometric Allan dispersion as a function of the accumulation time [6]. The effective accumulation time between amplitude calibrations was not less than 300 s. The amplitude characteristic of the AOS was measured using harmonic and noise input signals. A linear portion of the amplitude characteristic corresponds to the input signal variation over 24 dB and is limited by parameters of the output signal processing system in the optical processor.

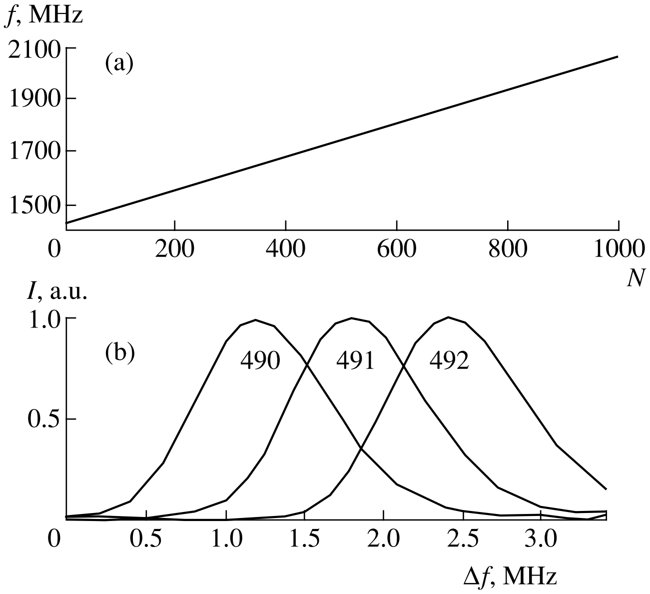

Fig. 1. Parameters of the acoustooptical spectrometer with a 500-MHz bandwidth: (a) frequency calibration; (b) frequency–amplitude characteristics of three adjacent channels (N is channel number, Δf is frequency deviation).

The data acquisition system of the AOS, based on a digital signal processor of the ADSP2181 type, provides for the photodetector operation control according to a preset program, analog-to-digital signal conversion, and preliminary digital data processing and storage in a buffer, followed by data transfer to a computer and file recording. In the preliminary processing stage, the signal processor performs separate accumulation of the signal spectrum for each of the two beams, with the buffer storage switched at a rate of the input signal modulation (lock-in accumulation scheme).

The subsequent processing of data recorded in the files includes step-by-step averaging over a preset accumulation time interval and computation of the difference spectra using the signals of two beams proportional to the calibrated and measured temperature difference. By these data, the spectrum of the brightness temperature of the sky is calculated, which contains the ozone emission line of interest [2, 5]. Figure 2 shows an example of the ozone spectrum recorded using this AOS (Moscow, June 2001) in a 350-MHz band (570 AOS channels). The detector operated in a double-band mode; the tropospheric attenuation of the spectral line was about 3 dB. In the final data-processing stage, separate spectra (analogous to that presented in Fig. 2) are integrated and the total vertical distribution of the ozone emission line intensity is reconstructed [2].

The results of determination of the characteristics of the broadband acoustooptical spectrometer and successful observation of the ozone spectra with the proposed AOS confirm the expediency of using such

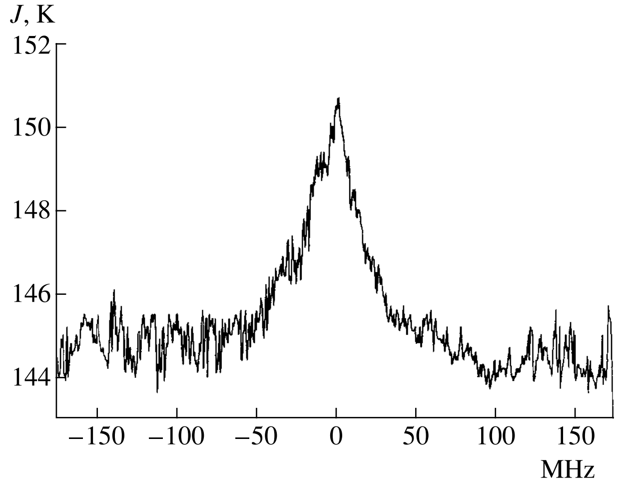

Fig. 2. A typical ozone emission spectrum measured at a zenith angle of 60° using the AOS operating in a double-band mode (calibration time, 96 s; measurement time, 192 s; $T_c = 110$ K, $T_0 = 299$ K). Ordinate indicates deviation from the emission line center.

instruments in the existing and future on-ground equipment for the remote microwave sounding of small gaseous atmospheric components.

Acknowledgments. This study was supported by the Russian Foundation for Basic Research (project nos. 99-02-18132, 00-02-17405a, and 00-05-64976) and by the Council for Support of Leading Scientific Schools (project nos. 00-15-99-071 and 00-15-96586).

REFERENCES

1. *Atmospheric Remote Sensing by Microwave Radiometry*, Ed. by M. A. Janssen (Wiley, New York, 1993), Chap. 7.
2. S. V. Solomonov, S. B. Rozano, E. P. Kropotkina, *et al.*, Proc. SPIE **3406**, 135 (1998).
3. N. A. Esepkina, C. A. Molodyakov, and I. I. Saenko, Photonics Optoelectron. **5** (2), 63 (1998).
4. N. A. Esepkina, I. I. Zinchenko, I. I. Saenko, *et al.*, Izv. Vyssh. Uchebn. Zaved., Radiofiz. **43** (11), 935 (2000).
5. S. V. Solomonov, S. B. Rozanov, E. P. Kropotkina, *et al.*, Radiotekh. Élektron. (Moscow) **46** (12), 1519 (2000).
6. R. Schieder, V. Tolls, and G. Winnerwisser, Exp. Astron. **1**, 101 (1989).

Translated by P. Pozdeev

Technical Physics Letters, Vol. 28, No. 5, 2002, pp. 419–421. Translated from Pis'ma v Zhurnal Tekhnicheskoĭ Fiziki, Vol. 28, No. 10, 2002, pp. 41–45.
Original Russian Text Copyright © 2002 by Tchen.

On Spherical X-ray Wave Focusing upon Backscattering from a Parabolic Cylinder Crystal

T. Tchen
Moscow State Academy of Fine Chemical Technology, Moscow, Russia
e-mail: docent65@mtu-net.ru; ttchen@e-mail.ru

Received July 16, 2001; in final form, November 19, 2001

Abstract—The focusing of a spherical X-ray wave upon the Bragg backscattering from a crystal uniaxially bent to form a parabolic cylinder is theoretically studied. Based on geometrical optics, an analytical formula for the size of the crystal surface area involved in the diffraction reflection in the backscattering mode is derived. The analytical expression for the wave intensity distribution at the focus is analyzed and compared to that obtained previously. *© 2002 MAIK “Nauka/Interperiodica”.*

The backscattering of X-ray radiation under Bragg diffraction conditions ($\theta_B = \pi/2$) from a bent crystal differs from the “usual” diffraction ($\theta_B \neq \pi/2$) in that the size $2\Delta\theta \sim 2|\chi_{hr}|^{1/2}$ of the total reflection region in the former case is significantly (by 2–3 orders of magnitude) greater than that in the latter case (θ_B is the Bragg angle and χ_{hr} is the Fourier component of the X-ray polarizability). The intensity of the reflected beam increases approximately to the same extent. In addition, geometric aberrations in the backscattering mode are minimized as a result of the normal wave incidence onto the crystal. These advantages of X-ray diffraction in the backscattering mode explain the interest of researchers in this phenomenon [1–3].

Below we will obtain, within the framework of geometrical optics, an analytical expression for the size of the region on the surface of a bent crystal involved in the backscattering of a spherical incident wave. In addition, an analytical formula for the wave intensity distribution at the focus will be derived for the first time with an allowance for the terms on the order of $\sim x^4$ in the reflected wave phase.

Let us consider a uniaxially bent crystal with a curvature radius R_x (see figure). Denoting by φ_{0x} the angle between an arbitrary beam incident upon the crystal at a point with the coordinates (x, $z \approx x^2/2R_x$) and the X axis, and by φ_{0z} the angle between a reflected beam and the Z axis, we can write an expression for these angles in the backscattering mode:

$$\cos\varphi_{0x} \cong x/L_0 - x^3(1 - L_0/R_x)/2L_0^3,$$
$$\cos\varphi_{0z} \cong -1 + x^2/2L_0^2 + x^4(1/R_x - 3/4L_0)/2L_0^3. \tag{1}$$

For coherent and elastic reflection, $\mathbf{k}_0 + \mathbf{h} = \mathbf{k}_h$, $k_0^2 = k_h^2 = k^2$, $h_0 = 2k\sin\theta_B$, and $\mathbf{h} = \mathbf{h}_0 - \nabla(\mathbf{h}_0\mathbf{u})$, where $\mathbf{h}_0$ and $\mathbf{h}$ are the reciprocal lattice vectors of the unbent and bent crystals, respectively; $\mathbf{u}(-xz/R_x, 0, x^2/2R_x)$ is the vector of displacement of the reflecting planes in the elastically bent crystal; and $\mathbf{k}_0$ and $\mathbf{k}_h$ are the wavevectors of the incident and diffracted beams, respectively. In this case, the angular halfwidth of the Bragg backscattering curve is as follows:

$$\Delta\theta = \Big|2x^2/R_xL_0 + x^2/L_0^2 + x^2/R_x^2 + x^4/2R_x^2L_0^2 - 3x^4/4L_0^4 - x^4/R_x^3L_0 - 3x^4/4R_x^4\Big|^{1/2}. \tag{2}$$

For a plane wave ($L_0 \gg R_x$), this expression simplifies to

$$\Delta\theta = \left|x^2/R_x^2 - 3x^4/4R_x^4\right|^{1/2}. \tag{3}$$

In the case of $x^2/R_x^2 \ll 1$, we can use this relationship to estimate the size of the crystal surface involved in the plane wave backscattering:

$$x_{pl} \approx R_x\Delta\theta \approx R_x|\chi_{hr}|^{1/2}. \tag{4}$$

As can be seen, the intensity of a beam reflected under Bragg's conditions from a bent crystal increases by a factor of $|\chi_{hr}|^{-1/2}$ as compared to the case of $\theta_B \neq \pi/2$. An analogous approach of geometrical optics to the Bragg reflection was previously employed in [4].

Now we will study the distribution of wave intensity in the immediate vicinity of the source image (i.e., at the focus). Before proceeding to this, note that there are two modes of crystal bending. In the first case, the reflecting surface is also bent to acquire the shape of a parabolic cylinder ($z \approx x^2/2R_x$). Alternatively, the crystal can be bent so as to retain a flat reflecting surface ($z \approx 0$, see [5]). This study addresses the first model of bending.

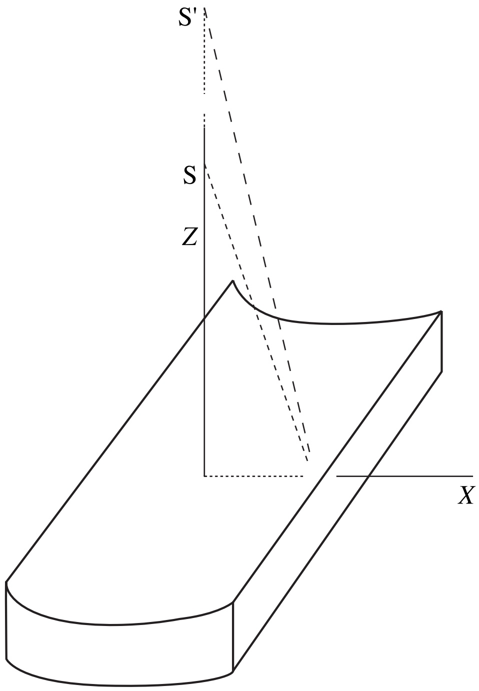

The scheme of focusing a spherical X-ray wave upon backscattering from a uniaxially bent cylindrical crystal: S and S' are the point radiation source and its image, respectively.

Proceeding from the geometrical considerations, we obtain

$$\begin{aligned} L_{0,h}(x) = L_{0,h(0)}[1 + x\sin\varphi_{0,h}L_{0,h(0)} + x^2\alpha_{0,h}/2L_{0,h(0)} \\ - x^3\sin\varphi_{0,h}\cos^2\varphi_{0,h}/2L_{0,h}^3 \\ + x^3\sin\varphi_{0,h}\cos\varphi_{0,h}/2L_{0,h(0)}^2R_x - x^4/8L_{0,h(0)}^4 \\ + x^4\sin^2\varphi_{0,h}/8R_x^2L_{0,h(0)}^2 + x^4\cos\varphi_{0,h}/4L_{0,h(0)}^3R_x \\ + 3x^4\sin^2\varphi_{0,h}\{1/L_{0,h} - \cos\varphi_{0,h}/R_x\}/4L_{0,h}^3, \end{aligned} \qquad (5)$$

where $\cos\varphi_{0,h}$ are the directional cosines of the incident and diffracted waves, $L_{0,h(0)}$ are the “aberration-free” distances from the point source of the spherical wave to the crystal and from the crystal to the source image, respectively, and

$$\alpha_{0,h} = \cos^2\varphi_{0,h}/L_{0,h(0)} - \cos\varphi_{0,h}/R_x. \qquad (6)$$

Considering the case of symmetric backscattering ($\varphi_0 = \varphi_h = \pi/2 - \theta_B$), we retain in (5) terms up to the fourth order only for the diffracted wave. Using the dynamic theory of X-ray diffraction in elastically bent crystals [5–7], we obtain an expression for the diffracted wave intensity at a point ξ_p in the vicinity of the focus:

$$\begin{aligned} I_h(\xi_p) \sim \Big|\kappa^2C\chi_{hr}\sigma_h(8\pi^{3/2}R_x^2\sin^2 2\theta_B)^{-1} \\ \times\int dyR(y)\exp(-iy^2\sigma_h^2/2\kappa\alpha_0) \\ \times\int dx\exp[i\kappa\{\xi_p x/L_{h(0)} - y\sigma_h x/\kappa \\ + \alpha_h x^2/2 + x^4(1/R_x - 1/2L_0)/4L_0^2\}]\Big|^2. \end{aligned} \qquad (7)$$

Here, $\kappa = 2\pi/\lambda$, C is the polarization factor, $\sigma_h = \kappa\chi_h/2\cos\theta_B$, λ is the incident radiation wavelength, $R(y)$ is the plane-wave amplitude reflection coefficient, and y is the normalized angular variable [8]. Taking into account that the integral with respect to x in Eq. (7) is essentially the Pearsey integral [9], we obtain the final expression for the diffracted wave intensity:

$$I_h(\xi_p) \sim 4\Big|\Phi(\kappa A_4)^{-1/4}R(y \approx 0)I_p^{y\approx 0}(A_1, A_2)\Big|^2, \qquad (8)$$

where Φ is the factor at the integral with respect to y in Eq. (7),

$$\begin{aligned} I_p(A_1, A_2) \\ = \int\exp[i(A_2t + A_1t^2 + t^4)]dt \end{aligned}$$

is the Pearsey integral, and

$$\begin{aligned} A_1 &= \kappa\alpha_h/\{2(\kappa A_4)^{1/4}\}, \\ A_2 &= [\kappa\xi_p/L_{h(0)} - y\sigma_h/\kappa]/\{\kappa A_4\}^{1/4}, \\ A_4 &= (1/R_x - 1/2L_0)/4L_0^2. \end{aligned} \qquad (9)$$

Let us consider the case of $L_0 = R_x/2$ and ignore the terms $\sim x^4$. Upon taking the integral with respect to x and y in (7) and using the geometrical focusing condition $\alpha_0 + \alpha_h = 0$, we obtain

$$\begin{aligned} I_h(\xi_p) \\ \sim |\Phi J_1(\xi_p\sigma_h/\alpha_hL_{h(0)})/(\xi_p\sigma_h/\alpha_hL_{h(0)})|^2\Theta(\xi_p/\alpha_hL_{h(0)}), \end{aligned} \qquad (10)$$

where $J_1(t)$ is the real first-order Bessel function and $\Theta(q)$ is the Heaviside unit step function. Note that formula (10) coincides with the result obtained by Gabrielyan *et al.* [10].

REFERENCES

1. K. Kohra and M. Matsushita, Z. Naturforsch. A **27**, 484 (1972).
2. A. Caticha and S. Caticha-Ellis, Phys. Rev. B **25**, 971 (1982).
3. V. I. Kushnir and É. V. Suvorov, Pis’ma Zh. Éksp. Teor. Fiz. **48** (2), 109 (1988) [JETP Lett. **48**, 117 (1988)].
4. T. Chen, V. A. Bushuev, and R. N. Kuz’min, Zh. Tekh. Fiz. **60** (10), 60 (1990) [Sov. Phys. Tech. Phys. **35**, 1148 (1990)].
5. K. T. Gabrielyan, F. N. Chukhovskiĭ, and Z. G. Pinsker, Zh. Tekh. Fiz. **50** (1), 3 (1980) [Sov. Phys. Tech. Phys. **25**, 1 (1980)].
6. F. N. Chukhovskii, K. T. Gabrielyan, and P. V. Petrashen’, Acta Crystallogr. A **34**, 610 (1978).
7. F. N. Chukhovskiĭ, Metallofizika **3** (5), 3 (1981).
8. Z. G. Pinsker, *X-ray Crystal Optics* (Nauka, Moscow, 1982).
9. T. Pearsey, Philos. Mag. **37**, 311 (1946).
10. K. T. Gabrielyan, F. N. Chukhovskiĭ, and D. I. Piskunov, Zh. Éksp. Teor. Fiz. **96** (3), 834 (1989) [Sov. Phys. JETP **69**, 474 (1989)].

Translated by P. Pozdeev

Technical Physics Letters, Vol. 28, No. 5, 2002, pp. 422–426. Translated from Pis'ma v Zhurnal Tekhnicheskoĭ Fiziki, Vol. 28, No. 10, 2002, pp. 46–56.
Original Russian Text Copyright © 2002 by Gundienkov, Yakovlenko.

The Interaction between Charged Dust Particles Calculated in Cassini Coordinates

V. A. Gundienkov and S. I. Yakovlenko

Institute of General Physics, Russian Academy of Sciences, Moscow, 117924 Russia

Received November 7, 2001

Abstract—The Poisson–Boltzmann equation for two charged dust particles surrounded by a cloud of charged plasma was numerically solved using the Cassini coordinates. The force of the electric field acting on each particle was determined by integrating the field pressure over the particle surface. It is shown that the dust particles can exhibit attraction at distances on the order of the Debye screening radius and the average spacing between particles. The attraction drops sharply if the particle charge is significantly smaller than the charge of surrounding plasma species. © *2002 MAIK "Nauka/Interperiodica".*

Introduction

According to experimental data [1–3], particles of micron dimensions existing in plasmas generated by thermal emission, gas discharge, or nuclear excitation can form spatial structures. Therefore, it is natural to suggest that attractive forces may exist between such charged particles surrounded by a cloud of charges of opposite sign. According to the results of numerical calculations [4, 5] and an approximate theoretical analysis [6], attraction between dust particles must actually take place. However, an exact solution of the Poisson–Boltzmann equation shows that charged planes occurring in an electron cloud or in a plasma always exhibit repulsion rather than attraction [7].

In order to elucidate this discrepancy, we have studied the problem of interaction between charged particles surrounded by an electron cloud and a plasma, based on a high-precision numerical calculation of the electric potential.

Formulation of the Problem

Poisson–Boltzmann equation. Let the electron gas surrounding dust particles be formed at the expense of electron emission from these particles possessing a sufficiently high temperature T. In addition, the particles are surrounded by a partly ionized gas. In order to determine the spatial distribution of potential ϕ, electric field strength $-\nabla\phi$, and charge density $\rho = e(N_i - N_e)$, we have to solve the Poisson equation $\nabla(-\nabla\phi) = 4\pi\rho$ with the densities of ions (N_i) and electrons (N_e) obeying the Boltzmann distributions $N_i = N_{i0}\exp(-e\phi/T)$ and $N_e = N_{e0}\exp(-e\phi/T)$, where N_{i0} and N_{e0} are the ion and electron densities at the points of zero potential; ∇ is the Hamiltonian vector operator.

Thus, the Poisson–Boltzmann equation takes the form

$$\Delta\phi = 4\pi e(N_{e0}\exp(e\phi/T) - N_{i0}\exp(-e\phi/T)), \quad (1)$$

where $\Delta = \nabla^2$ is the Laplace operator; the particle and plasma temperatures are assumed to be equal.

Dimensionless variables. Let us measure distances in units of the Debye screening radius $r_D = (T/4\pi e^2 N_{e0})^{1/2}$ corresponding to the electron density at the points of zero potential. The dimensionless potential φ, field strength $\mathbf{E}$, and electron density n_e are defined by the relationships

$$\begin{gathered}\varphi = \phi e/T; \quad \mathbf{E} = -\nabla\phi e r_D/T; \\ n_e = r_D^3 Ne = n_D\exp(\varphi),\end{gathered} \quad (2)$$

where $n_D = r_D^3 N_{e0}$ is the number of particles in the Debye sphere.

For example, under the experimental conditions studied in [1], where $N_{e0} = 2.5 \times 10^{10}$ cm^{-3} and $T = 0.146$ eV = 1700 K, the characteristic values are as follows: $r_D = 0.002$ cm; $T/e = 0.146$ V; $T/er_D = 80$ V/cm. For an average particle radius of $r_0 = 0.4$ μm ($r_0/r_D = 0.02$) and a charge of $Z_pe = 500e$, the electric field strength at the particle surface is estimated at $Z_pe/r_0^2 = 4.5 \times 10^4$ V/cm ($E_0 = E(r_0) = 550$).

In terms of these dimensionless quantities, Eq. (1) reduces to the following equation for the dimensionless potential φ:

$$\Delta\varphi = \exp(\varphi) - \delta\exp(-\varphi), \quad (3)$$

where $\delta = N_{i0}/N_{e0}$ is the parameter describing additional ionization of the gas; $\nabla\mathbf{E} = -(\exp(\varphi) - \delta\exp(-\varphi))$; and $\mathbf{E} = -\nabla\varphi$. With an allowance for quasineutrality of the plasma, $0 \le \delta \le 1$.

1063-7850/02/2805-0422$22.00 © 2002 MAIK "Nauka/Interperiodica"

Equation (3) can be studied analytically only in a plane case [7–9].

Boundary conditions. Following [10], a single charged dust particle in a thermodynamic equilibrium with a surrounding cloud of light charges will be referred to as a Debye atom, while two (or more) such particles are called a Debye quasi-molecule [4, 5]. Descriptions of the Debye atom and quasi-molecule differ only in the geometry of the problem. In considering the Debye atom with a spherically symmetric electron cloud, we may solve a one-dimensional Poisson equation. For the Debye quasi-molecule, the problem can be considered symmetric relative to the axis z coinciding with the line connecting the nuclei (centers of dust particles). Then it is sufficient to consider a two-dimensional equation (3) in the coordinate plane (z, y). However, a significant complication of the problem for the Debye quasi-molecule is related to the selection of two-dimensional boundary conditions.

In a real physical problem, we set the particle charge Z_pe and radius r_0 (for the process of particle charge formation, see [11]). Therefore, one of the boundary conditions is related to the field strength on the particle surface S:

$$\mathbf{E}_0 = -\nabla\varphi|_S. \tag{4}$$

The particle charge is determined as

$$Z_p = \frac{-r_D^2}{4\pi e}\int_S \nabla\phi ds, \quad z_p = \int_S \mathbf{E} ds, \tag{5}$$

where z_p is the dimensionless charge, which is related to that expressed in units of electron charge (Z_p) as $Z_p = z_pn_D$ (the surface area is measured in units of the squared Debye radius).

The second boundary condition indicates the surface S' on which the field is zero:

$$\nabla\varphi|_{S'} = 0. \tag{6}$$

A zero value of the electric field strength on the system boundary follows from the condition of quasineutrality.

It should be pointed out that the main purpose of considering the Debye molecule is to find the resultant electrostatic forces acting on particles as a function of the distance between them. For this purpose, it is more convenient to proceed from boundary conditions formulated in a different way [4, 5], whereby a constant potential (rather than the field strength) is set on the particle surface:

$$\varphi|_S = \varphi_0 = \text{const.} \tag{7a}$$

A solution to the Poisson–Boltzmann equation gives the field strength $\mathbf{E}_0$ on the particle surface. The resultant force is determined by integrating the electrostatic pressure over the particle surface. The required charge z_p (5) is obtained by properly selecting the potential φ_0.

In the case under consideration, the force of interaction between particles is directed along the z axis and is equal to

$$F = \frac{1}{8\pi}\int_S (\nabla\phi)^2|_S ds_z, \quad f = \int_S E_0^2 ds_z, \tag{7b}$$

where ds_z is the projection of the surface element ds onto the z axis. The force F is related to the dimensionless force f as $F = (T^2/8\pi e^2)f$; the electrostatic pressure is directed outward from the particle surface.

Solution of the Problem

Cassini coordinates. For determining the exact value of a force acting upon the particle, the method used for solving the Poisson–Boltzmann equation has to provide for maximum accuracy in the vicinity of the particle surface. Of most interest is the case of distances between particles significantly exceeding their diameters. This is difficult to achieve in the usual systems of coordinates. For this reason, we have used the coordinates constructed based on a particular case of the well-known oval of Cassini [12, 13].

The relationship between variables (u, ν) determining a point on the oval of Cassini and the Cartesian coordinates in the quadrant $z > 0$, $y > 0$ is as follows:

$$x(u, \nu) = \frac{d}{2\sqrt{2}}\sqrt{\sqrt{\exp(2u) + 2\exp(u)\cos(\nu) + 1} + \exp(u)\cos(\nu) + 1}, \tag{8a}$$

$$y(u, \nu) = \frac{d}{2\sqrt{2}}\sqrt{\sqrt{\exp(2u) + 2\exp(u)\cos(\nu) + 1} - \exp(u)\cos(\nu) - 1}, \tag{8b}$$

where d is the distance between foci of the oval occupying the points with the Cartesian coordinates $(-d/2, 0)$ and $(d/2, 0)$. On the whole plane (z, y), the coordinate network is obtained by mirror reflections from the z and y axes. The variable $\infty > u > -\infty$ is an analog of the radial coordinate. For $u < 0$, the curve represents two independent ovals; for $u = 0$, the coordinate line is essentially the Bernoulli lemniscate (i.e., an oval with an infinitely narrow waist [12, 13]). For $0.65 > u > 0$, the curve appears as an oval with a finite waist, and for $u > 0.65$, the oval acquires an elliptical shape. The variable $\pi > \nu > 0$ is analogous to an angle in polar coordinates. For $\nu = 0$, the point occurs on the ray $(d/2; -\infty)$; for $\nu = \pi$, the locus approaches an angle formed by the

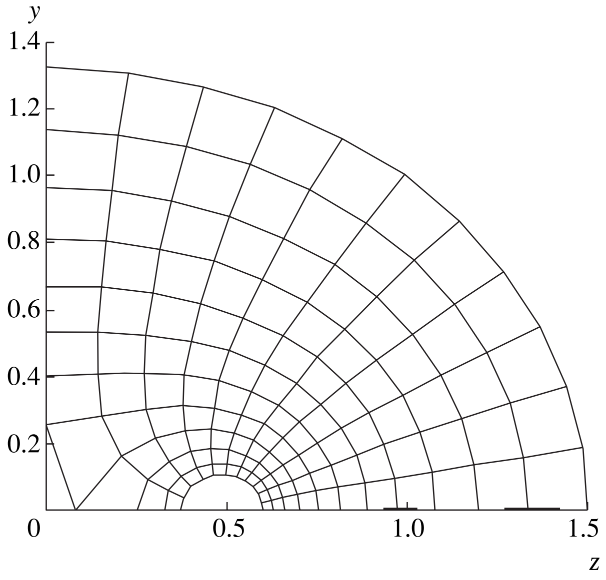

Fig. 1. The Cassini coordinate network for the distance between foci $d = 1$, which approximately corresponds to the attraction changing to repulsion.

segment $(0, d/2)$ and the ray $(0, \infty)$. The character of the Cassini coordinate lines is illustrated in Fig. 1.

Using the Cassini coordinates (8) offers the following advantages. First, the family of Cassini ovals qualitatively agrees with the pattern of equipotential lines for two identical charged particles situated at the oval foci. Second, the domain of the solution of the Poisson–Boltzmann equation in these coordinates becomes rectangular. Third, the network density of ovals exhibits exponential densification on approaching the particle surface. This allows us to use a uniform network even for large distances between small-size particles.

Method of solution. Not dwelling on the details, we only briefly describe the method of solution. The Cassini coordinates are especially convenient in the case when the particle radius r_0 is much smaller than both the Debye radius ($r_0 \ll 1$) and one-half the average distance between particles ($r_0 \ll a_0 = N_p^{1/3}/2$, where N_p is the particle number density). Then, considering the region of distances between particles $5r_0 < d < 5a_0$, we may consider the particles as Cassini ovals close to circles. It is convenient to set a constant potential φ_0 on this oval. At the same time, the cloud of electrons surrounding the particles is described by an elliptical oval, on which it is convenient to set the zero field.

The surface of the particle of radius r_0 and the external surface of the electron cloud (corresponding to the radius of electron cloud a_0 of a single particle) are described in Cassini coordinates (8) by the constants

$$u_{\min} = \ln\left(\frac{4r_0}{d^2}(d + r_0)\right), \quad u_{\max} = \ln\left(\frac{4a_0}{d^2}(d + a_0)\right), \quad (9)$$

with the boundary conditions (2) acquiring the form of

$$\varphi\big|_{u = u_{\min}} = \varphi_0, \quad \left.\frac{\partial\varphi}{\partial u}\right|_{u = u_{\max}} = 0. \quad (10)$$

The Poisson–Boltzmann equation (3) with the boundary conditions (10) was numerically solved by the Gauss–Newton iterative method using the MATLAB program package.

The particle charge and the force of interaction between articles were calculated in three-dimensional coordinates obtained by rotating plane coordinates (8) around the z axis. In these coordinates, the force of interaction between the particles was calculated by formula (7). The energy of this interaction was calculated by the formula

$$U(d) = \int_d^0 f(x)dx + \text{const}. \quad (11)$$

In the results presented below, the integration constant was selected so that the energy $U(d)$ at the minimum would be zero: $\min(U(d)) = 0$.

Results of Numerical Calculations

Selecting calculation parameters. The numerical calculations were performed for the parameters φ_0, r_0, a_0, which correspond to a single Debye atom at $d \gg a_0$. For this purpose, we have first solved a spherically symmetrical problem in which the field strength and potential at $r = a_0$ were set equal to zero (for detail, see [10]). From a solution to this problem, we determined the potential φ_0 on a particle of the given radius r_0. With this set of φ_0, r_0, a_0, we solved a two-center problem for $d = 10a_0$. The results for the spherically symmetrical and two-center problem coincided with high precision. The subsequent series of calculations was performed for smaller d values. The main attention was paid to a thermoemission plasma with $\delta = 0$.

With a view to studying the same plasma parameters as in [1], we selected $a_0 = 0.755$. According to the results of calculations, the most interesting region corresponds to relatively large distances $d \sim 1$. Assuming that $d \sim r_0$ corresponds to a weak polarization of the electron cloud in the vicinity of the particle surface, we used a particle radius of $r_0 = 0.1$ (i.e., five times greater than the experimental value). Accordingly, the potential $\varphi_0 = 1.16$ taken from the solution of the one-center problem for $r_0 = 0.1$ proved to be significantly smaller than the potential on the surface of a small-size particle.

On the attraction changing to repulsion. In order to determine how the force of interaction between particles depends on the distance d between them, we performed a series of calculations with various sets of φ_0, r_0, a_0. The particle charge z_p proved also to depend on d. For this reason, additional calculations were performed using φ_0 or a_0 modified so as to make the z_p value independent of d.

These calculations showed that repulsion takes place at small distances ($d \sim r_0$) between particles. This result disagrees with data obtained previously [4, 5], where the case of $d \sim r_0$ was characterized by attraction. Apparently, the numerical calculations in [4, 5] involved a significant error related to the calculation of potential at the particle surface: the resultant force is highly sensitive to this uncertainty.

In the calculations reported here, the attraction changes to repulsion at $\delta = 0$ for a distance $d \approx 1.3$ (Fig. 2), which approximately corresponds to the average spacing between particles $2a_0 = 1.5$. The value of d_0 at which the force changes sign depends but weakly on the type of quantities (φ_0, a_0 versus z_p, a_0) remaining constant in the course of distance variation. The effect of a_0 (at constant z_p, φ_0) on the d_0 value was somewhat more pronounced. Since the problem cannot be considered as binary for $d \gg a_0$, we present the results of calculation only for relatively small distances $d < 4$.

In the case of $\delta = 1$, the attraction between particles drops sharply and becomes virtually insignificant. This result disagrees with the data reported in [6], which is probably explained by the fact that the calculations in [6] did not take into account polarization of the charged clouds.

Interaction between nonpolarized particles. Assuming that the shells of the Debye atoms do not interact with each other, we arrive at a situation when only repulsion takes place between the particles. Indeed, the force of interaction between nonpolarized shells can be expressed as

$$f(d) = z_{\text{eff}}(d)z_p/d^2,$$

where $z_{\text{eff}}(d) = 4\pi E(d)d^2$ is the total charge inside a sphere of radius d centered at the particle (uncompensated fraction of the particle charge). Owing to the quasineutrality of the Debye atom, we conclude that $z_{\text{eff}}(r) \geq 0$ for $r > r_0$. Charges of the same sign would repel: $z_{\text{eff}}(d)z_p \geq 0$.

For the attracting forces to dominate, the charged shells have to experience rearrangement (polarization). This will lead to an increase in the number of charges situated on the axis of the Debye molecule and attracting the particles. Thus, the appearance of attraction between charged dust particles is related to polarization of the electron clouds, whereby the system deviates from the planar geometry [7].

Conclusion

In concluding, it should be noted that, first, the forces of attraction between dust particles arise at a sufficiently large distance approximately equal to their average spacing and to the Debye radius corresponding to the electron density at one-half the average distance between the particles. Second, the attraction is significant when charges of one sign are predominantly concentrated on the dust particles.

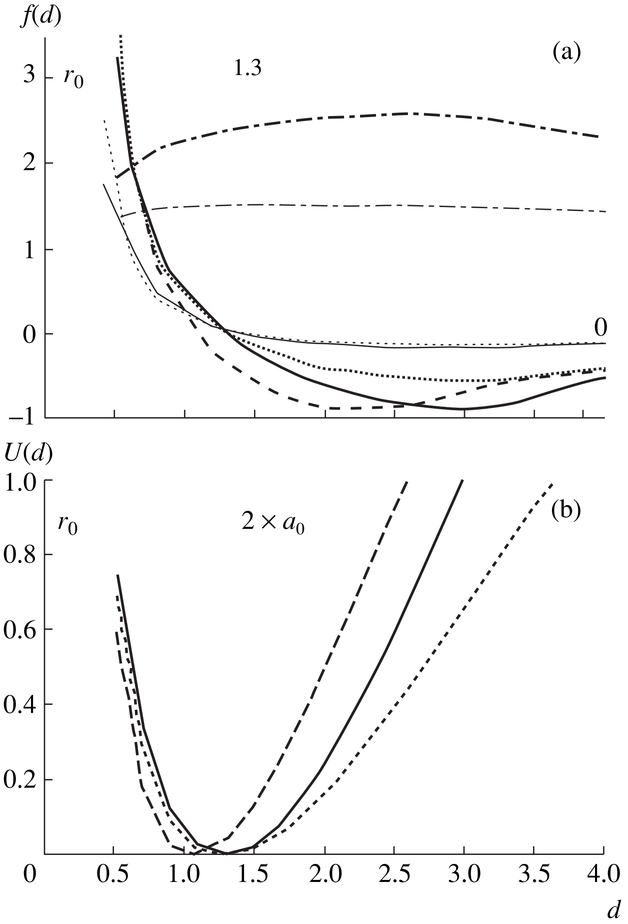

Fig. 2. Plots of the (a) force projection onto the z axis and (b) potential energy of interaction between dust particles versus the distance between them. A positive force corresponds to repulsion, and a negative force—to attraction between particles. The potential energy $U(d)$ is normalized so as to be zero in the point of minimum. Thick solid curves correspond to a constant potential of $\varphi_0 = 1.16$ on the particle surface; dotted curves correspond to a constant charge ($z_p = 2$ for $\delta = 0$; $z_p = 1.35$ for $\delta = 1$) determined by the selection of $\varphi(d)$; dashed curves correspond to a constant charge determined by selecting $a_0(d)$ at $\varphi_0 = 1.16$; and dot–dash curves in (a) show the particle charge as a function of the distance for a constant potential $\varphi_0 = 1.16$ and $a_0 = 0.755$.

Taking into account that the attractive forces arise at large distances, the formation of dust fluids and crystals can be correctly described only with an allowance for many-body interactions between such particles. However, the results reported above lead to two important conclusions concerning the criteria for manifestation of the collective phenomena:

(a) in the case of a thermoemission plasma, the electron density must be such that the Debye radius would be equal to approximately one-half the average distance between particles;

(b) in a gas-discharge or nuclear-excited plasma, the properties of the ionization source and the particle number density must be correlated so that the main (usually, negative) charge would be carried by these particles.

Acknowledgments. The authors are grateful to Yu.I. Syts'ko for fruitful discussions of the computational aspects of the problem studied.

REFERENCES

1. V. E. Fortov, A. P. Nefedov, O. F. Petrov, *et al.*, Zh. Éksp. Teor. Fiz. **111** (2), 467 (1997) [JETP **84**, 256 (1997)].
2. V. E. Fortov, V. S. Filinov, A. P. Nefedov, *et al.*, Zh. Éksp. Teor. Fiz. **111** (2), 889 (1997) [JETP **84**, 489 (1997)].
3. V. E. Fortov, V. I. Vladimirov, L. V. Deputatova, *et al.*, Dokl. Akad. Nauk **366** (2), 184 (1999) [Dokl. Phys. **44**, 279 (1999)].
4. S. I. Yakovlenko, Kratk. Soobshch. Fiz., No. 9, 3 (1999).
5. S. I. Yakovlenko, Pis'ma Zh. Tekh. Fiz. **25** (16), 83 (1999) [Tech. Phys. Lett. **25**, 670 (1999)].
6. D. N. Gerasimov and O. A. Sinkevich, Teplofiz. Vys. Temp. **37** (6), 853 (1999).
7. S. I. Yakovlenko, Pis'ma Zh. Tekh. Fiz. **27** (9), 83 (2001) [Tech. Phys. Lett. **27**, 389 (2001)].
8. B. V. Derjaguin and L. D. Landau, Acta Physicochim. URSS **14** (6), 633 (1941).
9. S. I. Yakovlenko, Pis'ma Zh. Tekh. Fiz. **26** (8), 47 (2000) [Tech. Phys. Lett. **26**, 337 (2000)].
10. A. N. Tkachev and S. I. Yakovlenko, Zh. Tekh. Fiz. **69** (1), 53 (1999) [Tech. Phys. **44**, 48 (1999)].
11. A. N. Tkachev and S. I. Yakovlenko, Pis'ma Zh. Tekh. Fiz. **25** (1), 52 (1999) [Tech. Phys. Lett. **25**, 21 (1999)].
12. *Mathematical Encyclopaedic Dictionary*, Ed. by Yu. V. Prokhorov (Bol'shaya Rossiĭskaya Éntsiklopediya, Moscow, 1995).
13. I. N. Bronshteĭn and K. A. Semendyaev, *Reference Book on Mathematics* (Nauka, Moscow, 1964).

Translated by P. Pozdeev

Technical Physics Letters, Vol. 28, No. 5, 2002, pp. 427–429. Translated from Pis'ma v Zhurnal Tekhnicheskoĭ Fiziki, Vol. 28, No. 10, 2002, pp. 57–63.
Original Russian Text Copyright © 2002 by Kulikov, Malkovich, Skoryatina, Usacheva.

Zinc Diffusion in $YBa_2Cu_3O_{7-x}$ Ceramics

G. S. Kulikov, R. Sh. Malkovich, E. A. Skoryatina, and V. P. Usacheva
Ioffe Physicotechnical Institute, Russian Academy of Sciences, St. Petersburg, 194021 Russia

Received December 17, 2001

Abstract—The process of zinc diffusion in $YBa_2Cu_3O_{7-x}$ ceramics with a porosity of 20–30% was studied in the temperature interval from 110 to 450°C using a ^{65}Zn radioactive tracer. The temperature dependence of the tracer diffusion coefficient is described by the relation $D = 5 \times 10^{-9}\exp(-0.25\ \mathrm{eV}/kT)$ cm^2/s. It is concluded that zinc migrates predominantly via pores and intergranular layers in the ceramics. © *2002 MAIK "Nauka/Interperiodica".*

An important fundamental and practical aspect in the investigation of high-temperature superconductivity is the effect of impurities on the properties of high-temperature superconductors (HTSCs). On the one hand, impurities can be intentionally introduced into an HTSC in order to improve the material properties; on the other hand, impurities can appear in or disappear from a material as a result of thermal treatments. For this reason, investigations of the diffusion of impurities in HTSCs are of considerable interest.

This study is devoted to the diffusion of zinc in HTSC ceramics of the $YBa_2Cu_3O_{7-x}$ (YBCO) type. By introducing zinc into YBCO, we can obtain important information on the nature of superconductivity in this compound [1]. The presence of zinc significantly influences the parameters and electron structure of HTSCs [2]. In particular, this dopant is used for manufacturing thin-film YBCO-based bolometers [3]. Previously, the diffusion of zinc in analogous ceramics was studied by Routbort *et al.* [4] and it was established that the diffusion coefficient of zinc varies from 2.7×10^{-12} to 3.5×10^{-11} cm^2/s for a temperature changed from 798 to 900°C.

Our experiments were performed on the samples of sintered YBCO ceramics in the form of $8 \times 8 \times 1.5$ mm parallelepipeds with a density reaching 70–80% of the theoretical limit and a porosity of 20–30%. A thin layer (~1 μm) of zinc containing the radioactive isotope ^{65}Zn was deposited in vacuum onto the sample face. The subsequent diffusion annealing was conducted in air at 110–450°C for 3–430 h. After termination of the annealing, the sample edges were ground. Then, 3- to 10-μm-thick plane-parallel sections were sequentially removed, the activity of each layer was measured in a gamma counter, and the tracer depth–concentration profiles were constructed.

A characteristic feature of the tracer profiles is the presence of two regions, representing near-surface and bulk layers of the sample (Fig. 1). The near-surface region exhibits a high tracer concentration, which drops sharply from $\sim 5 \times 10^{20}$ cm^{-3} at the surface to $\sim 10^{19}$ cm^{-3} at a depth of 15–20 μm. This part of the profile remains virtually unchanged with increasing temperature and time of annealing. This behavior is explained by zinc falling within open pores on the ceramic surface during deposition (a similar behavior was previously observed for silver [5]). In contrast, the bulk region is characterized by a rather slow variation of the tracer concentration. In this part of the profile, the concentration monotonically increases with the temperature and time of annealing, as well as with the sample porosity.

Assuming that the diffusion of zinc obeys the Fick law and the surface concentration does not change with time, we determined the tracer diffusion coefficient by comparing the bulk concentration profiles to the erfc curve corresponding to solutions of the Fick equation describing diffusion into the half-space from a constant source $c(0, t)$ = const.

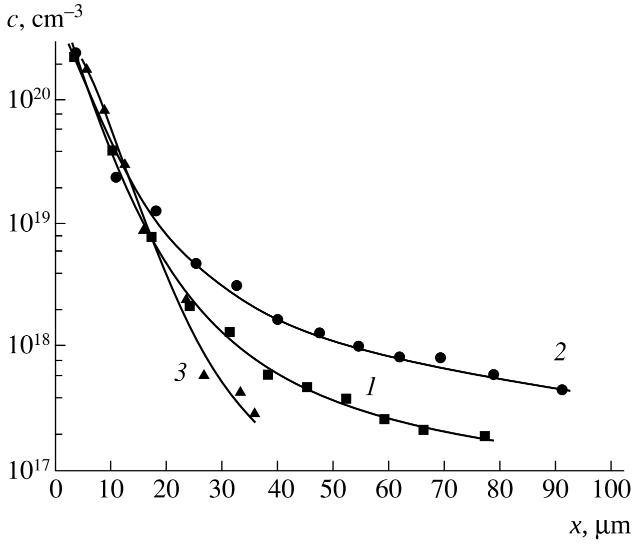

Fig. 1. Depth–concentration profiles of a zinc tracer in YBCO ceramics with a porosity of P = 30 (*1*, *2*) and 20% (*3*) upon diffusion annealing at T = 400°C for t = 3 h 40 min (*1*) and 20 h (*2*, *3*).

1063-7850/02/2805-0427$22.00 © 2002 MAIK "Nauka/Interperiodica"

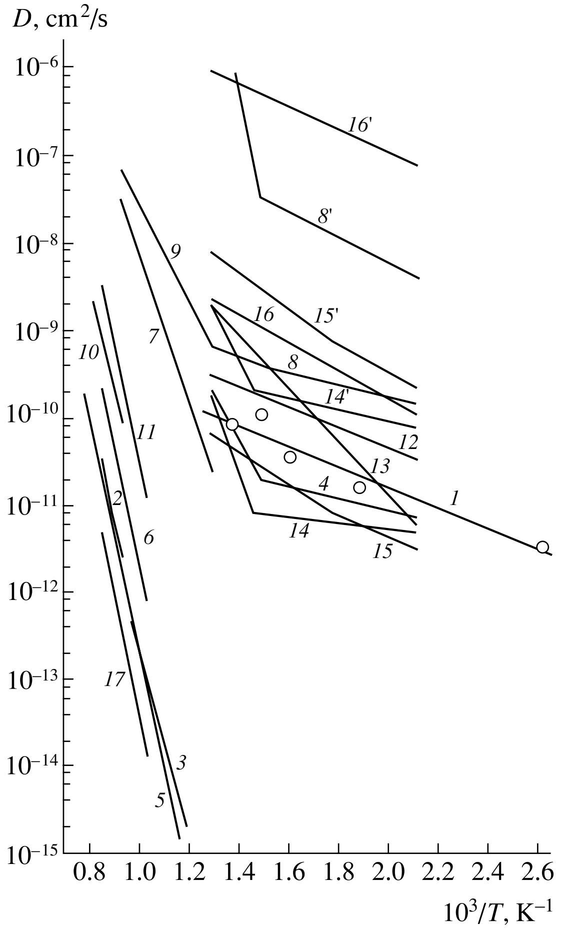

Fig. 2. The plots of diffusion coefficient versus temperature for various impurities in YBCO ceramics: (*1*, *2*) zinc; (*3*, *4*) nickel; (*5*–*7*) copper; (*8*, *8*', *9*, *11*) silver; (*12*) indium; (*13*) tin; (*14*, *14*') gold; (*15*, *15*') sulfur; (*16*, *16*') cadmium; (*17*) cobalt. Curves (*8*, *14*–*16*) refer to a slow, and (*8*', *14*'–*16*') to a fast diffusion component of the same element; (*1*) data of this study; (*2*, *17*) [4]; (*3*) [7]; (*4*, *12*, *13*) [9–11]; (*5*) [4, 7]; (*6*, *11*) [6]; (*7*, *9*) [12]; (*8*, *8*') [13]; (*10*) [8]; (*14*, *14*') [15]; (*15*, *15*') [17, 18]; (*16*, *16*') [16].

As can be seen from the results of this analysis (Fig. 2), the diffusion coefficient of zinc varies from 3.3×10^{-12} to 1.1×10^{-10} cm^2/s in the temperature interval studied (in the sample with a porosity of ~30%). The values of activation energy ε and preexponential factor D_0 calculated from the temperature dependence of the diffusion coefficient are $\varepsilon = 0.25$ eV and $D_0 = 5 \times 10^{-9}$ cm^2/s.

The values of the diffusion coefficient of zinc in YBCO ceramics determined from the results of our experiments in the temperature interval from 110 to 450°C are close to the values reported by Routbort *et al.* [4] for significantly higher temperatures (798–900°C) (see Fig. 2). At the same time, the above values of activation energy ε and preexponential factor D_0 significantly differ from analogous parameters ($\varepsilon = 2.7$ eV and $D_0 = 11$ cm^2/s) calculated using the data reported in [4]. We believe that this discrepancy is fully related to a significant difference between the materials studied: a high-density ceramics (95–97% of the theoretical value) studied in [4] versus low-density material (~70%) used in our experiments.

Sharp differences in the values of diffusion parameters obtained for materials of various densities are observed not only for zinc, but for some other elements (nickel, copper, silver) as well. In high-density (95–97%) ceramics, the diffusion coefficients of these elements do not exceed 2×10^{-13} cm^2/s (at 730°C) [7] for nickel, 8×10^{-13} cm^2/s (730°C) [7] and 7×10^{-11} cm^2/s (950°C) [4] for copper, and 1.5×10^{-8} cm^2/s (950°C) [8] for silver. In contrast, the diffusion coefficients of these elements in low-density (80%) ceramics reach the same or a markedly higher level at much lower temperatures: 7×10^{-12} cm^2/s (200°C) [9–11] for nickel, 10^{-10} cm^2/s (500°C) [12] for copper, and 3×10^{-10} cm^2/s (500°C) [5] or even ~10^{-6} cm^2/s (450°C) [13] for silver. Dependence of the coefficients of diffusion in YBCO ceramics on the material density was previously reported for silver [5, 6] and cobalt [14]. Acceleration in the diffusion of zinc with an increase in the porosity of YBCO ceramics was also observed in this study (Fig. 1, curves *2* and *3*).

The density of ceramics also significantly influences the values of activation energy ε and preexponential factor D_0 of the aforementioned elements. In a low-density material, the activation energies typically amount to a few tenths of an electronvolt and the preexponential factors are on the order of 10^{-6}–10^{-10} cm^2/s, whereas analogous values in high-density ceramics amount to $\varepsilon = 2.3$–2.7 eV and $D_0 > 1$ cm^2/s. In low-density ceramics, a significant diffusion rate of 10^{-10}–10^{-9} cm^2/s at relatively low temperatures of 200–400°C was also observed for tin [9–11], indium [9–11], gold [15], cadmium [16], and sulfur [17, 18] (Fig. 2). In this temperature interval, these elements are also characterized by small activation energies ($\varepsilon < 0.6$ eV) and preexponential factors ($D_0 < 10^{-5}$ cm^2/s).

It should be noted that YBCO ceramics represent a rather inhomogeneous system comprising microcrystals (grains), intergranular (boundary) layers, and pores. This system features, besides the bulk (intragranular) diffusion mechanisms, accelerated migration via intergranular layers and by the pore surfaces. Since the accelerated migration mechanisms are characterized by high diffusion coefficients and small activation energies, the observed increase in the diffusion coefficient and a decrease in the activation energy with decreasing density of the ceramics is apparently evidence of the increasing role of the accelerated diffusion mechanisms in the system studied. In this context, the values of the diffusion coefficient and the activation energy for zinc in YBCO determined in our experiments indicate that zinc migrates predominantly via pores and intergranular layers in the ceramics.

The presence of several diffusion mechanisms makes a description based on the classical Fick equation incorrect. Nevertheless, almost all of the aforementioned (as well as the other) papers devoted to diffusion in YBCO ceramics employed the Fick equation. The diffusion coefficient determined in terms of this equation is only an effective average value. A detailed description of the process of diffusion in YBCO ceramics requires development of an adequate theoretical model which must take into account all significant features of diffusion is this system. Work in this direction is currently in progress.

Acknowledgments. The authors are grateful to V.A. Didik for his help in preparing the manuscript.

REFERENCES

1. Yu. G. Asadov, A. I. Baĭramov, K. M. Dzhafarov, and T. D. Dzhafarov, Sverkhprovodimost': Fiz., Khim., Tekh. **5** (9), 1732 (1992).
2. S. G. Ovchinnikov, Fiz. Tverd. Tela (St. Petersburg) **41** (4), 596 (1999) [Phys. Solid State **41**, 534 (1999)].
3. S. B. Ogale, M. Vedaways, G. S. T. Dendre, and S. M. Kanetkar, Appl. Phys. Lett. **61** (17), 2105 (1992).
4. J. L. Routbort, S. J. Rothman, Nan Chen, *et al.*, Phys. Rev. B **43** (7), 5489 (1991).
5. G. S. Kulikov, R. Sh. Malkoich, E. A. Skoryatina, *et al.*, Ferroelectrics **144**, 61 (1993).
6. A. H. Callaghan and L. W. Barr, in *Proceedings of the International Conference on Diffusion and Defects in Solids, DD-91, 1991*, Post Deadline Abstracts, P-06, p. 36.
7. D. Gupta, S. L. Shinde, and R. B. Laibowitz, in *High Temperature Superconducting Compounds II*, Ed. by S. H. Wang, A. Das Gupta, and R. B. Laibowitz (The Minerals, Metals, and Materials Society, Warrendale, 1990), p. 337.
8. Nan Chen, S. J. Rothman, and J. L. Routbort, J. Appl. Phys. **68** (5), 2523 (1990).
9. P. P. Gorbik, V. V. Dyakin, V. M. Ogenko, *et al.*, Dokl. Akad. Nauk Ukr. SSR, Ser. A, No. 7, 51 (1990).
10. V. N. Andreev, P. P. Gorbik, V. V. Dyakin, *et al.*, Sverkhprovodimost': Fiz., Khim., Tekh. **3** (8), 1654 (1990).
11. V. N. Alfeev, P. P. Gorbik, V. V. Dyakin, *et al.*, Solid State Commun. **77** (1), 49 (1991).
12. S. F. Gafarov, T. D. Dzhafarov, G. S. Kulikov, *et al.*, Pis'ma Zh. Tekh. Fiz. **15** (21), 66 (1989) [Sov. Tech. Phys. Lett. **15**, 858 (1989)].
13. M. V. Bakuntseva, M. A. Vasil'ev, P. P. Gorbik, *et al.*, Metallofizika **15** (6), 61 (1993).
14. G. S. Kulikov, R. Sh. Malkovich, E. A. Skoryatina, and V. P. Usacheva, Pis'ma Zh. Tekh. Fiz. **20** (6), 72 (1994) [Tech. Phys. Lett. **20**, 248 (1994)].
15. P. P. Gorbik, V. V. Dyakin, D. M. Ogenko, *et al.*, Dokl. Akad. Nauk Ukr. SSR, No. 1, 41 (1991).
16. B. V. Alekseenko, L. V. Galushko, P. P. Gorbik, *et al.*, Sverkhprovodimost': Fiz., Khim., Tekh. **5** (6), 1063 (1992).
17. V. N. Alfeev, P. P. Gorbik, V. V. Dyakin, *et al.*, Dokl. Akad. Nauk Ukr. SSR, No. 2, 38 (1991).
18. V. N. Alfeev, P. P. Gorbik, V. V. Dyakin, *et al.*, Sverkhprovodimost': Fiz., Khim., Tekh. **4** (7), 1320 (1991).

Translated by P. Pozdeev

Technical Physics Letters, Vol. 28, No. 5, 2002, pp. 430–433. Translated from Pis’ma v Zhurnal Tekhnicheskoĭ Fiziki, Vol. 28, No. 10, 2002, pp. 64–71.
Original Russian Text Copyright © 2002 by Magomedov.

On the Role of Vacancies in the Process of Self-Diffusion at Low Temperatures

M. N. Magomedov
Institute for Problems of Geothermics, Dagestan Scientific Center, Russian Academy of Sciences,
Makhachkala, Dagestan, Russia
e-mail: danterm@dinet.ru

Received November 19, 2001

Abstract—Expressions for the calculation of the parameters of self-diffusion in a crystal of simple substance at temperatures close to absolute zero are derived. It is established that, in “loose” crystal structures (with the first coordination number below 12), the amount of atoms involved in diffusion motion exceeds the number of vacant sites in the crystal lattice at $T = 0$ K. The results of calculations of the vacancy and diffusion parameters at $T = 0$ K for ten cryocrystals show that the phenomenon of “nonvacancy self-diffusion at $T = 0$ K” can take place only in bcc helium. *© 2002 MAIK “Nauka/Interperiodica”.*

The special features of atomic self-diffusion in crystals at temperatures T close to absolute zero were theoretically predicted long ago [1, 2]. However, many details of this process still remain unclear—in particular, the temperature and pressure dependence of the self-diffusion parameters and the role of “zero-point vacancies” in the process taking place at $T \approx 0$ K. The purpose of this study was to elucidate these questions.

Previously [3, 4], an expression for the bulk self-diffusion coefficient of a simple crystal was obtained in the following form:

$$D = D_0^* x; \quad D_0^* = f_{\rm c}(c/k_y^{1/3})^2 k_{\rm B}\Theta/8\pi\hbar, \qquad (1)$$

where $f_{\rm c}$ is the correlation factor determined by the crystal structure [5], $c = (6k_yV/\pi N)^{1/3}$ is the distance between centers of nearest neighbor atoms in a given crystal structure, k_y is the coefficient of atom packaging in the structure, V is the crystal volume, N is the number of atoms in the crystal, Θ is the Debye temperature, $k_{\rm B}$ is the Boltzmann constant, $\hbar$ is the Planck constant, and the function $x = x(V, T)$ represents the fraction of atoms occurring in a delocalized state (D-state), that is, possessing a kinetic energy above a certain threshold ($E_{\rm d}$), called the delocalization energy [6–8]:

$$\begin{aligned} x &= N_{\rm D}/N = (2/\pi^{1/2})\int_{E_{\rm d}/k_{\rm B}T}^{\infty} t^{1/2}\exp(-t)\,dt \\ &\cong 2(E_{\rm d}/\pi k_{\rm B}T)^{1/2}\exp(-E_{\rm d}/k_{\rm B}T). \end{aligned} \qquad (2)$$

An expression for the delocalization energy derived previously [6– 8] within the framework of the Einstein crystal model is as follows:

$$E_{\rm d} = (3/8k_y^{2/3})m f_y(3ck_{\rm B}\Theta/4\pi\hbar)^2, \qquad (3)$$

where m is the atomic mass and

$$\begin{gathered} f_y = (2/y)[1-\exp(-y)]/[1+\exp(-y)], \\ y = 3\Theta/4T. \end{gathered} \qquad (4)$$

The process of equilibrium self-diffusion can be described using the well-known formulas of equilibrium thermodynamics. The Gibbs free energy ($g_{\rm d}$), enthalpy ($h_{\rm d}$), entropy ($s_{\rm d}$), and volume ($v_{\rm d}$) of self-diffusion at arbitrary temperature and pressure (P) are given by the formulas [3, 4]

$$\begin{aligned} D &= D_0^*\exp(-g_{\rm d}/k_{\rm d}T) \\ &= D_0^*\exp(s_{\rm d}/k_{\rm d})\exp(-h_{\rm d}/k_{\rm d}T), \end{aligned} \qquad (5)$$

$$g_{\rm d} = E_{\rm d}[1-(k_{\rm B}T/2E_{\rm d})\ln(4E_{\rm d}/\pi k_{\rm B}T)], \qquad (6)$$

$$h_{\rm d} = E_{\rm d}\{1-t+(2-t)\eta+\alpha_P T[\gamma(2-t)-(2/3)]\}, \qquad (7)$$

$$\begin{aligned} s_{\rm d} &= E_{\rm d}\alpha_P[\gamma(2-t)-(2/3)] \\ &-(E_{\rm d}/T)[1-t+(2-t)\eta]+(k_{\rm B}/2)\ln(4E_{\rm d}/\pi k_{\rm B}T), \end{aligned} \qquad (8)$$

$$v_{\rm d} = (E_{\rm d}/B_T)[\gamma(2-t)-(2/3)], \qquad (9)$$

where $\gamma = -[d\ln(\Theta)/d\ln(V)]_T$ is the Grüneisen isothermal parameter, $\eta = -[d\ln(\Theta)/d\ln(T)]_V$, $\alpha_P = [d\ln(V)/dT]_P$ is the isobaric thermal expansion coefficient, $B_T = -[dP/d\ln(V)]_T$ is the isothermal bulk compression modulus, and

$$\begin{aligned} t &= -d\ln(f_y)/d\ln(y) \\ &= 1-\{2y\exp(-y)/[1-\exp(-2y)]\}. \end{aligned}$$

At high temperatures ($T \gg \Theta$), the value of f_y is close to unity, while the t and η values are negligibly small. In this case, the function $E_{\rm d}$ is independent of the temperature T and formulas (1) and (5) convert into well-

1063-7850/02/2805-0430$22.00 © 2002 MAIK “Nauka/Interperiodica”

known Arrhenius relationships [5]. Since the $\alpha_P T$ product is smaller than unity by an order of magnitude at temperatures up to the melting point, the E_d value virtually coincides with the enthalpy of self-diffusion h_d given by formula (7). The case of high temperatures was studied in detail previously [3, 4, 6–8], and the calculated parameters of diffusion showed good agreement with the experimental values. Here, this approach is used for determining the behavior of the parameters of self-diffusion in a simple crystal at low temperatures.

At $T < \Theta$, the functions f_y and t strongly vary with the temperature so that

$$f_y(0) = \lim_{T/\Theta \to 0}(f_y) = (8/3)\lim_{T/\Theta \to 0}(T/\Theta) = 0,$$
$$t(0) = \lim_{T/\Theta \to 0}(t) \tag{10}$$
$$= 1 - (6/4)\lim_{T/\Theta \to 0}[(\Theta/T)\exp(-3\Theta/4T)] = 1.$$

Another difficulty of the low-temperature case consists in that the functions $\Theta(T)$ and $\gamma(T)$ behave as [9, 10]

$$\Theta(t) \cong \Theta(0)(1 - \chi T^2),$$
$$\gamma(T) \cong \gamma(0)(1 + \chi T^2)/(1 - \chi T^2), \tag{11}$$

where $\Theta(0)$ and $\gamma(0)$ is the Debye temperature and the Grüneisen parameter calculated for the crystal at $T = 0$ K. According to [10], the function χ can be expressed as $\chi = (4/3)[\pi/\Theta(0)]^2$. This yields

$$\eta = 2\chi T^2[\Theta(0)/\Theta(T)] = 8(\pi T)^2/3\Theta(0)\Theta(T). \tag{12}$$

Taking into account that the thermal expansion coefficient at low temperatures behaves as $\alpha_P(T) \sim T^3$ [11, p. 225], which implies that $\alpha_P(0) = 0$, we obtain the following expressions for the parameters of self-diffusion at $T = 0$ K:

$$D = D_0^*(0)x(0);$$
$$D_0^*(0) = f_c[c(0)/k_y^{1/3}]^2 k_B\Theta(0)/8\pi\hbar, \tag{13}$$

$$x(0) = N_D(0)/N$$
$$= (2/\pi^{1/2})\int_{M_d}^{\infty} t^{1/2}\exp(-t)dt \cong 2(M_d/\pi)^{1/2}\exp(-M_d), \tag{14}$$

$$\lim_{T/\Theta \to 0}(g_d/k_BT) = M_d - 0.5\ln(4M_d/\pi), \tag{15}$$

$$\lim_{T/\Theta \to 0}[h_d/(k_BT)^3]$$
$$= M_d\lim_{T/\Theta \to 0}[\eta/(k_BT)^2] = 8\pi^2 M_d/3[k_B\Theta(0)]^2, \tag{16}$$

$$s_d(0)/k_B = -M_d + 0.5\ln(4M_d/\pi), \tag{17}$$

$$\lim_{T/\Theta \to 0}(v_dB_T/k_BT) = M_d[\gamma(0) - 2/3], \tag{18}$$

where the parameter M_d represents the limiting ratio

$$M_d = \lim_{T/\Theta \to 0}(E_d/k_BT) = 8E_{d0}/3k_B\Theta(0), \tag{19}$$

$$E_{d0} = (3/8k_y^{2/3})m[3c(0)k_B\Theta(0)/4\pi\hbar]^2. \tag{20}$$

Thus, the self-diffusion coefficient is nonzero even at $T = 0$ K. This effect, reflecting the presence of "zero-point oscillations," was predicted in [1, 2]. In order to elucidate the role of vacancies in the process of self-diffusion at $T = 0$ K, let us compare the number of atoms involved in this process (i.e., occurring in the D state) relative to the number of vacant sites in the crystal lattice at $T = 0$ K.

As demonstrated recently [12], the probability of formation of "zero-point vacancies" is determined by the relationship

$$\phi(0) = (2/\pi^{1/2})\int_{M_v}^{\infty}\exp(-t^2)dt$$
$$\cong (\pi M_v)^{-1/2}\exp(-M_v). \tag{21}$$

Here, the parameter M_v represents the limiting ratio

$$M_v = \lim_{T/\Theta \to 0}(E_v/k_BT) = 8E_{v0}/3k_B\Theta(0) \tag{22}$$

and is related to the M_d value as

$$M_d/M_v = \lambda = E_{d0}/E_{v0} = 3k_n/2\pi^2 k_y^{2/3}, \tag{23}$$

where k_n is the first coordination number of the given crystal lattice.

Proceeding from the above relationships, one can derive the following relation between the number of atoms if the D state and the number of zero-point vacancies in the crystal lattice at $T = 0$ K:

$$x(0)/\phi(0)$$
$$= \exp[-M_v(\lambda - 1) + 0.5\ln(4\lambda M_v^2)] \cong N_d(0)/N_v(0). \tag{24}$$

As can be seen, this expression reaches a maximum when $M_v = M_v(\max) = (\lambda - 1)^{-1}$. For $k_n < 12$, there is an interval of M_v values in which $x(0)/\phi(0) \geq 1$ or $N_d(0)/N_v(0) \geq 1$.

Table 1 presents the parameters of the "nonvacancy self-diffusion" process (for which $N_d(0) \geq N_v(0)$) calculated for various crystal lattice structures. As is evident from these data, the self-diffusion at $T = 0$ K in close-packed structures (fcc, hcp) always proceeds by the vacancy mechanism (since $N_d(0) < N_v(0)$). In less dense (i.e., "loose") structures, a situation is possible (for a certain M_v) whereby the self-diffusion can proceed both by the vacancy mechanism and by alternative (nonvacancy) pathways, for example, by nearest neighbor exchange without forming vacancies, by circular atomic transfer, etc. (see, e.g. [5]). As can be seen from Table 1, loosening of the structure leads to expansion of this M_v region ($N_d/N_v \geq 1$) and to an increase in the

Table 1. The vacancy and diffusion parameters calculated for various structures

Structure	k_n	k_y	λ	M_v(max)	$[N_d(0)/N_v(0)]_{max}$	$M_v(N_d/N_v \geq 1)$
fcc, hcp	12	0.7405	2.2285	0.8140	0.8941	No
bct*	10	0.6981	1.9315	1.07335	1.0977	0.675–1.604
bcc	8	0.6802	1.5722	1.7476	1.6123	0.545–4.052
scp**	6	0.5236	1.4039	2.4760	2.1585	0.521–6.928
Diamond	4	0.3401	1.2479	4.0345	3.3160	0.508–13.842

Notes: * Body-centered tetragonal; ** simple cubic packing; M_v(max) is the M_v value at which the ratio (24) reaches a maximum; $[N_d(0)/N_v(0)]_{max}$ is the maximum of ratio (24); $M_v(N_d/N_v \geq 1)$ is the interval of M_v values for which $N_d(0) \geq N_v(0)$.

Table 2. Experimental values of the free volume V and Debye temperature Θ at $T = 0$ K and the vacancy and diffusion parameters calculated using these values for various crystals by formulas (13)–(23)

Substance	Structure	V, cm^3/mol	$\Theta(0)$, K	E_{v0}, K	M_v	$\phi(0)$	E_{d0}, K	M_d	$x(0)$	$N_d(0)/N_v(0)$	$D(0)$, cm^2/s
^{3}He	hcp	11.42	128.2 [14]	106.7	2.22	4×10^{-2}	237.9	4.95	2×10^{-2}	0.433	1.02×10^{-5}
		19.00	40.0 [14]	14.6	0.97	0.216	32.5	2.17	0.190	0.879	4.76×10^{-5}
	bcc	19.00	34.0 [14]	14.9	1.17	0.161	23.5	1.84	0.243	1.503	4.80×10^{-5}
		24.00	19.0 [14]	5.5	0.77	0.300	8.6	1.20	0.372	1.239	4.80×10^{-5}
^{4}He	hcp	12.00	100.0 [14]	89.5	2.39	3×10^{-2}	199.5	5.32	1.3×10^{-2}	0.380	0.59×10^{-5}
		21.00	20.0 [14]	5.2	0.69	0.339	11.6	1.55	0.299	0.883	4.00×10^{-5}
	bcc	20.927	21.2 [14]	8.3	1.04	0.196	13.0	1.63	0.282	1.438	3.71×10^{-5}
		21.028	20.8 [14]	8.0	1.02	0.201	12.5	1.61	0.287	1.429	3.71×10^{-5}
p-H$_2$	hcp	9.00	534.0 [15]	1053.6	5.26	10^{-3}	2348.0	11.73	3.1×10^{-5}	2.5×10^{-2}	6.33×10^{-8}
		23.40	94.0 [15]	61.7	1.75	7×10^{-2}	137.6	3.90	4.5×10^{-2}	0.608	3.04×10^{-5}
o-D$_2$	hcp	9.00	370.9 [15]	1016.6	7.31	10^{-4}	2265.5	16.29	4.0×10^{-7}	2.8×10^{-3}	5.40×10^{-10}
		20.40	87.0 [15]	96.5	2.96	2×10^{-2}	215.1	6.59	4.0×10^{-3}	0.233	2.26×10^{-6}
Ne	fcc	13.53	74.6 [15]	272.3	9.73	10^{-5}	606.8	21.69	10^{-9}	2×10^{-4}	7.4×10^{-13}
Ar	fcc	22.57	93.3 [15]	1185.9	33.89	10^{-16}	2642.7	75.53	10^{-32}	8×10^{-17}	10^{-35}
Kr	fcc	27.13	71.7 [15]	1650.9	61.40	10^{-28}	3679.0	136.83	10^{-59}	3×10^{-31}	10^{-62}
Xe	fcc	34.55	64.0 [15]	2435.9	101.5	10^{-46}	5428.4	226.18	10^{-97}	2×10^{-52}	10^{-100}
^{14}N$_2$	fcc	27.128	83.5 [15]	752.6	24.04	4×10^{-12}	1677.2	53.56	4.5×10^{-23}	1.1×10^{-11}	3×10^{-26}
^{15}N$_2$	fcc	27.027	81.0 [15]	756.9	24.92	2×10^{-12}	1686.7	55.53	6.4×10^{-24}	3.8×10^{-12}	4×10^{-27}
Li	bcc	12.806	344.0 [16]	2720.6	21.09	8×10^{-11}	4277.3	33.16	2.6×10^{-14}	3.0×10^{-4}	4×10^{-17}
	hcp	12.806	344.0 [16]	1813.7	14.06	10^{-7}	4041.9	31.33	1.6×10^{-13}	1.3×10^{-6}	3×10^{-16}

$[N_d(0)/N_v(0)]_{max}$ value. Note that an analogous behavior ($N_d > N_v$) is observed at elevated temperatures in a gas–liquid argon phase [13], the structure of which can be represented by a virtual lattice model with $N + N_v$ cells in which N_d atoms are delocalized (i.e., involved in the translational motion over the entire system volume), while the remaining $N - N_d$ atoms are localized in the virtual lattice cells and perform oscillation about their equilibrium centers.

Table 2 summarizes the results of calculation of the vacancy and diffusion parameters for ten substances. As can be seen, significant $\phi(0)$ and $x(0)$ values are observed only in helium. The M_v and M_d values increase, while $\phi(0)$ and $x(0)$ values decrease, with increasing atomic mass. Note also that, for the crystals presented in Table 2, the calculated values of E_{v0} and E_{d0} agree well with experimental estimates of the energies for monovacancy formation and the self-diffusion activation energies in the crystals at $T \ll \Theta$. The nonvacancy self-diffusion at $T = 0$ K (i.e., a situation whereby $N_d(0) \geq N_v(0)$) is realized only in a bcc He structure). No other cryocrystal nor bcc Li exhibit this effect. The phenomenon of "nonvacancy self-diffusion at $T = 0$ K" consists in that, under these conditions, the transfer of atoms in bcc He via the crystal volume is energetically more favorable without forming vacancies in the lattice. In this case, the enthalpy and free volume of self-diffusion become equal to zero (see formulas (16) and (18)).

The solid phase of helium at $T = 0$ K represents (as noted previously in [1, 2, 14–16]) a certain intermediate state of the substance between the classical solid and liquid. The nature of this intermediate sate is determined by a significant role of the zero-point oscillations in helium in comparison to that in other substances studied (Table 2). This may account for the phenomenon of nonvacancy self-diffusion at $T = 0$ K in bcc helium, which was also found at high temperatures in the lattice model of a gas-liquid phase of argon [13].

Acknowledgments. The author is grateful to Prof. K.M. Magomedov, K.N. Magomedov, and Z.M. Surkhaeva for their help in this work.

REFERENCES

1. A. F. Andreev and I. M. Lifshits, Zh. Éksp. Teor. Fiz. **56** (6), 2057 (1969) [Sov. Phys. JETP **29**, 1107 (1969)].
2. A. F. Andreev, Usp. Fiz. Nauk **118** (2), 251 (1976) [Sov. Phys. Usp. **19**, 137 (1976)].
3. M. N. Magomedov, Fiz. Met. Metalloved. **80** (4), 36 (1995).
4. M. N. Magomedov, Izv. Akad. Nauk, Met., No. 5, 21 (1996).
5. J. R. Manning, *Diffusion Kinetics for Atoms in Crystals* (D. van Nostrand, Toronto, 1968).
6. M. N. Magomedov, Fiz. Met. Metalloved. **77** (10), 13 (1992).
7. M. N. Magomedov, Zh. Fiz. Khim. **67** (4), 669 (1993).
8. M. N. Magomedov, Teplofiz. Vys. Temp. **31** (5), 731 (1993).
9. *Problems in Solid State Physics*, Ed. by H. J. Goldsmid (Academic, New York, 1968).
10. M. N. Magomedov, Zh. Fiz. Khim. **61** (4), 1003 (1987).
11. L. D. Landau and E. M. Lifshitz, *Course of Theoretical Physics*, Vol. 5: *Statistical Physics* (Nauka, Moscow, 1976; Pergamon, Oxford, 1980), Part 1.
12. M. N. Magomedov, Pis'ma Zh. Tekh. Fiz. **27** (18), 36 (2001) [Tech. Phys. Lett. **27**, 773 (2001)].
13. M. N. Magomedov, Teplofiz. Vys. Temp. **39** (4), 559 (2001).
14. S. B. Trickey, Q. P. Kirk, and E. D. Adams, Rev. Mod. Phys. **44** (4), 668 (1972).
15. *Cryocrystals*, Ed. by B. I. Verkin and A. F. Prikhod'ko (Naukova Dumka, Kiev, 1983).
16. C. Kittel, *Introduction to Solid State Physics* (Wiley, New York, 1976; Nauka, Moscow, 1978).

Translated by P. Pozdeev

Technical Physics Letters, Vol. 28, No. 5, 2002, pp. 434–436. Translated from Pis'ma v Zhurnal Tekhnicheskoĭ Fiziki, Vol. 28, No. 10, 2002, pp. 72–77.
Original Russian Text Copyright © 2002 by Tonkikh, Egorov, Polyakov, Cirlin, Kryzhanovskaya, Sizov, Ustinov.

Photoluminescence in the 1.55 μm Wavelength Range in the InGaAs/GaAs System with Quantum Dots and Wells

**A. A. Tonkikh[a], V. A. Egorov[a], N. K. Polyakov[a], G. E. Cirlin[b],
N. V. Kryzhanovskaya[b], D. S. Sizov[b], and V. M. Ustinov[b]**
[a] *Institute of Analytical Instrument Building, Russian Academy of Sciences, St. Petersburg, Russia*
[b] *Ioffe Physicotechnical Institute, Russian Academy of Sciences, St. Petersburg, 194021 Russia*

Received December 20, 2001

Abstract—It is demonstrated that longwave room-temperature photoluminescence (up to 1.65 μm) can be obtained using InGaAs/GaAs heterostructures of two types grown by low-temperature molecular beam epitaxy: (i) with InAs quantum dots formed at a low growth velocity and (ii) with an $In_{0.5}Ga_{0.5}As$ quantum well grown in excess of the group III elements. *© 2002 MAIK “Nauka/Interperiodica”.*

Creating laser diodes emitting at a wavelength of 1.55 μm (corresponding to a minimum signal absorption) is important for implementing these devices in fiber optic communication systems. Several approaches to solving this problem have been suggested up to now, which are based mostly on using heterostructures of $A^{III}B^{V}$ semiconductor compounds grown on indium phosphide substrates. The traditional approach consists in using the InGaAsP/InP system with quantum wells (QWs). Recently, Li *et al.* [1] reported on the photoluminescence at 1.55 μm in a structure with InAs quantum dots (QDs) grown on a buffer layer of InAlAs possessing a lattice parameter matched with that of the InP substrate. However, such structures possess a number of significant disadvantages, including low temperature stability, difficulties in creating vertical-cavity surface-emitting lasers, and a relatively high cost of InP substrates.

There are alternative technologies employing substrates other than InP. For example, Harmand *et al.* [2] used GaAsSbN QWs grown on GaAs substrates and succeeded in reaching a wavelength range of 1.3 and even 1.55 μm using materials with a nitrogen concentration of 1 and 2.5%, respectively. Another approach consists in doping a semiconductor material with rare-earth elements: Shen *et al.* [3] demonstrated electroluminescence at 1.55 μm from erbium-doped GaN.

Despite these solutions, it is of considerable interest to search for new ways of obtaining structures applicable in electrooptical devices. It was demonstrated [4] that longwave (~1.7 μm) radiation can be obtained using structures with laterally associated quantum dots (LAQDs) of the InAs/GaAs system grown at a low (~320–350°C) substrate temperature. Here we report on a modification of this method, employing InAs deposition at a low rate. This allows the crystallographic quality of the structure to be increased while retaining emission in the required longwave range (1.55 μm). For comparison, we studied an alternative method of reaching the same wavelength range based on the growth of $In_{05}Ga_{05}As$ QWs at low substrate temperatures and low deposition rates under conditions of excess group III element.

The sample structures were grown in a molecular beam epitaxy (MBE) system of the EP1203 type using semi-insulating single crystal GaAs(100) substrates. In samples of the first type, the active region was formed by depositing an InAs film with an effective thickness of three monolayers (ML) at a low InAs deposition rate (0.01 ML/s) and an initial substrate temperature of 350°C. The deposition of InAs QDs was monitored by measuring and analyzing the reflection high-energy electron diffraction (RHEED) patterns [5]. The observed dynamics of RHEED patterns showed that a sharp transition from linear to point diffraction (characteristic of the Stranski–Krastanov growth mechanism) corresponding to the onset of an island growth takes place after deposition of the InAs layer with a thickness of about 1.8 ML. In heterostructures of the second type, the active region represented an $In_{05}Ga_{05}As$ QW with a thickness varying in various samples from 20 to 50 Å. A characteristic feature of growth in this system was that the RHEED patterns revealed no transition to the island growth, thus evidencing growth in a planar regime. The substrate temperature during the active region deposition was 350°C. This region was grown in the presence of excess group III elements: the residual pressure of As_4 vapors was on a level of 5×10^{-7} Pa. In order to prevent indium evaporation from the InGaAs layer, a 20-Å-thick GaAs layer was grown in all structures immediately after the active region formation (at the same substrate temperature). Then the substrate temperature was increased and the main 200-Å-thick GaAs layer was grown.

In order to eliminate the transport of nonequilibrium carriers into the near-surface region and into the substrate in the course of optical measurements, the active region was bounded from both sides by short-period superlattices $Al_{0.25}Ga_{0.75}As$/GaAs (5 pairs, 25 Å/25 Å). This was followed by a 5-nm-thick GaAs layer. The buffer layer, superlattices, and uppermost GaAs layers were deposited at a substrate temperature of 600°C. The photoluminescence (PL) was excited by an Ar^+ laser (λ = 514.5 nm; beam power density, ~100 W/cm^2). The emission was measured with a cooled Ge photodiode.

Figure 1 shows the PL spectra of two structures with QDs grown by low-temperature MBE. The two samples differed in the technology of InAs layer deposition. In the first case (spectrum *1*), the substrate temperature during InAs layer growth was decreased from 350 to 320°C, whereas in the second case (spectrum *2*), the substrate temperature during InAs layer growth was maintained constant (350°C). Both spectra clearly display two emission bands. The first band at 1.15 eV corresponds to the photoluminescence from small-size QDs. An analysis of the RHEED pattern confirms the QD formation. Note that QDs of this type are usually obtained by depositing InAs at a substrate temperature of 480–500°C [6]. The second (longwave) emission band corresponds to the emission from LAQDs described previously [4]. The proposed modification of the low-temperature MBE technique allowed us to obtain structures with the room-temperature longwave PL peak intensity comparable to that of the usual QDs. In our opinion, this is achieved due to a low (~0.01 ML/s) growth rate, resulting in a higher crystallographic quality of the structure.

Figure 2 shows the PL spectra of three structures with QWs grown at 350°C, differing by the thickness of the InGaAs layer (20, 30, and 50 Å in samples 1–3, respectively). The growth of these layers was monitored by the RHEED method. In all cases, the RHEED patterns retained the line character; the intensity of lines corresponding to the main reflections decreased, and the surface exhibited a reconstruction changing from (2 × 2) to (3 × 1). This reconstruction probably corresponds to the formation of a corrugated surface structure typical of the heteroepitaxial growth in the InGaAs/GaAs system [7].

During deposition of a 20-Å-thick GaAs layer onto the InGaAs film at the same substrate temperature, samples 1 and 2 showed a diffraction pattern typical of the facet growth. We attribute this fact to the appearance of InGaAs islands in the surface layer. This assumption is confirmed by the presence of a PL peak in the region of 1.15 eV. Sample 3 also showed a broad PL band in this region, but the RHEED patterns of this sample did not reveal the characteristic transition from layer to island growth. This probably explains the fact that the PL intensity in the shortwave peak is lower than that in the longwave peak. An interesting feature of samples 2 and 3 is the presence of a longwave peak in the region of 1.6 μm. We assign this peak to the structures appearing as a result of the surface-stress-induced transformation of the initial $In_{0.5}Ga_{0.5}As$ layer.

Thus, we have demonstrated the possibility of obtaining PL in the 1.5–1.65 μm wavelength range using heterostructures with QDs and QWs in the InGaAs/GaAs system grown by MBE with low-temperature deposition of the active region. The study of these structures by transmission electron microscopy is in progress.

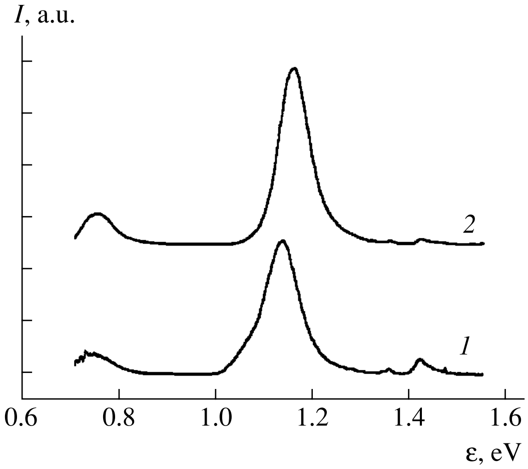

Fig. 1. The room-temperature PL spectra of two heterostructures with 3-ML InAs quantum dots grown by low-rate MBE with the substrate temperature (*1*) decreased from 350 to 320°C and (*2*) maintained constant at 350°C.

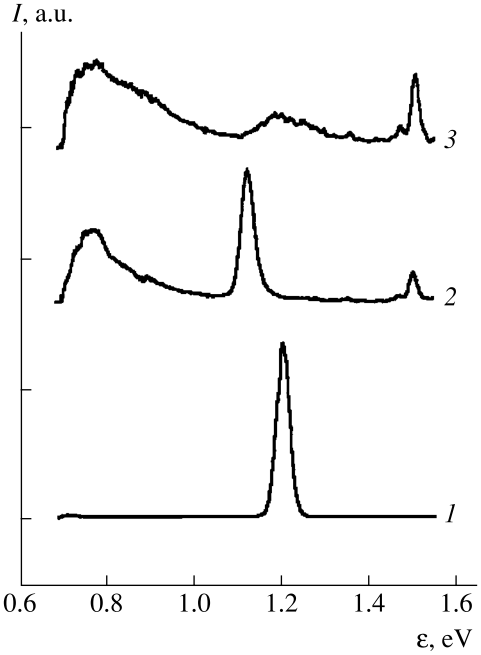

Fig. 2. The spectra of PL at 77 K for heterostructures with $In_{0.5}Ga_{0.5}As$ quantum wells of various thicknesses: (*1*) 20, (*2*) 30, and (*3*) 50 Å.

Acknowledgments. V.A.E. and A.A.T. are grateful to the St. Petersburg City Administration for support (Young Scientist Program, grant nos. MO1-2.4K-494 and MO1-2.4D-495). This study was also partly supported by the Federal Scientific Program "Physics of Solid-State Structures."

REFERENCES

1. Y. F. Li, X. L. Ye, B. Xu, *et al.*, J. Cryst. Growth **218**, 451 (2000).
2. J. C. Harmand, G. Ungaro, J. Ramos, *et al.*, J. Cryst. Growth **227-228**, 553 (2001).
3. H. Shen, J. Pamulapati, M. Taysing, *et al.*, Solid-State Electron. **43**, 1231 (1999).
4. M. V. Maximov, A. F. Tsatsul'nikov, B. V. Volovik, *et al.*, Appl. Phys. Lett. **75** (16), 2347 (1999).
5. V. N. Petrov, V. N. Demidov, N. P. Korneeva, *et al.*, Zh. Tekh. Fiz. **70** (5), 97 (2000) [Tech. Phys. **45**, 618 (2000)].
6. G. É. Tsyrlin, N. P. Korneeva, V. N. Demidov, *et al.*, Fiz. Tekh. Poluprovodn. (St. Petersburg) **31** (10), 1230 (1997) [Semiconductors **31**, 1057 (1997)].
7. G. M. Guryanov, G. E. Cirlin, A. O. Golubok, *et al.*, Surf. Sci. **352–354**, 646 (1996).

Translated by P. Pozdeev

Technical Physics Letters, Vol. 28, No. 5, 2002, pp. 437–438. Translated from Pis'ma v Zhurnal Tekhnicheskoĭ Fiziki, Vol. 28, No. 10, 2002, pp. 78–82.
Original Russian Text Copyright © 2002 by Gutkin, Ovid'ko, Skiba.

Changes in Grain Boundary Misorientation Caused by Emission of Dislocation Pairs

M. Yu. Gutkin, I. A. Ovid'ko, and N. V. Skiba
Institute of Problems of Mechanical Engineering, Russian Academy of Sciences, St. Petersburg, Russia
e-mail: ovidko@def.ipme.ru

Received October 11, 2001

Abstract—A new geometric micromechanism responsible for changes in the misorientation of grain boundaries in the course of (super)plastic deformation is proposed. According to this, the misorientation changes as a result of the motion of grain-boundary disclinations accompanied by the emission of lattice dislocation pairs. Within the framework of the proposed model, the energy characteristics of the motion of grain-boundary disclinations are calculated. *© 2002 MAIK "Nauka/Interperiodica".*

The behavior of grain-boundary disclinations (GBDs) significantly influences the properties of grain boundaries (GBs) in solids (see, e.g., [1–7]). In particular, the experimentally observed changes in the misorientation of GBs in the course of plastic deformation of fine-grained polycrystals and nanocrystalline materials [8, 9] are usually related to the motion of GBDs induced by the absorption of lattice dislocations at GBs [2–4, 7]. In the general case, however, the motion of disclinations in GBs takes place not only as a result of the absorption of lattice dislocations, but upon the emission of such dislocations as well.

Below we propose and theoretically describe a new geometric micromechanism of changes in the misorientation of GBs in the course of (super)plastic deformation. According to this model, the GB misorientation changes as a result of the motion of GBDs related to the emission of lattice dislocation pairs into the neighboring grains.

According to the concepts of the theory of defect structure of GBs [1–7], the GBDs represent linear defects separating the regions of GBs with different misorientation values. Then, time variation in the GB misorientation is described as the motion of GBDs [2, 3].

Within the framework of the model developed in this paper, the elementary event of transfer of a wedge GBD with a power ω over a distance l is accompanied by the emission of a pair of lattice dislocations with the Burgers vectors $\mathbf{b}_1$ and $\mathbf{b}_2$ (where $\mathbf{b}_1 + \mathbf{b}_2 = \mathbf{b}$ and $b = 2l\tan(\omega/2)$) into the adjacent grains (Fig. 1). The sequential emission of such dislocation pairs can provide for a change in the misorientation over arbitrarily large GB regions and, in particular, for the rotation of the grain as a whole.

Let us consider the energy characteristics of the proposed micromechanism of GBD motion. For example, consider the transfer of a GBD with the power ω in a total field of the screening stresses of another (immobile) GBD with the power –ω and the stresses created by an external mechanical load (Fig. 1). The results of the theoretical analysis of a particular configuration of defects depicted in Fig. 1 can be readily generalized to other disclination and dislocation configurations.

According to the results of our calculations (a complete presentation is outside the scope of this brief communication), the energy difference ΔW of the given defect configuration (Fig. 1) after and before GBD transfer is determined by the following expression:

$$\begin{aligned}
\Delta W = {} & \frac{Db_1^2}{2}\left\{\left(1+\frac{b_2^2}{b_1^2}\right)\left(\ln\frac{R}{r_0}+1\right)-\frac{b^2}{b_1^2}\right. \\
& \left.+\frac{\omega^2 L_1^2}{b_1^2}\left[\ln\frac{R}{L_1}+\frac{1}{2}-\frac{L^2}{L_1^2}\left(\ln\frac{R}{L}+\frac{1}{2}\right)\right]\right\} \\
& -\frac{1}{2}\sigma_y p(b_1\sin 2\phi_1 + b_2\sin 2\phi_2) \\
& +\frac{1}{2}D\omega b_1\cos\phi_1\left(L\ln\frac{R^2+L^2+2RL\sin\phi_1}{p^2+L^2+2pL\sin\phi_1}\right. \\
& \left.-l\ln\frac{R^2+l^2+2Rl\sin\phi_1}{p^2+l^2+2pl\sin\phi_1}\right) \qquad (1) \\
& +\frac{1}{2}D\omega b_2\cos\phi_2\left(L\ln\frac{R^2+L^2+2RL\sin\phi_2}{p^2+L^2+2pL\sin\phi_2}\right. \\
& \left.-l\ln\frac{R^2+l^2+2Rl\sin\phi_2}{p^2+l^2+2pl\sin\phi_2}\right) \\
& +\frac{1}{2}Db_1b_2\cos(\phi_1+\phi_2)\ln\frac{p^2+R^2+2pR\cos(\phi_1+\phi_2)}{2ep^2[1+\cos(\phi_1+\phi_2)]} \\
& +\frac{1}{2}Db_1b_2\frac{R^2+p^2+2Rp[\cos(\phi_1+\phi_2)-\sin^2(\phi_1+\phi_2)]}{R^2+p^2+2Rp\cos(\phi_1+\phi_2)}.
\end{aligned}$$

1063-7850/02/2805-0437$22.00 © 2002 MAIK "Nauka/Interperiodica"

Here, $D = G/[2\pi(1 - \nu)]$, G is the shear modulus, ν is the Poisson coefficient, L is the distance between disclinations (disclination dipole arm), $L_1 = L - l$, r_0 is the radius of the dislocation core, σ_y is the acting normal external stress, ϕ_1 and ϕ_2 are the angles between the normal to the boundary and the slip planes of the first and second dislocation, R is the radius of screening of the defect-induced stress field, and p is the path traveled by each dislocation upon emission (Fig. 1).

An analysis of formula (1) shows that there are sufficiently wide domains of parameters of the defect structure (Fig. 1) in which $\Delta W < 0$; that is, the process of GBD transfer is energetically favorable. This conclusion is illustrated in Fig. 2, presenting the plots of ΔW (expressed in Gb^2 units) versus disclination dipole arm L for various angles ϕ_1 and ϕ_2 at which the dislocations are emitted (for the following set of characteristic parameters of the given defect configuration: $R = 10^5 b$, $\omega = 0.1$, $p = 1b$, $\sigma_y = 10^{-3}\,G$). The data of Fig. 2 show that the transfer of a GBD (Fig. 1) becomes energetically favorable beginning with a certain value of the disclination dipole arm L. This L value depends on the dislocation emission angles ϕ_1 and ϕ_2. As can be seen from Fig. 2, the process in the given defect configuration is energetically favorable at $L = 20b$ for the angles $\phi_1 = \phi_2 = 2°$, and at $L = 65b$ for $\phi_1 = \phi_2 = 45°$. Therefore, the smaller the angles ϕ_1 and ϕ_2, the shorter the disclination dipole arm L at which the transfer of GBDs becomes energetically favorable.

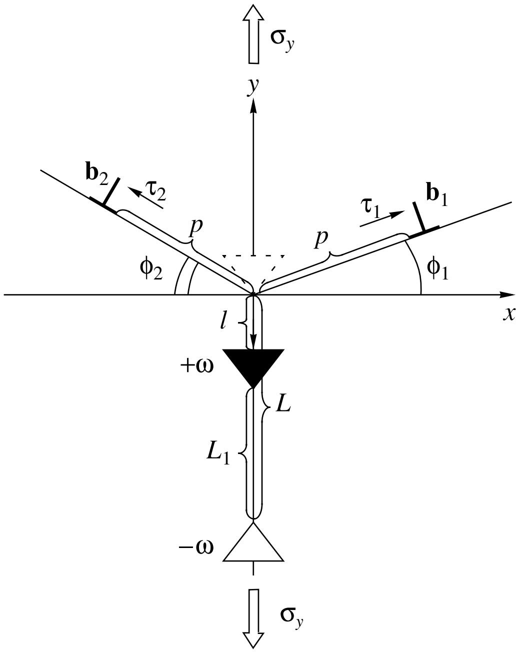

Fig. 1. Schematic diagram illustrating emission of a pair of lattice dislocations accompanying the transfer of a grain-boundary disclination.

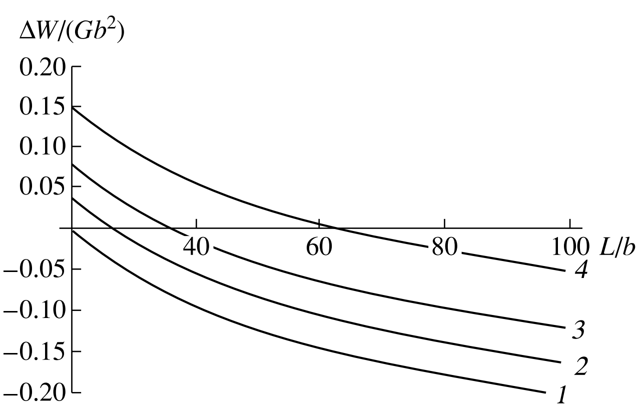

Fig. 2. The plots of ΔW versus L for various emission angles of a dislocation pair: $\phi_1 = 2°$ (*1*), 20° (*2*), 30° (*3*), 45° (*4*); $\phi_2 = 2°$ (*1*), 30° (*2*), 40° (*3*), 45° (*4*).

Thus, the transfer of GBDs accompanied by the emission of lattice dislocation pairs (Fig. 1) offers an effective geometric micromechanism for changing the misorientation of GBs in the course of plastic deformation in fine-grained polycrystals and nanocrystalline materials. The notions about GB misorientation variation related to dislocation pair emission naturally explain the experimental data [8, 9] on the rotation of grains during superplastic deformation. At the same time, further theoretical and experimental investigations are necessary in order to determine the role of the proposed geometric micromechanism in changing the GB misorientation in real plastically deformed materials.

Acknowledgments. This study was supported by the Russian Foundation for Basic Research (project no. 01-02-16853), the INTAS Foundation (grant no. 99-01216), Volkswagen Foundation (project 05019225), and the European Office of the US Naval Research Laboratory (grant N00014-01-1-1020).

REFERENCES

1. V. V. Rybin, A. N. Vergazov, and V. A. Likhachev, Fiz. Met. Metalloved. **37**, 620 (1974).
2. V. V. Rybin, *Large Plastic Deformations and Fracture of Metals* (Metallurgiya, Moscow, 1986).
3. V. I. Vladimirov and A. E. Romanov, *Disclinations in Crystals* (Nauka, Leningrad, 1986).
4. A. A. Nazarov, A. E. Romanov, and R. Z. Valiev, Acta Metall. Mater. **41**, 1033 (1993).
5. M. Yu. Gutkin and I. A. Ovid’ko, Philos. Mag. A **74**, 561 (1994).
6. V. V. Rybin and A. A. Zisman, Probl. Prochn. **3**, 70 (1985).
7. M. Yu. Gutkin and I. A. Ovid’ko, *Defects and Mechanisms of Plasticity in Nanostructured and Noncrystalline Materials* (Yanus, St. Petersburg, 2001).
8. O. A. Kaĭbyshev and R. Z. Valiev, *Grain Boundaries and Properties of Metals* (Metallurgiya, Moscow, 1987).
9. M. G. Zelin and A. K. Mukherjee, Mater. Sci. Eng. A **208**, 210 (1996).

Translated by P. Pozdeev

Technical Physics Letters, Vol. 28, No. 5, 2002, pp. 439–440. Translated from Pis'ma v Zhurnal Tekhnicheskoĭ Fiziki, Vol. 28, No. 10, 2002, pp. 83–87.
Original Russian Text Copyright © 2002 by Karachinov.

Cathodic Localization of Metal Coatings on Silicon Carbide Crystals

V. A. Karachinov

Novgorod State University, Velikiĭ Novgorod, Russia

Received January 14, 2002

Abstract—Experimental data on the electrical properties of metal contacts fabricated by depositing copper from a porous electrode onto the surface of silicon carbide crystals are reported. *© 2002 MAIK "Nauka/Interperiodica".*

Introduction. In some technical applications, silicon carbide is employed with metal coatings performing the functions of electrodes, ohmic contacts, Schottky barriers, or protective layers [1–5]. As is known, such structures of preset shapes and dimensions are fabricated within the framework of SiC planar technology using processes combining various methods of vacuum deposition and photolithography. However, the electrochemical methods of SiC surface treatment can also be of interest: using these techniques, it is possible to form oxide and porous layers at room temperature without vacuum facilities and to deposit some metals without an electroplating bath [6, 7].

Below we report on the results of experimental investigation of the morphology and electric properties of metal–SiC structures fabricated by depositing copper from a porous electrode.

Experimental. The local deposition of copper was studied in an experimental setup comprising a controlled current generator and a porous electrode (anode). The output voltage could be varied in an interval from 0 to 12 V. The experiments were performed with porous electrodes of a cylindrical shape, made of fiber materials saturated with a copper-containing electrolyte of standard composition [8].

The initial materials were single crystal SiC wafers and bulk samples of the 6H polytype, with natural faces and surfaces upon mechanical polishing and etching in melted KOH, as well as sintered polycrystalline samples. The uncompensated (excess) donor concentration in SiC crystals was $N_d - N_a \approx 5 \times 10^{17}$–$5 \times 10^{18}$ cm^{-3}, and the dislocation density was $N_D \cong 1 \times 10^4$–5×10^5 cm^{-2}.

The features of surface morphology of the deposited copper layers were studied by optical methods (a metallographic TV microscope with computer image processing and an optical interferometer) and by scanning electron microscopy (SEM) using a Tesla BS-340 electron microscope in the secondary-electron imaging mode. The electrical properties of the Cu–SiC system were studied using test resistor structures with a contact area of $S \approx 500$ μm^2 and thermoresistors of various shapes fabricated by an erosive replication technique [9]. These samples were used to measure the current–voltage (I–U) characteristics and their temperature variation.

The results of optical examination showed that copper films can be applied onto SiC substrates of any crystallographic orientation. The local character of deposition provides for the obtaining of patterns with both extended elements and separate islands (for example with thickening in the central part in the form of either smooth transition or terrace morphology). The average metal deposition rate was ~0.8 μm/min, as determined by traditional parameters (current density, electrolyte concentration) and by the velocity of porous electrode translation. The latter factor is related to the restoration of copper lost from the gliding electrolyte layer. Electrode motion favors release of gas bubbles from the SiC substrate surface.

The initial crystal surface condition and the methods of preparation (prehistory) influenced the initial stage of the electrodeposition process. According to the SEM data, the formation of copper nuclei took place predominantly on the active centers of the SiC substrate surface (scratches, cleavages, microroughnesses, etc.). A unidirectional electrode motion sometimes led to the surface texture formation [10].

Results and discussion. Freshly deposited copper films exhibited a bright surface and possessed good adhesion to the substrate. The resistivity of these coatings (1.64–1.78 μΩ cm) differed only slightly from the values typical of the deposits obtained in a electroplating bath [11].

As is known, copper is rarely used as a separate coating material [12]. However, copper films deposited onto SiC can be of interest as technological underlayers, which are chemically stable with respect to carbon and its compounds at high temperatures and show good adhesion to virtually all other metals. Figures 1 and 2 show examples of the copper films deposited from

1063-7850/02/2805-0439$22.00 © 2002 MAIK "Nauka/Interperiodica"

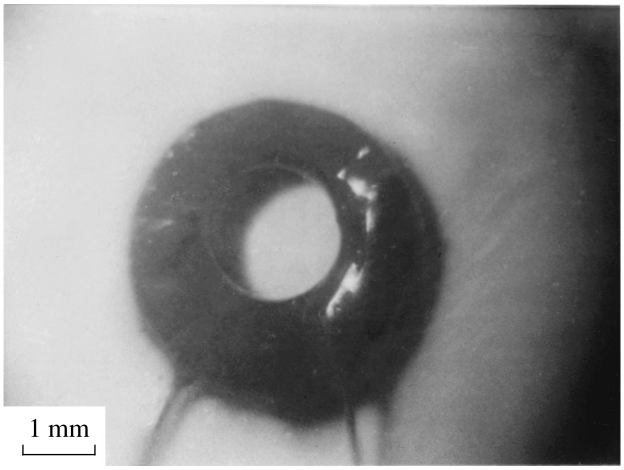

Fig. 1. A ring-shaped copper thermoresistor on 6H-SiC(N).

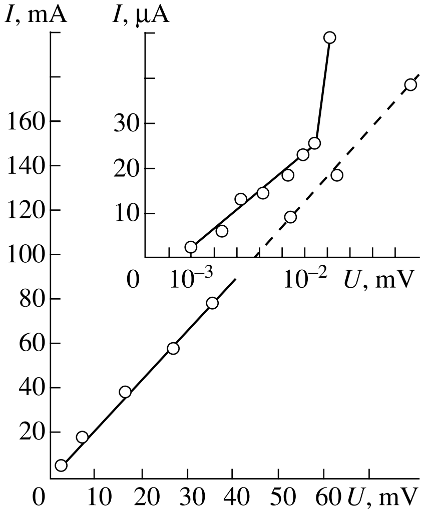

Fig. 2. The experimental current–voltage characteristics of an In–Cu–SiC structure.

porous electrodes, which model thermoresistors and contacts on SiC. The external protective coating was made of indium. The results of measurements showed that the In–Cu–SiC structures are temperature-sensitive and their *I*–*U* curves exhibit no anomalies. The contact potential difference, determined from the experimental *I*–*U* curves and the temperature dependence of resistance, was about 0.01 mV. The *I*–*U* curves are linear and symmetric.

Conclusion. The main experimental results are as follows:

(i) A galvanic process in the porous electrode–silicon carbide system provides for the local deposition of copper onto the substrate surface of any crystal orientation at room temperature.

(ii) The character of porous electrode translation over the substrate surface influences, together with traditional factors, the growing copper film structure.

(iii) The copper films deposited from porous electrodes can be used as contacts on SiC elements.

REFERENCES

1. Yu. A. Vodakov, A. O. Konstantinov, D. P. Litvin, and V. I. Sankin, Pis'ma Zh. Tekh. Fiz. **7** (12), 705 (1981) [Sov. Tech. Phys. Lett. **7**, 301 (1981)].
2. Akira Suzuki, Kazunobu Mameno, Nobuyuki Furui, and Hiroyuki Matsumami, Appl. Phys. Lett. **39** (1), 89 (1981).
3. J. Crofton, P. A. Barnes, and J. P. Williams, Appl. Phys. Lett. **62** (4), 384 (1993).
4. A. N. Andreev, A. I. Lebedev, M. G. Rastegaeva, *et al.*, Fiz. Tekh. Poluprovodn. (St. Petersburg) **29** (10), 1833 (1995) [Semiconductors **29**, 957 (1995)].
5. A. V. Afanas'ev, V. A. Il'in, and A. A. Petrov, in *Proceedings of the III International Workshop "Silicon Carbide and Related Materials," Novgorod, 2000*, p. 202.
6. L. P. Mileshko, I. N. Sorokin, and Yu. D. Chistyakov, *Activated Processes in Microelectronic Technology* (Nauka, Moscow, 1980), pp. 29–40.
7. N. S. Savkina, V. V. Ratnikov, V. B. Shuman, and A. A. Volkova, in *Proceedings of the III International Workshop "Silicon Carbide and Related Materials," Novgorod, 2000*, p. 159.
8. A. N. Yampol'skiĭ and L. A. Il'in, *Concise Handbook of Electroplater* (Mashinostroenie, Leningrad, 1981).
9. O. G. Bazhenov and V. A. Karachinov, Pis'ma Zh. Tekh. Fiz. **22** (21), 26 (1996) [Tech. Phys. Lett. **22**, 875 (1996)].
10. S. N. Kochergin and A. V. Leont'ev, *Formation of Textures under Electrochemical Crystallization of Metals* (Metallurgiya, Moscow, 1974).
11. I. D. Gruev, N. I. Matveev, and N. G. Sergeva, *Electrochemical Coatings on Electronic Devices* (Radio i Svyaz', Moscow, 1988).
12. I. K. Amirov and A. V. Zhokhov, Zh. Tekh. Fiz. **65** (10), 187 (1995) [Tech. Phys. **40**, 1078 (1995)].

Translated by P. Pozdeev

Technical Physics Letters, Vol. 28, No. 5, 2002, pp. 441–443. Translated from Pis'ma v Zhurnal Tekhnicheskoĭ Fiziki, Vol. 28, No. 10, 2002, pp. 88–94.
Original Russian Text Copyright © 2002 by Kleshchinov, Batyaev, Begel'dieva, Kharitonov.

Cooperative Activation of Neodymium Luminescence by Titanium(III) and Manganese(II) Ions in a Potassium Aluminosilicate Phosphate Glass

E. B. Kleshchinov, I. M. Batyaev, S. M. Begel'dieva, and D. V. Kharitonov
Herzen Pedagogical Institute, St. Petersburg, Russia

Received January 14, 2002

Abstract—A luminophor based on a potassium aluminosilicate phosphate glass activated with Ti(III), Mn(II), and Nd(III) ions was synthesized. It is shown that Nd luminescence in this glass is activated by titanium and manganese ions via a cooperative dipole–dipole mechanism. © *2002 MAIK "Nauka/Interperiodica".*

A nonradiative transfer of the electron excitation energy is successfully employed in the physics of laser materials for increasing the efficiency of pumping of the optical quantum generators. The purpose of this study was to assess the possibility of nonradiative transfer of the electron excitation energy in a glass matrix containing a system of three activators: Ti^{3+}, Mn^{2+}, and Nd^{3+}.

Previously [1–9], we have studied a series of biactivated systems containing a rare-earth (RE) emitter ion and a 3*d*-metal activator. Based on the results of these investigations, we obtained glassy RE-containing luminophors effectively excited with lamp pumping in the entire visible range. However, the activators did not provide for the possibility of using pumping radiation in the UV range. In this case, the energy emitted by the pumping lamp in the UV range was not converted into the laser emission and, hence, was ineffectively dissipated. It was suggested that this disadvantage could be partly removed by introducing manganese ions possessing an optical absorption band in the near UV range.

Based on these considerations, we have synthesized and characterized a potassium aluminosilicate phosphate (PASP) glass coactivated with Ti^{3+}, Mn^{2+}, and Nd^{3+} ions. The results of preliminary experiments led to a conclusion that the system features cooperative activation of the neodymium luminescence by titanium and manganese ions. The PASP composition was synthesized by coprecipitation from the solutions of the components, which ensured a high degree of homogeneity of the glassy matrix. The concentrations of the activator ions were as follows (wt %): Nd, 0.5; Mn, 3; Ti, 0.5.

The electronic absorption spectrum of the PASP glass (Fig. 1) exhibits a superposition of the absorption bands belonging to Ti^{3+}, Mn^{2+}, and Nd^{3+} ions. No visible differences from the spectra of noncoactivated ions were detected.

The luminescence spectra were measured on an SDL-1 spectrometer equipped with FEU-79 and FEU-39A photomultiplier detectors. The spectra were excited by radiation from a DRSh lamp filtered by various standard optical filters, an LGN-222 He–Ne laser (λ = 630 nm), and a nitrogen laser (λ = 337 nm). The luminescence spectrum of the PASP:Ti^{3+}–Mn^{2+}–Nd^{3+} glass (Fig. 2) exhibits narrow intense bands ion the region of λ_{max} = 890 and 1055 nm, which can be attributed to the radiative transitions in an Nd^{3+} ion ($^4F_{3/2} \longrightarrow {}^4I_{9/2}$ and

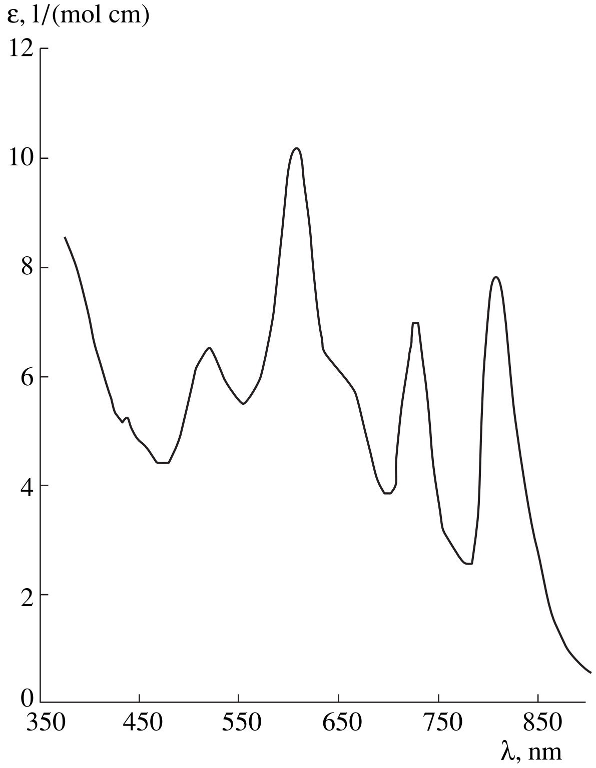

Fig. 1. The optical absorption spectrum of PASP:Ti^{3+}–Mn^{2+}–Nd^{3+} glass.

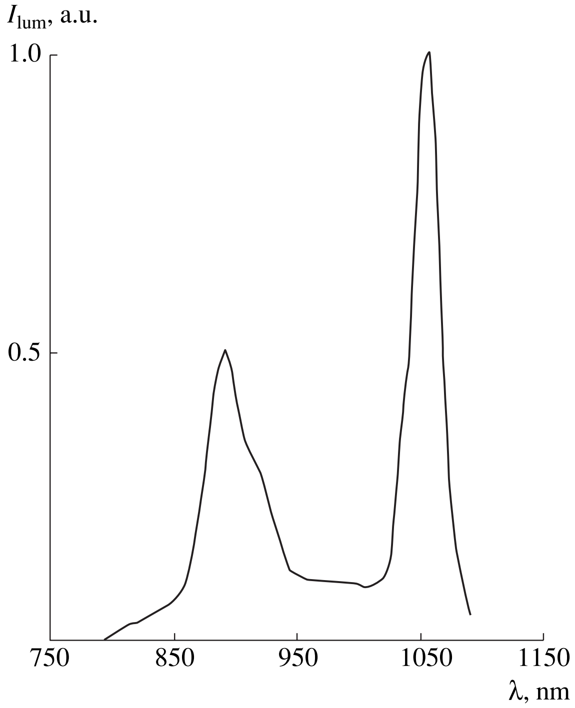

Fig. 2. The luminescence spectrum of a PASP:Ti^{3+}–Mn^{2+}–Nd^{3+} glass.

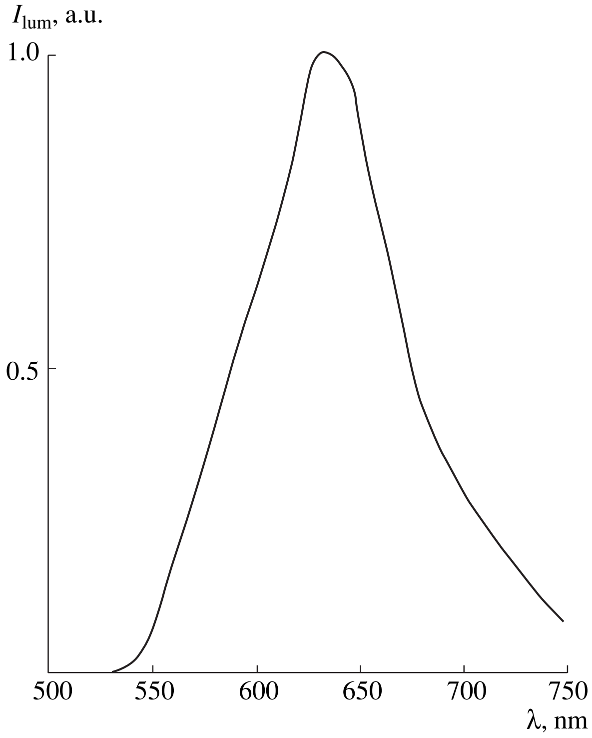

Fig. 3. The luminescence spectrum of a PASP:Mn^{2+} glass.

$^4F_{3/2} \longrightarrow {}^4I_{11/2}$) and a very weak and broad band at 800–1000 nm assigned to the luminescence channel of Ti^{3+} (^2E_g–$^2T_{2g}$); the intensity of the latter band is less than one-tenth of the intensity of noncoactivated bands due to Ti^{3+} ions in the same glass matrix.

We failed to detect the luminescence band of Mn^{2+} ($^6A_1 \longrightarrow {}^4A_1$ transition) expected in the region of 630 nm (Fig. 3). Thus, the results are indicative of the quenching of luminescence of the titanium and manganese ions in the PASP:Ti^{3+}–Mn^{2+}–Nd^{3+} glass. This suggests a nonradiative transfer of the excitation energy from titanium and manganese ions to a metastable $^4F_{3/2}$ level of the neodymium ion (cooperative activation). This hypothesis can be verified by a comparative analysis of the spectra of luminescence excitation of neodymium via the $^4F_{3/2} \longrightarrow {}^4I_{9/2}$ channel in the PASP:Ti^{3+}–Mn^{2+}–Nd^{3+} glass and in the PASP glass activated only by Nd^{3+} ions.

Figure 4 shows the luminescence excitation spectra of PASP glasses. As can be seen, the introduction of Ti(III) and Mn(II) ions into the PASP:Nd^{3+} system leads to a significant change in the spectrum, as manifested by additional broad bands corresponding to the absorption bands of Ti^{3+} and Mn^{2+} ions. This result confirms the presence of cooperative activation of neodymium ions in the glass studied.

The efficiency of the nonradiative energy transfer and the contributions due to both activators can be determined from a comparative analysis of the kinetic curves of decay of the excited states of Ti(III) and Mn(II) in the glasses with and without neodymium. The results of such investigations showed that the average

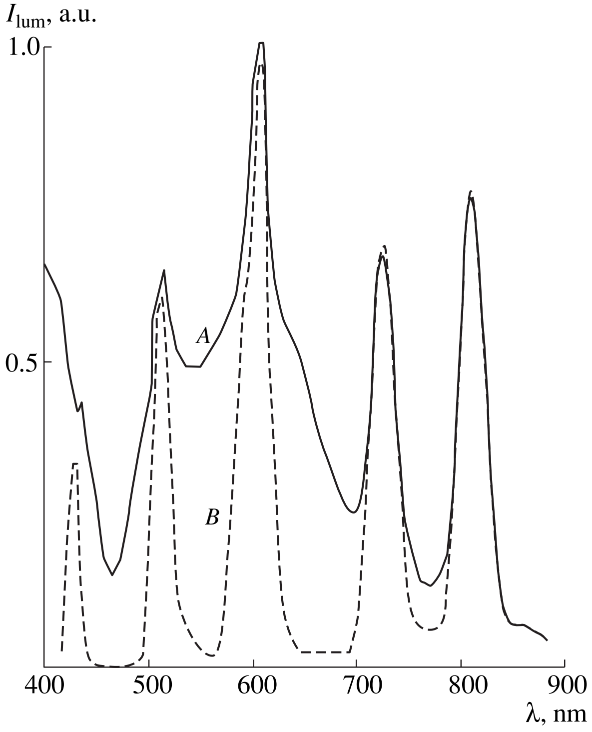

Fig. 4. The Nd^{3+} luminescence excitation spectra of (*A*) PASP:Ti^{3+}–Mn^{2+}–Nd^{3+} and (*B*) PASP:Nd^{3+} glasses.

time of titanium luminescence in the Ti^{3+}–Nd^{3+} pair decreases from 6 to 1.5 μs, while the average time of manganese luminescence in the Mn^{2+}–Nd^{3+} pair decreases from 6 to 2 ms.

The results of modeling the kinetic curves by the known functions describing the quenching of luminescence from donors in the presence of acceptors [9] allowed us to determine the mechanism of energy transfer in the Ti^{3+}–Nd^{3+} and Mn^{2+}–Nd^{3+} as belonging to the dipole–dipole type. Calculations of the quantum efficiency of this transfer by the formula

$$n = \frac{\tau_{od} - \tau_d}{\tau_{od}},$$

where τ_d and τ_{od} are the times of donor luminescence with and without an acceptor, gave values of about 0.75 and 0.66. Therefore, titanium ions present in the PASP:Ti^{3+}–Mn^{2+}–Nd^{3+} glass yield a somewhat greater contribution to the coactivation process.

Thus, we have demonstrated for the first time the possibility of cooperative activation of neodymium luminescence by titanium(III) and manganese(II) ions in glass matrices.

REFERENCES

1. I. M. Batyaev and E. B. Kleshchinov, Opt. Spektrosk. **81** (5), 823 (1996) [Opt. Spectrosc. **81**, 753 (1996)].
2. I. M. Batyaev and E. B. Kleshchinov, Pis'ma Zh. Tekh. Fiz. **22** (12), 34 (1996) [Tech. Phys. Lett. **22**, 494 (1996)].
3. I. M. Batyaev and S. B. Sukhanov, Opt. Spektrosk. **72** (6), 1367 (1992) [Opt. Spectrosc. **72**, 765 (1992)].
4. I. M. Batyaev and I. V. Golodova, Opt. Spektrosk. **77** (1), 81 (1994) [Opt. Spectrosc. **77**, 45 (1994)].
5. I. M. Batyaev and E. B. Kleshchinov, Pis'ma Zh. Tekh. Fiz. **23** (21), 7 (1997) [Tech. Phys. Lett. **23**, 820 (1997)].
6. I. M. Batyaev and E. B. Kleshchinov, Zh. Obshch. Khim. **67** (7), 1207 (1997).
7. E. B. Kleshchinov, Author's Abstracts of Candidate's Dissertation (St. Petersburg, 1997).
8. I. M. Batyaev and S. B. Sukhanov, Pis'ma Zh. Tekh. Fiz. **20** (10), 38 (1994) [Tech. Phys. Lett. **20**, 403 (1994)].
9. I. M. Batyaev and I. V. Golodova, Opt. Spektrosk. **78** (3), 468 (1995) [Opt. Spectrosc. **78**, 421 (1995)].
10. V. A. Ermolaev, E. N. Bodunov, E. B. Sveshnikov, and T. A. Shakhverdov, *Nonradiative Transfer of Electron Excitation Energy* (Leningrad, 1977).

Translated by P. Pozdeev

Technical Physics Letters, Vol. 28, No. 5, 2002, p. 444.

ERRATA

Erratum: "Microwave Oscillations as an Indicator of the Magnetoplasmadynamic Thruster Operation in a Limiting Regime" [*Tech. Phys. Lett.* 26 (7), 612 (2000)]

The list of the authors should read V. I. Brukhty and K. P. Kirdyashev.